

Electrophoretic Nanoinjection: New Applications for Live Cell Experiments

Matthias Simonis

Dissertation
an der Fakultät für Physik
der Universität Bielefeld

vorgelegt von
Matthias Simonis

Juni 2017

Erstgutachter: Prof. Dr. Thomas Huser
Zweitgutachter: Prof. Dr. Andreas Hütten

Abstract

Nanoinjection is a relatively new method used to deliver foreign molecules into single living cells by employing small hollow glass capillaries. In contrast to microinjection, the pipette tip has an inner diameter of only 100 nm and the injection itself is not pressure-driven. Instead, an electric field is used to drive molecules out of the pipette and into the cell via electrophoresis with high precision.

In this work, I show that using the smaller nanopipette leads to an increased survival rate of 92% compared to only 40% for a five times larger micropipette. These values were determined a full 24 hours after the injection and therefore are more conclusive than previous publications concerning the viability

To make nanoinjection more accessible and easier to utilise, I developed a new mobile system (MoNa – mobile nanoinjection) that can be built at only 13% the costs of the previously used equipment. However, I prove MoNa to have the same injection capabilities with the added benefits of flexibility, portability and ease of use.

As a new application for nanoinjection I demonstrate the combination with single molecule localisation microscopy and generate three-dimensional super-resolved images of the actin structure of a living cell. Furthermore, the adjustment of labelling density simultaneously to the imaging process was shown to work. In the course of these experiments, I also demonstrated the importance of choosing the right immersion oil for the fluorescence microscope. An unsuitable oil was shown to yield an up to 20% worse resolution laterally and even over 200% axially.

Finally, I show the nanoinjection of non-adherent algae cells with fluorescent molecules. This could prove to be a viable tool for gene editing of these unicellular organisms through injection of the CRISPR/Cas9 protein complex.

Zusammenfassung

Nanoinjection ist eine relativ neue Methode um Moleküle in einzelne lebende Zellen einzubringen. Im Vergleich zur Mikroinjektion hat die (Nano-)Pipette hier nur einen inneren Durchmesser von etwa 100 nm und funktioniert nicht über einen rückwertig angelegten Druck. Stattdessen werden die Moleküle über ein angelegtes elektrisches Feld und Elektrophorese mit hoher Präzision aus der Spitze in die Zelle befördert.

In dieser Arbeit zeige ich, dass der Gebrauch von Nanopipetten bei der Injektion von lebenden Zellen zu einer hohen Überlebensrate von 92% führt. Im Vergleich dazu wurden unter denselben Bedingungen nur 40% mit den etwa fünffach größeren Mikropipetten erreicht. Diese Werte wurden volle 24 Stunden nach der Injektion bestimmt und sind somit aussagekräftiger als vorherige Studien

Um Nanoinjection zugänglicher und einfacher zu gestalten, haben wir ein neues mobiles System (MoNa – Mobile Nanoinjection) entwickelt, das zu einem Bruchteil der Kosten (13%) des vorherigen Systems aufgebaut werden kann. Trotzdem zeigen wir, dass MoNa dieselben Möglichkeiten für Injektionen bietet und darüber hinaus noch flexibel, portabel und einfach in der Anwendung ist.

Als eine neue Anwendung der Nanoinjection demonstriere ich die Kombination mit Einzelmolekül Lokalisationsmikroskopie und erstelle dreidimensionale, superaufgelöste Bilder von der Aktin-Struktur lebender Zellen. Dabei wird auch bewiesen, dass es möglich ist, während der Bildaufnahme die Farbstoffdichte über den Ionenstrom zu justieren. Ebenfalls konnten ich bei diesen Experimenten zeigen, dass die richtige Wahl des Immersionsöles von großer Bedeutung ist. Ein „falsches“ Öl führt zu einer 20% schlechteren laterale Auflösung und in axialer Richtung beträgt die Verschlechterung sogar über 200%.

Abschließend zeige ich, dass es möglich ist, auch in nicht adhärente Zellen wie einzellige Algen einen Fluoreszenzfarbstoff zu injizieren. Dies könnte alternativ zu Elektroporation als neue Möglichkeit genutzt werden, um CRISPR/Cas9 Proteinkomplexe in diese Zellen einzubringen um Genveränderungen vorzunehmen.

Contents

Abstract	i
Zusammenfassung	ii
Contents.....	iii
1 Introduction.....	1
2 Theoretical Background	7
2.1 Fluorescence Microscopy	7
2.1.1 Fluorescence	8
2.1.2 Spatial Resolution	10
2.1.3 Widefield Fluorescence Microscope Setup.....	12
2.1.4 Fluorophores	14
2.1.5 Single Molecule Localisation Microscopy.....	16
2.1.6 3D STORM.....	21
2.2 Nanoinjection.....	23
2.2.1 Injection Procedure	24
2.2.2 Molecule Kinetics inside a Nanopipette	25
3 Survival Rate of Eukaryotic Cells Following Nanoinjection.....	29
3.1 Introduction.....	29
3.2 Method & Preliminary Experiments	30
3.2.1 Dextran as a Negative Dead Cell Stain.....	31
3.2.2 Influence of the Electric Field	33
3.3 Survival Statistics.....	34
3.4 Discussion & Conclusion.....	36
4 Development of a Mobile Nanoinjection (MoNa) System	41
4.1 Motivation	41
4.2 Setup	42
4.2.1 Electrode Amplifier	43
4.2.2 Positioning	43
4.2.3 Hardware.....	44
4.2.4 Controller & Software	44
4.3 Comparison to the Original SICM System.....	48

4.4	Injections of Fluorescent Dyes	50
4.5	Conclusion	52
5	Immersion Oils in Localization Microscopy	55
5.1	PSF Comparison.....	56
5.2	2D dSTORM PSF Statistics.....	59
5.3	Correction for Refractive Index Mismatch.....	60
5.4	3D dSTORM imaging.....	63
5.5	Conclusion	63
6	Nanoinjection PAINT.....	65
6.1	Real-time Control of Labelling Density	65
6.2	PAINT Imaging of the Cytoskeleton	70
6.3	3D PAINT imaging.....	71
6.4	Discussion & Conclusion.....	72
7	Nanoinjection of the Alga Chlamydomonas Reinhardtii.....	75
7.1	History & Motivation	76
7.2	Injection Procedure and Cell Preparation	76
7.3	Fluorophore Injection	78
7.4	Injection of RNPs	79
7.5	Conclusion	80
8	Heating & Cooling Microscope Stage.....	81
8.1	Peltier Controlled Microscope Stage.....	82
8.2	Cooling Experiments	84
8.3	Conclusion	86
9	Conclusions and Outlook	87
A	Appendix	91
A.1	Raw Data of the Survival Statistics.....	91
A.2	Nanoinjection Materials & Methods.....	92
A.3	MoNa Software Documentation.....	93
A.4	MoNa Operational Amplifier Circuit.....	95
A.5	Fluorescence Microscope Setup.....	96
A.6	Fluorophores & Filter Sets	96
A.7	Cell Preparation & Staining	97
A.8	Additional Materials & Methods	99

List of Figures.....	101
List of Tables.....	103
List of Abbreviations.....	104
References.....	107
Publications & Conferences.....	117
Acknowledgements.....	118
Erklärung.....	121

1 Introduction

Cell Delivery Methods

How to introduce foreign molecules into living cells? This is a fundamental question and problem for researchers trying to study biological processes on a (sub-) cellular level. Over time, several approaches have been developed in order to cope with this issue. Broadly speaking one can separate these methods into two categories. Single cell techniques that work with specific, selected cells and ensemble methods that take a wider approach and treat many cells (in some cases millions) at once in a stochastic manner. The latter includes procedures such as electroporation (Neumann et al. 1982), lipofection (Felgner et al. 1987) or glass bead delivery (McNeil und Warder 1987). But one must take into account that in most cases, these methods are used on whole cell cultures and usually the welfare of individual cells isn't of any interest. That is why even though these methods have been around for decades and are well established, mortality rates of up to 50 % are accepted (Canatella et al. 2001; Hapala 1997).

On the other hand for single-cell specific procedures the survival of individual cells is one of the most important factors for an efficient work-flow. Maybe the most popular and widely applied method is microinjection. Its basic working principle is that of a syringe. Thin glass capillaries are heated and pulled to a fine aperture usually ranging from 0.5 μm to a couple of micrometres depending on their application. With these devices called micropipettes, a wide range of samples from single cells to small organisms can be treated (Graessmann und Graessmann 1983; Pepperkok et al. 1988; DePamphilis et al. 1988).

This method started as a “hands-on” approach, as positioning of the pipettes and the actual injection was done exclusively by hand. Reproducibility and feasibility

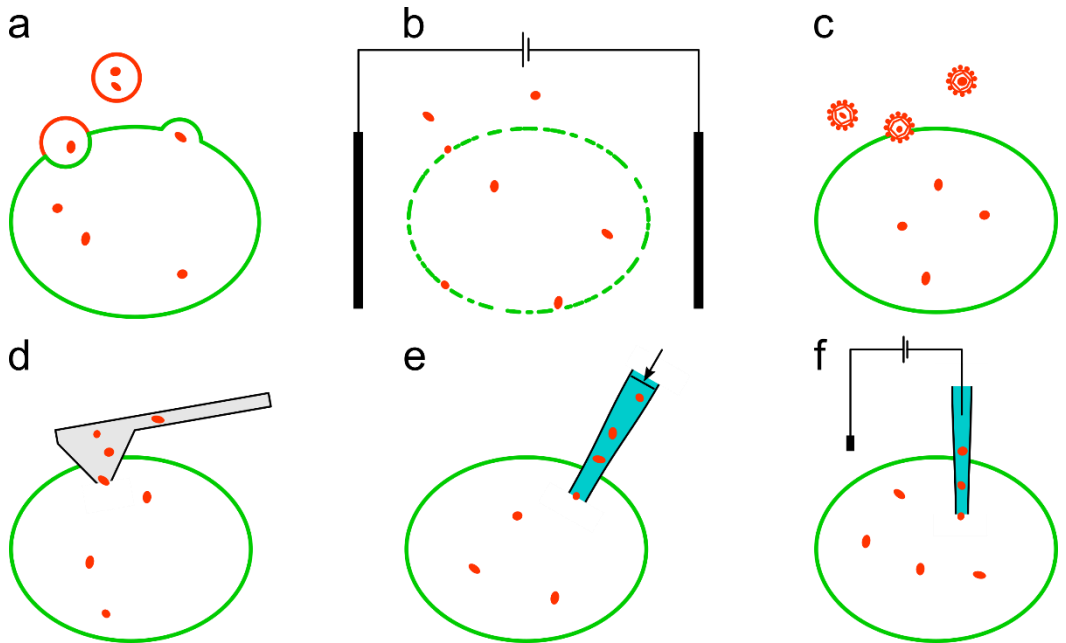


Figure 1: Schematic illustration of cell delivery methods. The cell membrane is depicted in green, delivered molecules are red. Not to scale. (a) Lipofection. Small vesicles (liposomes) fuse with the cell membrane and release their content into the cell. (b) Electroporation. The membrane is permeabilized through an electric field. The molecules can diffuse into the cell. (c) Viral transduction. A virus or viral vector is used to introduce a foreign molecule (constricted to DNA) into the cell. (d) AFM. A hollow cantilever pierces the membrane and injects the molecules. (e) Microinjection. The molecules are injected through a hollow glass capillary into the cell by pressure. (f) Electroporetic nanoinjection. A voltage applied to two electrodes allow the injection via electrophoretic forces.

was pretty much restricted to larger cells and organisms. Recent advancements in technology however, made a semi-automated approach possible (Viigipuu und Kallio 2004; Wang et al. 2008). As a result, the reliability and success-rate of injection could be vastly improved. Another benefit of this refinement was the possibility to use smaller, more fragile pipette sizes which led in some cases to an improved survival rate of the treated cells. In the range of 10s to a few 100 nm, syringe-like injections become difficult and the tips may simply brake due to the pressure build-up at the narrow opening diameter. More stable carbon-coated glass pipettes (Schrlau et al. 2008) or carbon tubes inserted and glued to a larger pipette tip have been used to resolve this issue (Xing et al. 2014).

A different kind of probe architecture is presented with AFM cantilevers. While early adaptations again used a carbon nanotube attached to the probe to inject surface bound materials into cells (Yum et al. 2010), more recent methods use hollow

cantilevers for injection (Guillaume-Gentil et al. 2014). These methods are a viable alternative to using glass nanopipettes and additionally provide the opportunity to measure the force required to penetrate the cell membrane. Nevertheless, more elaborate setups, costlier and time intensive probe fabrication are certainly downsides to keep in mind.

Other, more exotic approaches such as optical injection through optical heating of membrane-attached gold nanoparticles can be used under certain circumstances but lack the flexibility and reproducibility of “classical” injection methods. Furthermore, the used excitation light will lead to an increased mortality (Li et al. 2015).

Electrophoretic Nanoinjection

The majority of injection techniques described above are pressure-driven. While this is the certainly the most intuitive and easy to achieve procedure for delivering molecules, it comes with a few drawbacks. Namely the injection volume and probe size. Injections in femtolitre regimes are possible but still it is hard to control the exact volumes that are transferred into the cell. Furthermore, this delivers the entire solution into the cell. For small concentrations of a certain molecule that means potentially introducing a large volume of foreign material into the cell. Additionally, the probe size has its limits as mentioned earlier.

A solution to this appeared with the introduction of voltage-controlled nanoinjection (Adam Seger et al. 2012). Here, the molecules of interest are not pushed through the pipette by applying a pressure but rather through electrophoretic forces. This way, the inner diameter of the glass pipette can be reduced to 100 nm and below. The injection itself can now be controlled with much higher precision by adjusting the voltage between an electrode inside the pipette and in the surrounding medium. Subsequently, nanoinjection was used for a variety of applications such as transgene delivery (Wilson et al. 2013), electrochemical measurements within cells (Actis et al. 2014b) or fluorescently labelling the cell for super-resolution imaging (Hennig et al. 2015b).

In addition to the increased precision of electrophoretic injections, one can make use of the emerging ionic current. Like in scanning ion conductance microscopy (SICM) it is possible to detect changes in the direct vicinity of the pipette tip (e.g. cell membranes) through variations in this current. This information can be used to determine with high accuracy the exact position of the pipette in relation to the cell. It is even possible to detect cell organelles like the nucleus with this feedback

(Anderson und Bau 2014). Though the exact molecule kinetics inside the nanopipette (caused by multiple effects such as electrophoresis, electro-osmosis and dielectrophoresis) are yet to be described conclusively, the empiric data presents nanoinjection as a viable alternative to classical microinjection with both advantages and disadvantages. In this work, I want to further determine and expand the capabilities of electrophoretic nanoinjection as a tool for single cell manipulation.

Survival Rate after Electrophoretic Injections

As of now there has not been a conclusive work reporting on the survival rate of injected cells. Thus, my first goal was to determine a reliable statistical analysis of the viability of individual cells. To further increase the validity of this analysis, the cell's health state will be defined after one full day subsequent to injection. This way the organism has time to adjust to the damage inflicted by the inserted pipette. Additionally, the proliferation behaviour can be checked during that time span, giving further insight of the cell's health status.

Furthermore, I will conduct these experiments two times. Once using custom made nanopipettes with an inner diameter of 100 nm and the second time with commercially available 0.5 μm diameter micropipettes. This will give an idea of how (or if at all) the probe size correlates with the survival rate.

Developing a Mobile Nanoinjection System

To make electrophoretic nanoinjection more accessible and flexible, I will try to evaluate our existing nanoinjection setup and reduce it to its essential components. As most injection systems, it too is an experimental setup previously used for SICM. Consequently, its capabilities surpass those needed for the less complex nanoinjection process. That is why a huge potential for down-sizing and simplification presents itself. The new mobile nanoinjection (MoNa) system I want to construct will be tested to have the same capabilities in regard to nanoinjection as our old system. The reduced complexity should in turn also lead to a vastly reduced price point and much easier and more flexible usability.

New applications for Nanoinjection

Since fluorescence microscopy is the bread-and-butter of biological imaging techniques, I want to explore possible opportunities for new applications especially regarding super-resolution methods. Here, I will focus on single molecule localisation microscopy. A common problem in fluorescence microscopy is to achieve a suitable

labelling of the structures of interest. Intrinsic fluorescence can seldom be used. Apart from transfecting the cells to express fluorescent proteins, the only option is to introduce dye molecules into the cell. This is where nanoinjection could prove viable. By simultaneous injection and imaging, I want to optimise labelling conditions on the fly to generate optimized super-resolved images. This way, the imaging process could be adapted to a variety of different conditions concerning buffer, fluorophores and acquisition timings.

In a short excursus beforehand, I will optimise our fluorescence microscope regarding the used immersion oil. I hope that by doing this, subsequently acquired images will yield a higher quality and resolution especially concerning three-dimensional images.

An additional application is the injection of RNPs (ribonucleoprotein complexes) into living *C. Reinhardtii* algae cells to knockout or modify specific genes. It turns out that in this case, standard delivery methods such as electroporation yield an unusually low efficiency. Nanoinjection could provide a well working alternative. I will first establish a protocol to reliably nanoinject the algae using a highly visibly fluorophore. In a second step, injection of the RNPs itself has to be established.

2 Theoretical Background

This chapter serves as an introduction to the theoretical background of the methods used in the work at hand. It mainly concentrates itself around the vastly popular technique fluorescence microscopy, its backgrounds and advancements and of course the more recent scanning ion conductance microscopy-derived method nanoinjection.

2.1 Fluorescence Microscopy

Since its first commercial appearance in 1911 (Gerlach 2009; Heimstädt 1911), fluorescence microscopy has become a cornerstone of modern biology and other accompanying scientific disciplines. Its unique properties led to high-contrast images previously not possible, that pretty much revolutionized the way we look at cells today. Now it was possible to visualize subcellular processes and study living cells in great detail (Figure 2). Recent developments like STORM (Rust et al. 2006), PALM (Betzig et al. 2006), STED (Hell und Wichmann 1994) or SIM (Gustafsson 2000) even went beyond the theoretical resolution limit of classical optical microscopy and opened up a vast new field of opportunities for exploring biology on the scale of a few nanometres.

An essential role in the success of all of these methods is played by the fluorescent molecules and proteins used to mark specific structures of the examined samples. They have to adhere to certain restrains concerning emission and absorption spectra, fluorescent lifetime, photostability and quantum efficiency to allow the

microscopy methods to work to their fullest potential. But also other factors such as cytotoxicity or cell permeability play a major role in the efficiency of biological fluorescent microscopy.

2.1.1 Fluorescence

As the name already suggests, the underlying physical principle behind fluorescence microscopy is fluorescence. It describes the absorption and emission of light by atoms and molecules. The processes and concepts of this chapter are derived mainly from J. R. Lakowicz (Lakowicz 2006).

Fluorescence is a special case of luminescence that is only present within 10^{-6} to 10^{-9} s of excitation through an incident photon (in contrast to phosphorescence that takes place on time scales of 10^{-2} to 10^2 s). Usually, the emitted photon holds an energy smaller than that of the exciting photon. This specific property is equivalent to a red shift of the wavelength and known as the Stokes shift (Figure 3 a). It is the fundamental working principle of fluorescence microscopy.

To explain the missing energy of this process, we have to look at the internal energy states of the molecule. A simplified illustration of this is presented with the Jablonsky diagram (Figure 3 b). According to Kasha's rule, the vast majority of fluorescence photons are emitted from the ground vibrational state of the excited electric state S_1 . Absorption on the other hand rarely occurs into the lowest vibrational state. Therefore, energy is lost by vibronic relaxation and other radiationless transitions, hence the Stokes shift.

If these transitions are all happening between the singlet states $S_0...S_n$, i.e. with the same multiplicity, the entire process takes only a few nanoseconds. In the case of intersystem crossings to and from the triplet states $T_0...T_n$, an electron spin flip has

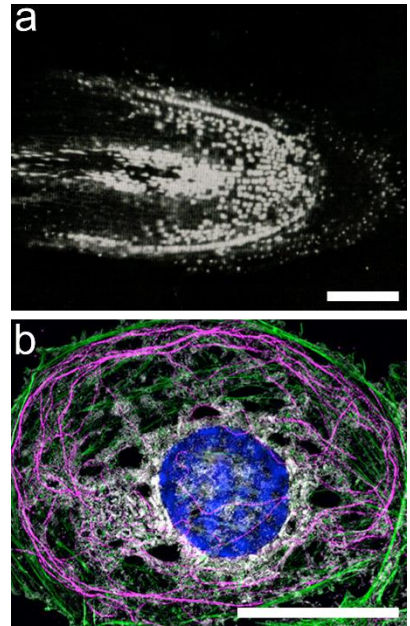


Figure 2: Fluorescence images

(a) One of the first fluorescence microscopy images of an actively stained sample (Haitinger 1938) Onion root tip, nuclei are visible as white dots. Scale bar, ca. 1 mm (b) Modern super-resolved, multi-color image of a single liver cell (Monkemoller et al. 2015). The nucleus is depicted in blue. Scale bar, 10 μ m

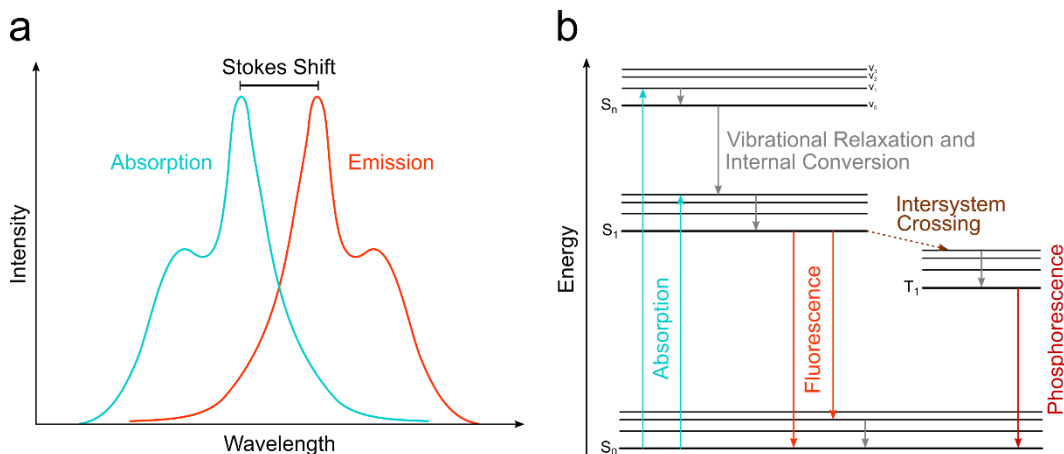


Figure 3: Fluorescence and phosphorescence principles. Adapted from Lakowicz (2006) (a) Absorption and emission spectra of a typical fluorescent molecule. The wavelength difference of their peaks denotes the Stokes shift. (b) Jablonski diagram, schematic illustration of possible transitions between different energy states. Fluorescence happens by absorption of a photon into an excited electric state S_n . After vibrational relaxation and/or internal conversion, the fluorescent transition is most likely to occur from the vibrational ground state v_0 . Through intersystem crossing (with a spin flip) the system can fall into the excited triplet state T_1 . Because this transition is less probable, the phosphorescence cycle has a much longer lifetime.

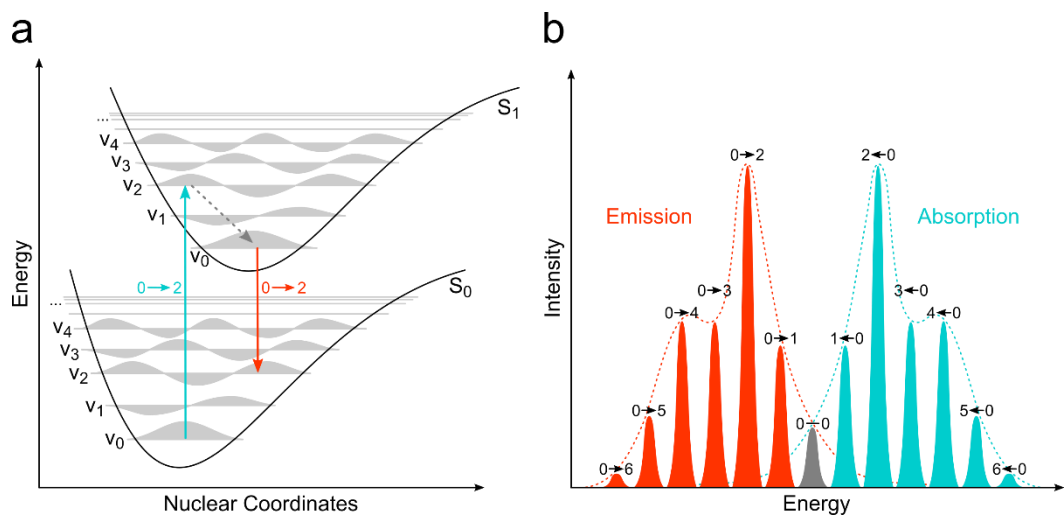


Figure 4: Transition probabilities and spectra. Adapted from Lakowicz (2006) (a) Illustration of the Frank-Condon principle. The electric transitions happen so fast (10^{-15} s) that during this time the nuclear coordinates will not change due to the relatively high mass of the nucleus (Born-Oppenheimer approximation). Thus, the transition probability mainly increases depending on the amount the involved vibrational state wave functions overlap. The same is true for the emission from the S_1 vibronic ground state back to the electric ground state. A likely transition pathway cycle is depicted above. (b) Because the two potentials have an almost identical shape, nearly the same transition probabilities will emerge for emission and absorption, leading to mirror-imaged spectra.

to occur. While this is possible to happen via spin-orbit coupling, these transitions are far less likely. Thus, the time to depopulate the excited T_1 state back to S_0 through emission of a photon takes much longer and is called phosphorescence.

Another interesting property of fluorescence becomes clear by taking a closer look at the emission and absorption spectra of fluorescent molecules (Figure 4 b). They are basically mirror images of each other. This can be explained through the Frank-Condon principle that describes the transition probabilities between the different states of the system (Figure 4 a). It is based on the assumption that transitions are more likely to occur, when the vibrational wave functions of two states overlap to a greater extent.

2.1.2 Spatial Resolution

The theoretical diffraction-based resolution limit of a microscope, i.e. the minimum distance d between two objects under which they can still be distinguished from each other, is dependent on only a few parameters. Their relationship was first investigated by Ernst Abbe in 1873 (Abbe 1873). He used a diffraction grating and determined the angle of the first order diffracted beam. This beam has to be detected in order to gain knowledge of the lattice constant. Through this relationship he derived the following equation now known as Abbe diffraction limit:

$$d = \frac{\lambda}{2n \sin \vartheta} = \frac{\lambda}{2 \text{NA}} \quad (2.1)$$

ϑ is the angle of the first order beam equivalent to the aperture angle of the Objective. n stands for the diffraction index of the surrounding medium and λ for the wavelength of the used light. The numerical aperture of the objective (NA) is defined as

$$\text{NA} = n \sin \vartheta. \quad (2.2)$$

Another approach more applicable to fluorescence microscopy is presented with the Rayleigh criterion (Rayleigh 1879; Kubitscheck 2013). It is based on the geometry of

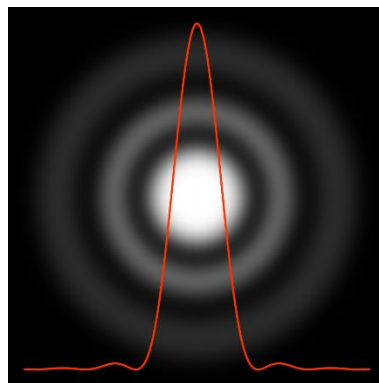


Figure 5: Airy pattern shape. Simulated Airy pattern and superimposed Bessel function based line plot through the center.

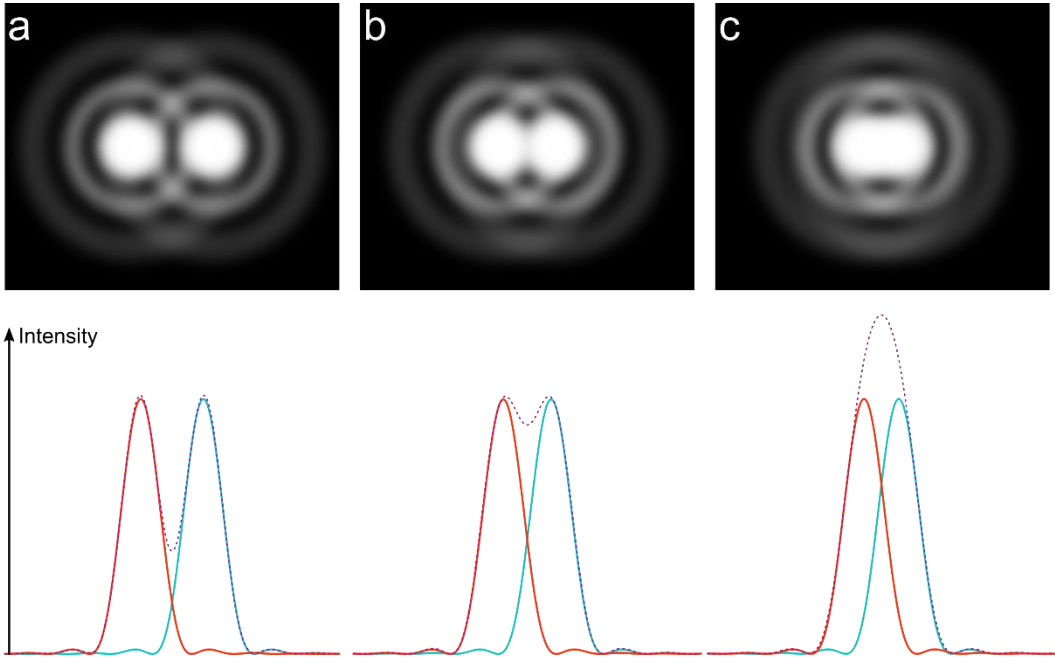


Figure 6: Illustration of the Rayleigh criterion. Top row depicts two simulated Airy patterns with different distances to each other. Bottom row shows the respective intensity line plots (solid lines) and their sum (dashed lines). (a) The emitters are still relatively far from each other and are easily distinguishable. (b) Rayleigh criterion. The maximum intensity of one pattern falls into the first minima of the second. This represents the distance under which two emitters can just barely be resolved. (c) If the patterns move even closer, they overlap too much for a reliable distinction.

the Airy patterns (Figure 6) produced by an optical system when a point source is imaged. Those patterns (also called point spread function – PSF) are mathematically described through a first-order, first-kind Bessel function J_1 :

$$I(x) \propto \left[\frac{J_1(x)}{x} \right]^2 \quad (2.3)$$

$I(x)$ denotes the intensity of the pattern at the distance x from the centre. The Rayleigh criterion states, that two point sources are still distinguishable, if the maximum of one PSF is not nearer to the second PSF than its first minimum (Figure 6). This can be calculated by finding the first zero of the Bessel function and yields the Rayleigh criterion

$$d = \frac{0.61 \lambda}{\text{NA}} . \quad (2.4)$$

2.1.3 Widefield Fluorescence Microscope Setup

The fundamental property of fluorescence that makes microscopes of this type even possible is the Stokes shift. Through a lowpass or dichroic filter, the high-powered light used for illumination of the sample is separated from the much weaker fluorescent signal. Oftentimes cleaned up by another bandpass or lowpass filter, the signal is collected by an adequate detector (Figure 7 a). In most cases an emCCD (electro multiplying charge-coupled device) or sCMOS (scientific complementary metal-oxide-semiconductor) camera, as they provide high performance in low light conditions and can even detect very weak signals. In order to filter out the excitation light effectively, a monochromatic light source is favourable. Often a laser is used but filtered mercury-vapor lamps or LEDs can also be equally feasible. However, the main setup used in this work utilises laser illumination which provides some distinct advantages.

When imaging a uniformly EPI-illuminated (epifluorescence) sample, not only the fluorophores directly in focus contribute to the collected signal but also those on lower and higher layers along the optical axis. This leads to a blurred image and relatively low signal-to-noise ratio. To circumvent this problem, the laser can be parallelly shifted along the axis of the excitation path to achieve HILO (Tokunaga et al. 2008) (highly inclined and laminated optical) or TIR (Ambrose 1956; Thompson et al. 1981) (total internal reflection) illumination (Figure 7 b).

For TIR illumination, the actual excitation beam is completely reflected at the cover glass/sample interface. Only high-NA objectives are able to provide the option of reaching the critical angle ϑ_c determined by Snell's law

$$\vartheta_c = \arcsin\left(\frac{n_1}{n_2}\right). \quad (2.5)$$

The refractive indices of the sample (approximated by water) $n_1 = 1.33$ and of a typical borosilicate glass coverslip $n_2 = 1.517$ yield a critical angle of around $\vartheta_c = 61^\circ$. If we calculate the minimum numerical aperture required, we get

$$\text{NA} = n_2 \sin\vartheta_c = 1.33. \quad (2.6)$$

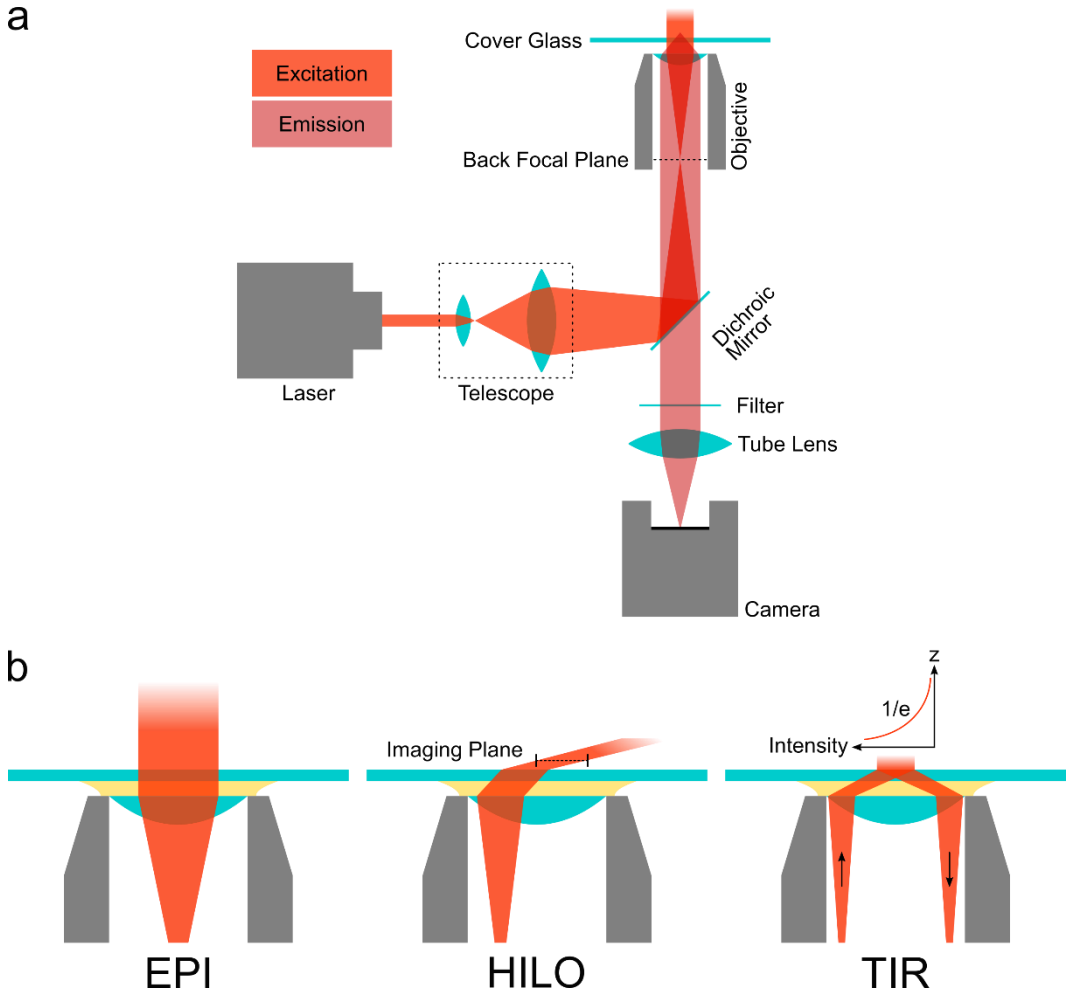


Figure 7: Fluorescence microscope setup and illumination modes (a) Schematic image of a widefield fluorescence microscope. The laser excitation beam is widened and focused through a telescope system consisting of two lenses. Reflected by the dichroic mirror it passes through the objective. It is important that the beam is focused onto the objective's back focal plane to achieve an even illumination through the sample. The fluorescence signal is collected by the same objective and can now pass the dichroic mirror due to its Stokes shift. Additional band-pass and long-pass filters are used to further reject the excitation wavelength and other unwanted signals. Finally, the fluorescence is focused onto the camera to form an image (b) Illustrations of different illumination modes. In case of EPI-fluorescence, the whole z -range of the sample is evenly excited causing out-of-focus regions to blur the image. During HILO illumination, the depicted imaging range is much more defined along the optical axis leading to a better signal-to-noise ratio. In TIR mode, only around 200 nm of the sample directly above the cover glass are illuminated by an evanescent field. It is caused by the incident beam that totally reflected at the glass-sample interface. This leads to an even better signal-to-noise ratio. However, the imaging region is basically restricted to the glass surface.

Using TIR, the sample is only illuminated by an evanescent field that decreases exponentially starting with an initial intensity I_0 from the cover glass surface $z=0$ into the sample (Axelrod 1981):

$$I(z) = I_0 \exp\left(-\frac{z}{d}\right) \quad (2.7)$$

d is dependent on the wavelength λ , the incident and critical angles, ϑ and ϑ_c of the light and the refractive index of the sample medium n_1 :

$$d = \frac{\lambda}{4\pi n_1 \sqrt{\frac{\sin^2 \vartheta}{\sin^2 \vartheta_c} - 1}} \quad (2.8)$$

This kind of field will illuminate the sample up to a depth of approx. 200 nm leading to an excellent signal-to-noise ratio since the excitation of out-of-focus fluorophores is effectively avoided.

However, this restricts imaging to the cover glass surface only. If the region of interest lies above this region, HILO can be used as an alternative. The z-dimension of the illumination sheet will be in the order of some μm , which still yields an improved signal-to-noise ratio compared to EPI-illumination (Tokunaga et al. 2008).

Another possibility to suppress out-of-focus signal is to use a confocal fluorescence microscope. It works by focussing the excitation beam into the sample and uses a pinhole in the emission path to further minimize the detection volume. An image is acquired through a scanning process. As the excitation has an additional PSF-like distribution, the detected signal now consists of a product of two airy patterns leading to an effective $\sqrt{2}$ -fold increase in resolution.

2.1.4 Fluorophores

A fluorescent signal can originate from all kinds of molecules. Cell intrinsic fluorescence for example can originate from amino acids such as tryptophan, tyrosine or phenylalanine. But also, other structures like NAD (nicotinamide adenine dinucleotide) show fluorescent properties.

Nevertheless, more often than not the structures of interest inside a cell are not auto-fluorescent or their fluorescent properties are not suited for efficient excitation and detection. In that case, synthetic fluorophores are used to label the cell extrinsically. It is important to choose the dyes according to the potential auto-fluorescence of the cell to avoid overlapping spectra.

The most common, commercially available fluorescent dyes are comprised of rhodamines, cyanines, oxazines or coumarins. These organic dyes can be designed in such a way that properties like emission and absorption wavelengths, lifetime and quantum yield are optimized for the individual application. Most importantly, they can be functionalized to bind to specific target molecules inside or outside of the cell to label certain structures. These structures can then be imaged with a high level of contrast, provided the fluorophores have a high specificity and the surrounding medium is devoid of freely diffusing dye molecules.

The fluorophore's quantum yield Q describes the ratio between emitted and absorbed photons. Via non-radiative processes, the molecule can reach its electric ground state without a fluorescence photon, which means this ratio is always smaller than 1. It is defined through the rates of radiative Γ and non-radiative κ processes.

$$Q = \frac{\Gamma}{\Gamma + \kappa} \quad (2.9)$$

The fluorescent lifetime τ can also be derived from these variables:

$$\tau = \frac{Q}{\Gamma} = \frac{1}{\Gamma + \kappa} \quad (2.10)$$

As fluorescence can be described as a decay, the time-dependent course of the intensity can be represented as follows:

$$I(t) = I_0 e^{-t/\tau} \quad (2.11)$$

Another key factor concerning fluorophores is their photostability. A fluorophore is called "bleached", when it is unable to express its supposed fluorescence behaviour. This can either happen by a direct photochemical cleaving of covalent bonds or through reactions with the surrounding medium. The excited triplet state of the fluorophore is especially linked to photobleaching. A molecule in this state can more easily react with molecular oxygen that also exists in a triplet state itself, making the

reaction much more likely. A solution for this problem is to use specific buffer solutions that purge the oxygen through reduction.

However, perfect buffer conditions are not always possible to achieve, so that it is often necessary to choose a fluorophore with high photostability that will last for many excitation/emission cycles. While fluorescent proteins usually emit 10^4 to 10^5 photons before bleaching, modern organic dyes last for 10^5 to 10^6 or even more cycles (Greenbaum et al. 2000).

2.1.5 Single Molecule Localisation Microscopy

As described earlier, optical microscopy has an inherent resolution minimum dependent on the wavelength and numerical aperture of the objective. A way to circumvent this limit is presented by so called single molecule localisation microscopy (SMLM) techniques.

The basic principle behind these methods is to successively localise single fluorophores, find their exact position by means of a fitting algorithm and reconstruct a super-resolved image over the course of thousands of acquired frames. The requirement for this to work is that even though the entire structure of interest must be labelled, only a sparse subset of fluorophores can be in the active on-state at a given time. This way the PSFs of the emitters are not overlapping, their exact position can be precisely determined and used to reconstruct a super-resolved image (Figure 8).

Two methods using this underlying idea emerged in 2006, PALM (photo-activated localization microscopy) (Betzig et al. 2006; Hess et al. 2006) and STORM (stochastic optical reconstruction microscopy) (Rust et al. 2006). While PALM achieves the sparsity of emitters through photoswitchable fluorescent proteins, a Cy3/Cy5 dye pair was used in the original STORM publication.

Another method depends on the binding mechanics of specific dyes. PAINT (points accumulation for imaging in nanoscale topography) (Sharonov und Hochstrasser 2006) works by localizing freely diffusing molecules inside the surrounding medium as they bind and become immobilized for a short periods of time at the outside of the cell membrane.

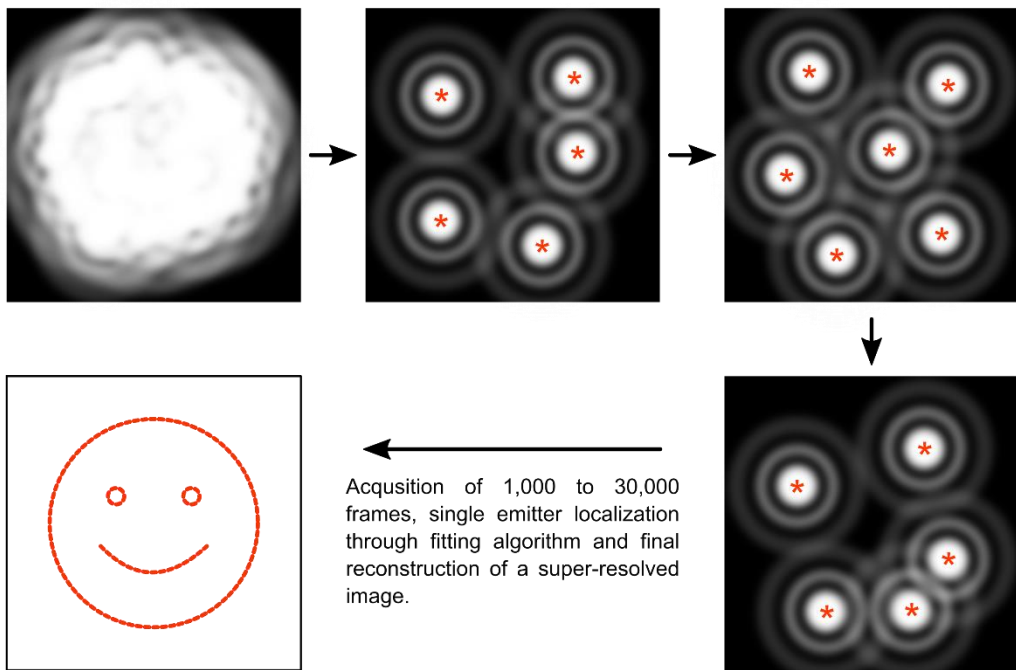


Figure 8: Illustration of the SMLM principle. We start on the top left with an unresolvable widefield image. If we then – e.g. through photoswitchable dyes – are able to image a subset of single not overlapping emitters, we can find their exact locations via a fitting algorithm. All these localizations can then be displayed in a virtual smaller pixel-grid, forming a super-resolved image.

dSTORM

The original STORM system made use of the interactions of the two organic cyanine dyes Cy3 and Cy5. Red laser excitation was used to localise the Cy5 molecules and also to put them into the fluorescent off-state. A green laser source was used to excite the Cy3 molecules that in turn switched the Cy5 fluorophores back to the on-state. These processes are linearly dependent on the laser powers, which allows a relatively easy adjustment of the desired sparsity of active emitters. This setup however is generally quite restricted due to a limited number of suitable dye pairs. Additionally, they also have to have the looked-for properties to label the structures of interest.

Soon after the original publication, it was reported that a whole range of commercial dyes could also be used to achieve the wanted sparse blinking behaviour: dSTORM (direct STORM) (Heilemann et al. 2008) works with only a single fluorophore. Its blinking behaviours are mostly influenced and adjustable by the

surrounding buffer solution and the illumination intensity. This can be explained with a look at the Jablonski diagram. When a molecule is in the long-lived triplet state, it cannot fulfil its fluorescent cycle and is considered “off”. Having a thiol like cysteamine in the imaging buffer is used to further adjust the lifetime of the off-state by quenching the fluorophore. A higher concentration will lead to more inactive dye molecules. At the same time, an oxygen scavenger system is used to save the now longer excited states from irreversible redox reactions. The rate of all reactions is proportional to the excitation power with which the sample is illuminated. A higher laser power will lead to more emitted photons but also more fluorophores switching to the non-fluorescent triplet “off-state”. To adjust this ratio during imaging - but decreasing excitation power is not an option due to e.g. low signal-to-noise ratio - a second illumination source can be applied. E.g. a 405 nm or 488 nm radiation will bring some fluorophores back into the on-state.

In contrast to STORM, this flexibility opened the door to countless new applications, since many dSTORM compatible dyes already existed and were available with various functionalizations to label a wide range of structures in cells. However, the dependency on certain buffer conditions also leads to new problems. Live cell imaging proves to be a huge issue, since oftentimes the required buffers for an optimal fluorophore behaviour are toxic for cells. But as we assess the whole imaging process, the high illumination power in addition to long acquisition times are equally as problematic (Wäldchen et al. 2015).

PAINT

In contrast to PALM and STORM, where the intrinsic switching and blinking behaviour of fluorophores is used to create a sparse subset of active dyes, PAINT uses its binding kinetics. Originally, the PAINT principle was applied by having fluorophores in solution bind and unbind to the membrane lipid bilayer of cells (Sharonov und Hochstrasser 2006) (Figure 9). The virtually infinite supply of dye molecules in the solution allows image acquisition over long periods of time and has yielded resolutions down to 25 nm. It should be noted though, that the abundant fluorescent molecules in the surrounding medium lead to elevated background levels. This is why PAINT is always exclusively illuminated by a HILO configuration.

More recent approaches were able to manifold the possibilities by imaging different membrane molecules at the same time with uPAINT (Giannone et al. 2010) (universal PAINT) or by using short DNA pieces to achieve the required transient binding properties (DNA-PAINT) (Jungmann et al. 2014). Here, a short DNA strand

is attached to a structure inside a fixed cell through an antibody. A complementary strand is labelled with a fluorescent dye and upon temporary hybridization, a fluorescent signal can be acquired and the position localized. Until now however, this method is restricted to fixed cells. Because the fluorophores must be available abundantly around the labelled structures, the cells have to be permeabilized in order to supply fresh dye-DNA complexes.

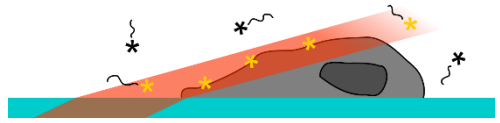


Figure 9: Original PAINt principle. The cell is illuminated by a highly inclined light sheet to maximize the signal-to-noise ratio. Excited fluorophores (red stars) will be registered as localizations only if they are immobilized on the cell membrane. Freely diffusing ones will contribute to a non-specific background.

Reconstruction

Image reconstruction, i.e. the reassignment of localisation coordinates to a new, finer pixel-grid, is the same with all techniques introduced before. Today a vast selection of software packages, plugins and programs exist (Sage et al. 2015). In this work I am using the free ImageJ (Schindelin et al. 2015) plugin ThunderSTORM (Ovesný et al. 2014) exclusively.

First, the raw image is processed by an averaging wavelet-spline filter which suppresses noise artefacts. This makes the next step much easier, which is finding potential localisation candidates by a simple local maxima calculation within 4 or 8 connected pixels. With the potential number of localisations refined to a reasonable number of candidates by these two filtering steps, the computationally most demanding final algorithm can now be performed more efficiently. The local maxima data is fitted with sub-pixel accuracy by a two-dimensional Gaussian as an approximation of the PSF's Airy pattern:

$$f(x,y) = \frac{A}{2\pi\sigma^2} \exp\left(-\frac{(x-x_0)^2-(y-y_0)^2}{2\sigma^2}\right) + b \quad (2.12)$$

A is the amplitude of the signal and corresponds to the number of photons emitted by the molecule. x_0 and y_0 are the new sub-pixel coordinates of the centroid, i.e. the localisation of the molecule. σ stands for the width (standard deviation) of the pattern and b corresponds to the surrounding background level. While the sub-pixel coordinates are in essence the only things necessary to reconstruct a super-resolved

image, the other parameters can and should be used to filter the results and achieve a better image quality.

Noise

The final localisation precision r is not only dependent on the standard deviation σ of the determined Gaussian fit. Noise of different origins also plays a major role in this. The first contribution is due to the quantized nature of light. Since each pixel of the camera only registers discrete chunks of light, i.e. photons, this leads to a discrete intensity which shows the characteristics of a Poisson distribution. This fundamental uncertainty underlying all measurements (also called shot noise) scales with a factor of $\frac{1}{\sqrt{N}}$, where N denotes the number of detected photons.

Since the camera chip has a physical pixel size a and it cannot be determined where exactly a photon hit the pixel, an inherent uncertainty manifests itself in this aspect as well. It can be modelled with a top-hat distribution and amounts to $\sqrt{\frac{12a^2}{N}}$.

The final contribution is the level of the background noise b consisting of various factors such as read noise and dark current of the camera, other fluorescent sources and residual excitation light. It was derived by Thompson et al. in 2002:

$$\sqrt{\frac{8\pi\sigma^2 b^2}{a^2 N^2}} \quad (2.13)$$

If we put the three different contributions together, we obtain the complete theoretical model of the localization precision r :

$$r = \sqrt{\frac{\sigma^2}{N} + \frac{a^2}{12N} + \frac{8\pi\sigma^2 b^2}{a^2 N^2}} \quad (2.14)$$

However, this model has proven to overestimate the attainable precision by 30%. An updated version of this formula was found to be more accurate and in agreement with simulations and actual experiment data (Luo et al. 2017):

$$r = \frac{\sigma_a}{\sqrt{N}} \sqrt{\frac{16}{9} + \frac{8\pi\sigma_a^2 b^2}{a^2 N^2}} \quad (2.15)$$

With $\sigma_a = \sqrt{\sigma^2 + a^2/12}$.

Labelling Density

Another important parameter of SMLM methods is the labelling density. In order to reach a certain resolution, the Nyquist-Shannon sampling theorem states that the density of localized molecules has to be twice as high (Fitzgerald et al. 2012). This theoretical ratio assumes a homogeneous distribution along the labelled structure. For a more realistic, random distribution of dyes, at least a five times higher density is required (Legant et al. 2016).

This is a fundamental problem, as an increased labelling density can cause the PSFs of single emitters to overlap more frequently. This makes changes in the switching behaviour necessary. Off times have to be increased which in turn ensues longer imaging times.

2.1.6 3D STORM

So far, the presented techniques only increased the resolution in lateral dimensions. The axial resolution remains the same as that of common epifluorescence microscopy and can be approximated with

$$d = \frac{2 \lambda n}{\text{NA}^2}, \quad (2.16)$$

while n is the refractive index of the immersion medium between objective and cover slip (Kubitscheck 2013). Other illumination modes like TIRF or HILO are able to limit the detection volume. But within this volume the same resolution limit is applicable.

To obtain 3D information out of localisation data in STORM and similar techniques, one has to introduce an optical element into the system that brakes the axial symmetry of the emitter's PSFs. One way to achieve that goal is by having a cylindrical lens inside the detection path of the microscope and introducing a slight astigmatism. Therefore, the PSF is elongated along the x or y axis depending on the position of the emitter in relation to the imaging focus (Figure 10 a). The distance of the emitter to the focal plane can be calculated by the ratio of the elongation.

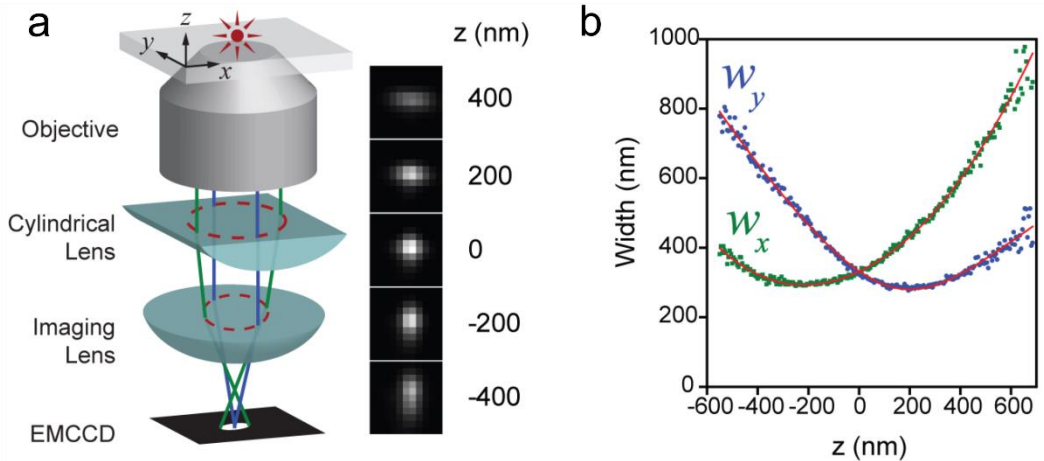


Figure 10: The principle of 3D STORM taken from Huang et al. 2008. (a) By introducing an astigmatism through a cylindrical lens, the PSF shows an axially asymmetric elongation along the x and y-axis depending on the focal position. (b) The width of the PSF in x and y-direction (w_x and w_y) plotted against the axial position of the emitter. These curves are generated by imaging a sub-diffraction fluorescent bead through optical sectioning. They are used as a calibration for later experiments. Depicted in red are fourth-order polynomial fits.

Resolutions of 20 to 30 nm laterally and 50 to 60 nm axially have been reported (Huang et al. 2008).

The reconstruction of these images happens analogously to 2D reconstruction and can be done with ThunderSTORM as well. Only that except of the symmetric fit function, a rotated elliptical Gaussian is used to fit the localization data. Thus, the information of the orientation and amount of ellipticity can be extracted and used to place the emitter in three dimensions.

Prior to the experiments a calibration curve has to be recorded by imaging sub-diffraction fluorescent beads. A z-stack of about $2\mu\text{m}$ and a sampling rate of 10 nm proved to be sufficient (Ovesný et al. 2014). (Figure 10 b) shows an example of the calibration curves fitted by a forth order polynomial.

An additional calibration step has to be done because of the refractive index mismatch between immersion oil medium and sample medium (Diaspro et al. 2002; Besseling et al. 2015). Light from within the sample will be diffracted at the sample/cover glass interface towards the optical axis. This variable angle in conjunction with the varying thickness of immersion medium due to the focussing process leads to an apparent elongation of the imaged structure along the optical axis. The scaling factor h was previously simulated based on (large-angle) geometrical optics (Visser und Oud 1994) yielding

$$h = \sqrt{\frac{n^2 - \text{NA}^2}{n_{oil}^2 - \text{NA}^2}}, \quad (2.17)$$

with n and n_{oil} standing for the refraction indices of the sample medium and the immersion oil. However, this formula proved to vastly overestimate the magnitude of elongation for high NA objectives and it was found that the paraxial approximation of this formula

$$k = \frac{n}{n_{oil}} \quad (2.18)$$

works much better albeit slightly underestimating the mismatch ratio (Besseling et al. 2015).

2.2 Nanoinjection

The nanoinjection method described in this work originated from scanning ion conductance microscopy (SICM) (Hansma et al. 1989). A hollow glass capillary pulled on one side to a fine tip - usually in the 100-nm regime (called a nanopipette) - is used to probe the topography of a sample inside an electrolyte solution. This is done by placing electrodes inside the pipette and an electrolyte bath, applying a small voltage of a few hundred mV and monitoring the emerging ionic current. Changes in this current indicates a change of the environment close to the pipette tip and thus, with a scanning procedure, a topological map can be created.

With more recent approaches it became apparent, that it was not only possible to passively monitor the current, but to actively place molecules onto (cell-)surfaces by driving them out of the nanopipette via electrophoresis (Bruckbauer et al. 2002; Hennig et al. 2015a). The next step was to inject molecules directly into the cell by penetrating the cells membrane beforehand. However, the ability to monitor the ionic current while injecting remained an important feature – it enabled to determine the exact location of the pipette tip relative to the cell surface and whether it is already inside of the cell or still on the outside (Laforge et al. 2007; Hennig et al. 2015b). Another difference to microinjection is, that the pipette is oriented along the optical axis of the microscope. While making axial positioning of the pipette harder – in contrast to microinjection, where the entire pipette tip can be seen through the

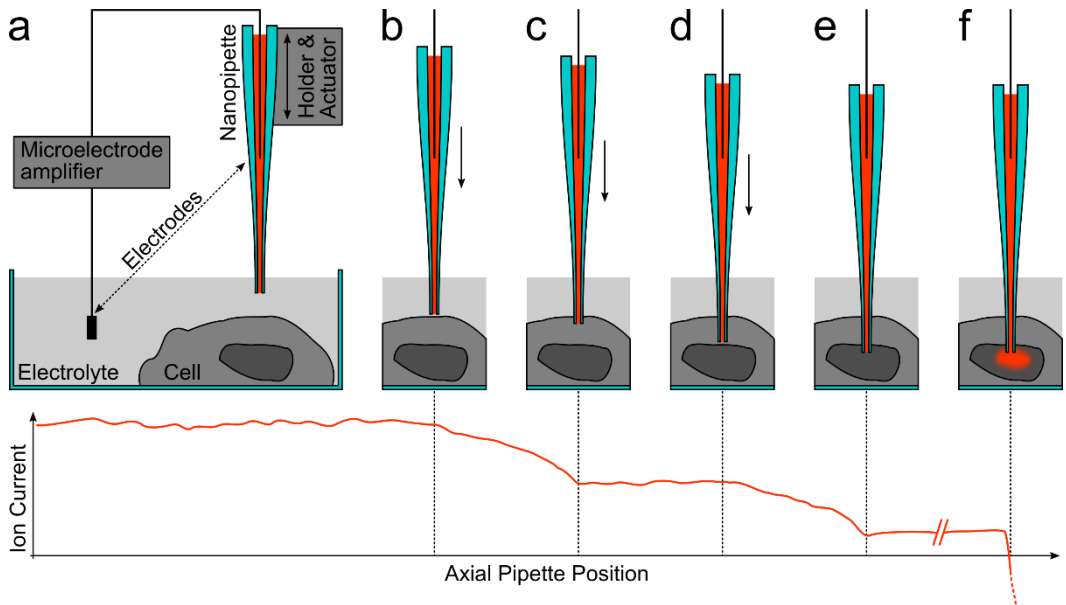


Figure 11: Nanoinjection principle. On top a schematic side view of the injection procedure. Below the corresponding ion current approach curve. (a) Minimal nanoinjection setup. The main components are the microelectrode amplifier with connected electrodes and the pipette holder and actuator. Both are controlled and synchronized by a computer not depicted. This is the initial state with the pipette filled (shown here as red dye solution) and positioned directly over the target cell. For all steps, the ion current is shown below dependent on the pipettes axial position. (b) As the pipette moves towards the cell membrane, the current begins to drop due to the additional resistance. (c) Upon penetration, the current stops decreasing. (d) Due to the nuclear membrane, the current decreases again as the pipette moves closer. (e) Another stop in decreasing ion current marks reaching the inside of the nucleus. Movement is now stopped. (f) The voltage is reversed and increased. With this, the actual injection of is started via electrophoresis.

microscope at an angle – it allows for precise lateral alignment. This is especially important for targeting cell organelles like the nucleus.

2.2.1 Injection Procedure

Nanoinjection always follows the same steps (Figure 11). First, the pipette is manually placed a few μm (usually around $20\mu\text{m}$) above the target. For common, adherent cells this leaves a gap of a few μm between the tip and the outer cell membrane. Now, a small voltage in the range of 100mV (depending on the conductivity of the used electrolyte) is applied to the electrodes. This causes a small

ionic current of 1 to 5 nA to emerge - which is crucial for the feedback system. It is important to choose the direction of the voltage according to the injected solution. The electrophoretic force should face inwards to avoid premature leaking of the target molecules. Then, either pipette or sample are moved towards each other via a means of automated actuation e.g. a piezo-driven stage. Simultaneously, the ion current is recorded and monitored. As soon as the tip is near the cell membrane, the physical barrier leads to a distinct drop in the current signal. After a short time, the current stops decreasing and plateaus or slightly increases again. This indicates the arrival of the tip inside the cytoplasm of the cell. Now, the voltage can be reversed and adjusted for electrophoretic injection of the molecules from the pipette. Optionally, previous steps are repeated within the cell to deliver directly into the cell's nucleus. Here, the nuclear membrane causes another drop in current and provides the needed positional feedback.

Usually, the current decreases by one third per membrane for adherent mammalian cells. While the exact shape of the approach curve is highly dependent on the individual cell – height, morphology and cell cycle influence the geometry of the membranes –, the general appearance is in most cases the same, which is imperative for the reproducibility of this technique.

2.2.2 Molecule Kinetics inside a Nanopipette

As we venture to smaller dimensions, interactions and physical effects are not always intuitively explained. Therefore, we cannot compare the nanopipette system with the more macroscopic workings of e.g. gel electrophoresis (Thorne 1966). Other parameters like dielectrophoresis, electro-osmosis or the geometry of the electric field inside the pipette have to be considered as well.

Electrokinetic Phenomena

Electrophoresis describes the motion of charged particles in a fluid induced by a surrounding electric field. It was first reported in the 19th century by Strakhov and Reuss (Reuss 1809). They observed small clay particles to migrate under the influence of an external electric field.

Following Coulomb's law, an electrically charged particle experiences a force F_{el} proportional to its charge and the surrounding field. However, its motion is also

influenced by the viscosity of the surrounding medium η and the particle's zeta potential. The contribution of the viscosity is intuitively explained by Stoke's drag force F_{drag} that points in the opposite direction of the particles direction of movement. The zeta potential describes the electrokinetic potential of the double layer surrounding the particle. This double layer forms in electrolyte solutions, where all surface charges are screened by a diffuse layer of ions with the opposite charge. If an electric field is applied, it will also exert a force in the opposite direction on these loosely bound ions. While this force is not applied directly on the original particle, it will feel a retardant force F_{ret} through viscous stress. The complete force equilibrium is expressed as

$$0 = F_{el} + F_{drag} + F_{ret}. \quad (2.19)$$

However, the retardation force is only relevant for larger, macroscopic objects and can be dismissed for molecule sized particles with relative certainty (Landers 2007). This leads to a simplified formula and thus, the electric mobility $\mu = \frac{v}{E}$ can be derived as follows,

$$F_{el} = QE = 6\pi\eta rv = F_{drag} \quad (2.20)$$

$$\Leftrightarrow \frac{Q}{6\pi\eta r} = \frac{v}{E} = \mu, \quad (2.21)$$

where v denotes the particle's velocity, Q its overall charge, and r its radius.

A different electrokinetic effect is presented with electro-osmosis. An electro-osmotic flow (EOF) is occurring due to the nature of electrolyte solution and surface charge of the (in this case) borosilicate glass capillary. This surface will be negatively charged through the prevalent SiO^- groups and thus, an electric (Debye) double layer of the ions in solution will form. Ions of the opposite charge are attracted to the first surface layer and form the second, diffusely bound layer. It is influenced by the electrophoretic force in the same way as particles in the solution. This leads to a flow of molecules in the vicinity of the glass surface that can potentially be opposed to that of the electrophoretic motion of molecules in solution. Through friction, uncharged or even oppositely charged molecules can be dragged along the EOF. This effect will be stronger for smaller capillary dimensions and has to be considered in nanoinjection. The zeta potential ζ is used to describe the electric double-layer and

together with the dielectric constants of solution ε and vacuum ε_0 the electric mobility of the diffuse layer can be formulated:

$$\mu_{EOF} = \frac{v_{EOF}}{E} = -\frac{\varepsilon\varepsilon_0\zeta}{\eta} \quad (2.22)$$

This is referred to as the Helmholtz-Smoluchowski equation (Li 2004).

Dielectrophoresis describes the effects on neutral particles under the influence of inhomogeneous electric fields. However the forces of this process are weak for small and charged particles compared to electrophoretic and electro-osmotic forces and are not further considered (Mauro 1980).

Simulations

So far it has been very difficult to generate accurate simulations of the processes inside a nanopipette that could reproduce actual experiments. Often the predictions made by the used mathematical models failed to predict the empirical results (Zhou et al. 2017).

Only the distribution of the electric field $E(x)$ within the pipette and in the close proximity of the pipette tip have been found reasonably precise (Ying et al. 2004) (Figure 12 [ǎ](#)). One part of it was only derived through geometric and electrodynamic considerations.

$$E(x) = \frac{V R \tan \vartheta}{(R+x \tan \vartheta)^2} \quad (2.23)$$

ϑ is the inner opening angle of the half-cone shaped pipette, R the opening radius and V the applied voltage. The area from $0.5\mu\text{m}$ in front of to $1\mu\text{m}$ inside of the pipette was simulated by a simple finite element approach and blended with the mathematical model to yield a continuous transition. It reveals a maximum of the electric field roughly 100 nm from the opening inside of the pipette.

A more recent publication (Calander 2009) confirms this model and reports a set of more intricate finite-element simulations that facilitates the simultaneous solutions of the Nernst-Planck, Poisson and Navier-Stokes equations. Additionally, effects emanating from the surface charge of the glass pipette and field effects through the glass walls are taken into account. The results show that under certain

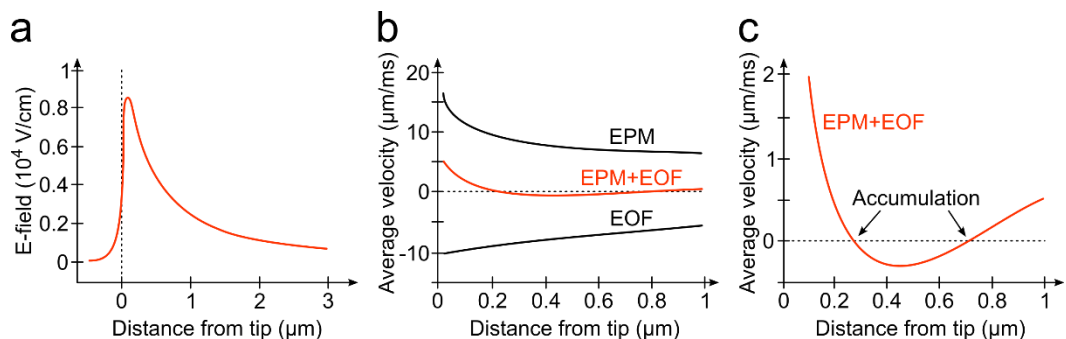


Figure 12: (a) Simulation of the electric field within a pipette. The maximum lies several 100 nm inside the pipette. Data shown for 100 nm inner diameter, 6° opening angle and 1 V applied. Adapted from Ying et al. 2004. (b) Simulation of the kinetics of ions inside a nanopipette. Depending on the charge, of the ions, electrophoretic motion (EPM) and electro-osmotic flow (EOF) can be antiparallel to each other. (c) This can lead to certain areas where the forces cancel each other out and ions accumulate. Adapted from Calander 2009.

circumstances, ions can become trapped in a region of the pipette where electrophoretic and electro-osmotic forces cancel each other out (Figure 12 b,c).

Nevertheless, this publication also states the entire system is not yet able to fully explain all effects. On top of that, the simulations show a very sensitive system. Many parameters such as the opening angle and diameter of the pipette (where deviations of 10% are not uncommon), the size, charge and concentration of the studied molecules or particles all contribute to sensitive behaviour of the system as a whole.

Moreover, detailed information on the molecules (e.g. fluorescent dyes) may not be available making an informed prediction virtually impossible. However, we found that for nanoinjection the net charge of the molecule seems to be the factor that contributes the most and we can assume that it will move according to electrophoretic forces 80% of the time. Otherwise, it is a trial and error situation, so the properties have to be determined empirically. In the case described earlier, where molecules could become trapped in the pipette tip, a simple change of voltage could bring the solution as the electrokinetic forces react differently to variations in the electric field.

3 Survival Rate of Eukaryotic Cells Following Nanoinjection

One of the first steps to a reliable single cell method is to investigate its impact on the health of individual cells. This way following experiments can be executed with greater confidence and reproducibility. But prior to this work there weren't any substantial statistics regarding the long-time effects on viability of injection based methods. That is why I compiled a statistical analysis of single cell survival rate a full day after the injection experiments. Thus, ensuring the organism is given enough time to react to possible harm.

In this chapter, I summarize and extend the results of my first-author paper "Survival rate of eukaryotic cells following electrophoretic nanoinjection" (Simonis et al. 2017).

3.1 Introduction

There are ensemble methods to insert molecules into cells and there are single cell specific techniques. Especially the later would greatly benefit from increased viability, as one is working with a single cell at a time. Nevertheless, the few studies available show a wide range in survival rates. Microinjection for example has reported survival rates of 9% to 56% and 49% to 82% (Davis et al. 2000; Viigipuu und Kallio 2004). Later improvements and automatization of the process could increase the percentage to above 95% (Wang et al. 2008). But there were no further details given

regarding long time viability or how exactly this statistic was generated and controlled. Actis et al. (2014a) reported a viability of 70% just 30 min. after injection using approx. 100 nm nanopipettes similar in size to what I used in this work. But again, there is information missing. A more recent publication describes a statistical analysis consisting of 23 cells from which 8 died (Guillaume-Gentil et al. 2014).

This shows that a more thorough statistic is needed. Only determining the state of injected cells right after the experiment is often not sufficient, as they may die or react hours after being treated. Furthermore, it is not yet clear if or to which extent the probe size correlates with viability, as the 95% survival rate for automated microinjection and 70% for “nanobiopsy” curiously doesn’t indicate this. Thus, I chose to compare two differently-sized pipettes with each other, while also taking other effects like the electric field or injection time into account and waited 24 hours before determining cell viability.

3.2 Method & Preliminary Experiments

As microinjection is used as a standard method in biology and is the quasi-“competitor” to nanoinjection, I compare these two techniques to each other, regarding to the viability of treated cells. In this it is important to realize that I purely compared the different pipette sizes. I didn’t perform any actual microinjection (which is based on pressure and volume displacement) but utilized typical 500 nm micropipettes in the same fashion I used my custom 100 nm nanopipettes. This way the statistics are based only on the size of the probe and can be applied to different conditions and experiments as well.

In search of a reliable way to track cells over the course of 24 hours, I found a cell impermeant dextran construct labeled with a red fluorescent dye (Dextran - Alexa Fluor 647, DAF). This molecule is reported to be non-toxic and can be detected inside cells for several generations (Strehlow und Gilbert 1993). Furthermore, it doesn’t bind to anything specific and spreads through the entire cell, resulting in a highly visible signal on a common fluorescence microscope. The basic idea was to inject the cells with this dye and check a day later whether they are still alive or have died during that time.

All DAF injections in this chapter were performed as described in the theory Chapter 2.2. As target I chose widely available human bone osteosarcoma cells (U2OS). To get a more precise ion current signal for the injection feedback, the cell

culture medium was replaced with pre-warmed PBS prior to the experiments. The nanopipette was filled with 10 μ l of 1 μ M DAF-PBS solution and positioned approx. 20 μ m above the sample. A negative voltage of around -100 mV was applied for the approach. Once inside the cell, the Voltage was reversed and increased to 1 V for 5 to 10 s to drive the dye molecules into the cell. Red (647 nm) laser illumination was used to monitor the process and confirm successful injection. To keep cell stress to a minimum, a heated microscope stage kept the cell culture dishes at 37°C. Additionally, the nanoinjection sessions were constrained to one hour at a time. After that, the PBS was switched again to pre-warmed culture medium and the cells were put back into the incubator. In order to reliably find cells again after 24 hours, I took note of their position by keeping them in a gridded culture dish.

3.2.1 Dextran as a Negative Dead Cell Stain

To show that DAF can be used as an indicator of cell death, I used SYTOX Green (SXG) dead cell stain as a reliable indicator. This dye will only permeate the membrane of dead cells and subsequently bind to the DNA, efficiently staining the nucleus. I injected some U2OS cells with DAF and then observed them for several hours. Additionally, 100 nM SXG was added to the medium. The results can be seen in Figure 13.

As I expected, the large dextran molecules are confined by the cell membrane and stay inside the intact cell membrane of the still living cell, giving a strong red fluorescence signal for the first hours. While the cell starts to die, its membrane becomes corrupted, allowing the unbound DAF to diffuse out of the cell into the medium. At the same time the SXG is able to diffuse into the cell and accumulates at the cell's nucleus where it binds to the DNA. This results in a bright green fluorescence signal. The two effects are happening within 20 min of each other leading to my conclusion, that DAF can indeed be used as a “negative” dead cell indicator via nanoinjection.

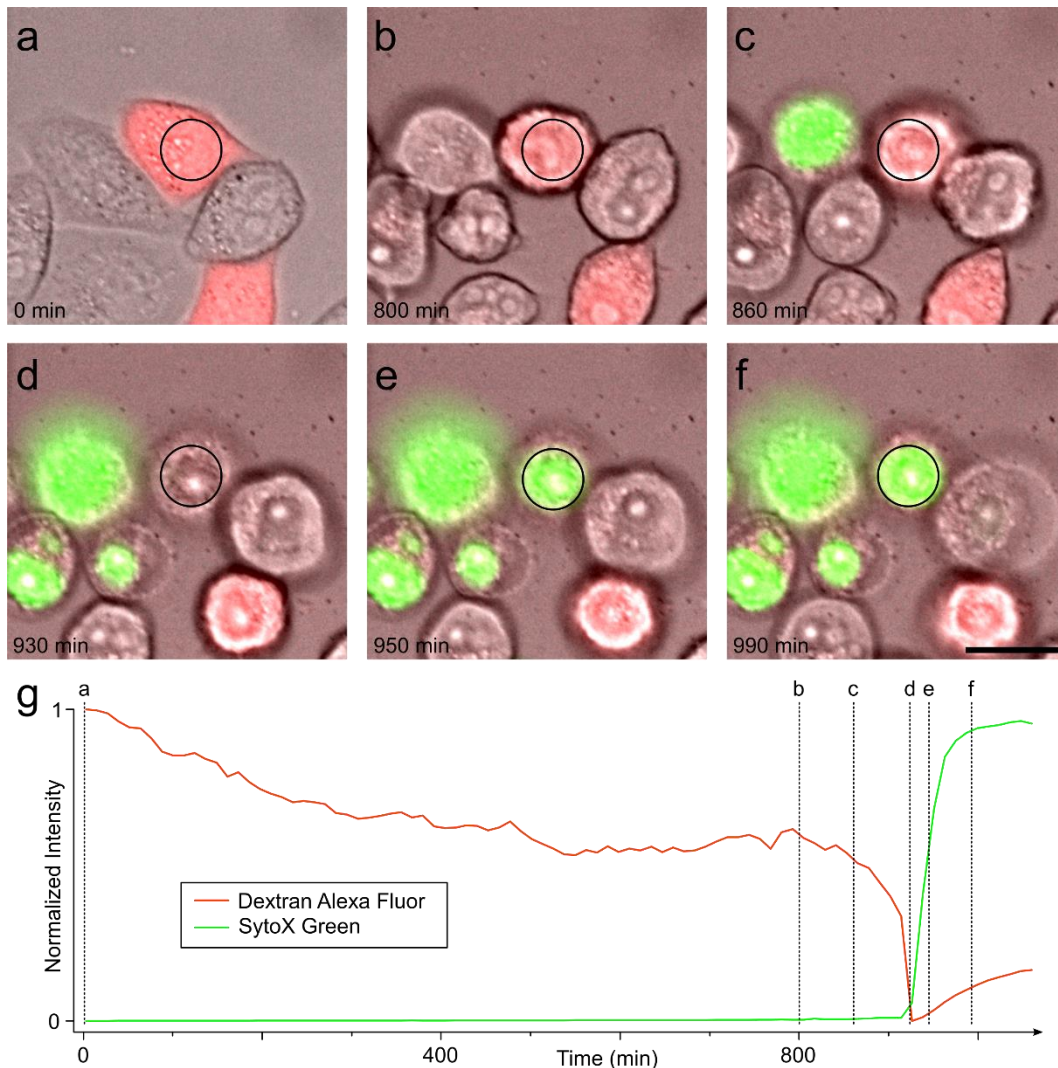


Figure 13: Time-lapse of U2OS cells injected with DAF with SXG inside the medium. Both dyes are membrane impermeant. While SXG labels the DNA, DAF doesn't bind to anything specific inside the cell. (a-f) Overlay of whitelight, red and green fluorescence images of dying U2US cells. Cell of interest indicated by circle. (a) The cell is still healthy and shows typical morphology. (b,c) Rounding of the cell is an indicator of imminent cell death (or cell division). At the same time, DAF molecules diffuse out through the corrupted cell membrane indicated by a decreasing red fluorescence signal. (d) Ca. 2 h after the first signs of cell death, virtually all DAF molecules have left the cell. (e,f) A steep increase in green fluorescence shows that SXG has entered the cell and bound to its DNA. (g) Normalized, average intensity of the green and red fluorescence signal within the black circle. Decrease from a to b is likely due to photobleaching. Scale bar, 20 μm .

3.2.2 Influence of the Electric Field

Because nanoinjection works via electrophoresis by applying a voltage between the inside and the outside of the cell, I also considered the possible negative effect of the electric field by itself on the survival rate. To evaluate this possibility, I measured the survival rate for long injection times with different voltages. For this, I simply loaded the nanopipette with the pure electrolyte (PBS) without any added fluorophores and left the probe inside the cytoplasm for 1 min. and 5 min., while providing a voltage of 0.5 V and 1 V. This way, any ill effects due to the fluorescent dye can be ruled out.

Otherwise, the injection took place as described earlier. After this simulated injection, the cells were continuously observed under cell culture conditions for 24 hours. Acquiring a whitelight image every 20 minutes made sure I could track every cell, even though they weren't providing any additional fluorescent signal. I was careful to use low light intensities and small integration times to keep phototoxicity effects to a minimum. The results of this test can be seen in Figure 14.

For an injection time of 1 min., the voltage has a negligible effect on survival rates: 94% (1 V) and 97% (0.5 V) lay well inside or above the expected control viability (N=184, 94%). Only for the 5 min. "injections", an effect is noticeable. 85% of the cells survive when using 500 mV and only 49% for 1 V. Because I only need 5-10 s to inject sufficient amounts of DAF into the cells for tracking, I can now safely assume that the electric field does not contribute to or has only a negligibly effect on my main survival statistics.

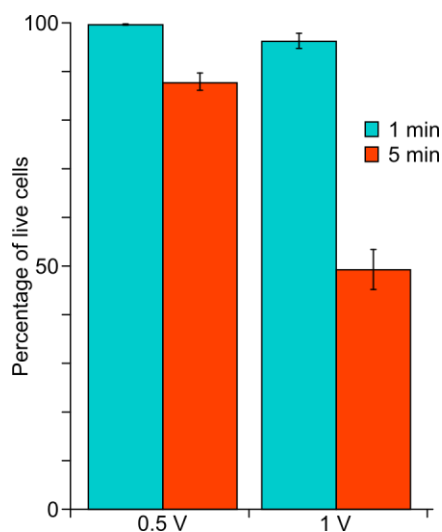


Figure 14: Statistics of cell survival after injection with two different timings and voltages. We used our 100 nm nanopipette loaded with PBS only, to simulate injection. The pipette was left inside the cell for either 1 or 5 min. while a voltage of 500 mV or 1 V was applied. Viability was determined 24 h after injection. The 1 min. "injection" shows negligible effect regardless of the voltage compared to a control population of cells: 94% (N=35) for 1 V and 97% (N=32) for 500 mV. After 5 min., a higher mortality emerges: Only 85% (N=17) and 49% (N=26) cells survive when treated with 0.5 and 1 V respectively.

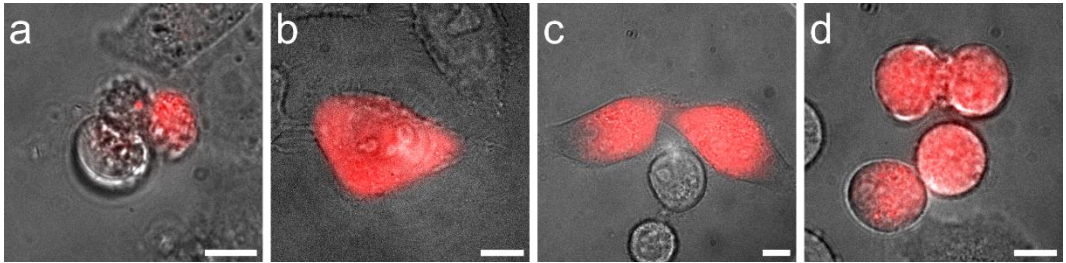


Figure 15: Overlay of whitelight and red fluorescence images of U2OS cells. These images were acquired 24 hours after the cells were injected with DAF. We used a gridded culture dish to relocate the cells. (a) Judging by its morphology this cell can be presumed dead even if residues of the dye are still visible. (b) Healthy cell with distinct fluorescence signal. (c) Two cells at the initial injection site which implicates a cell division. (d) When two divisions took place during the 24 hours, four cells can be found. Here, they are just finishing mitosis. Scale bars, 10 μm .

3.3 Survival Statistics

For my main survival statistics, I further differentiated between cytoplasmic injection and injections directly into the cell's nucleus. This is interesting, as nuclear injections can provide a better or the only way to deliver certain molecules to their destination. As described before, I used DAF delivered by a micro- and a nanopipette (500 nm and 100 nm inner tip diameter respectively) to be able to determine the cells status 24 hours after injection.

There are several possibilities to what I could observe after that time (Figure 15): 1) The cell is still alive after 24 hours and can be found easily near the area of injection via its red fluorescent signal. 2) If two or more cells express a red fluorescence, the cell proliferated once or twice. 3) No signal can be seen – either the cell died and the DAF diffused into the medium and/or the cell detached from the substrate. I never observed any living cells mobile enough to move out of the field of view, so either way it is counted as dead. 4) Sometimes dead cells can leave some residual fluorescent signal behind. But due to their different morphology they can easily be distinguished from healthy cells and count as dead as well.

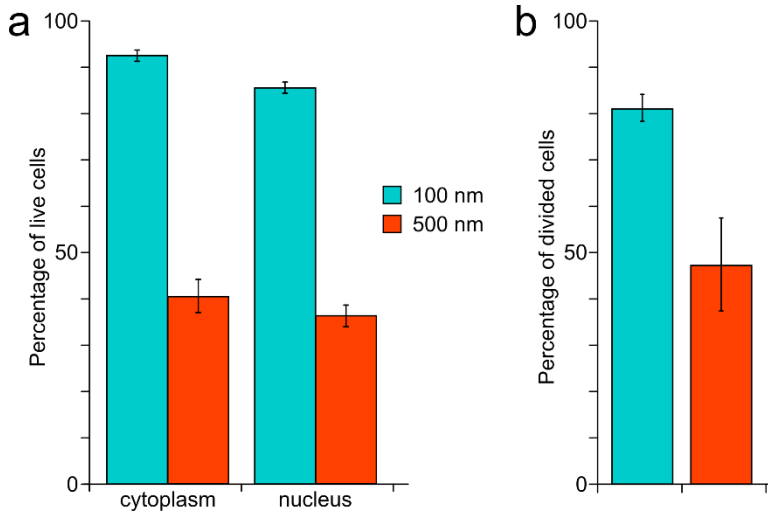


Figure 16: Cell state 24 hours after injection with 100 nm and 500 nm pipettes. One batch of injections was restricted to one hour at a time to keep cell stress to a minimum. Additionally, a heated stage kept the cells at 37°C. For injection, culture medium was switched with pre-warmed PBS. (a) shows the percentage of surviving cells one day after the injection. High viability was achieved using our nanopipette. 92% (N=68) for injection into the cytoplasm and a slightly lower 85% (N=71) when injecting into the nucleus. For the larger 500 nm pipette, survival rates were less than half as much with 40% and 36% (both N=50) respectively. In (b) all the surviving cells were compared regarding their proliferation activities. While 81% (N=116) of the nano-injected cells showed proliferation, only 47% (N=36) of the cells treated with the larger pipette divided.

All the following percentages are already corrected for a control population of 184 cells investigated under the same conditions. The natural mortality of our U2OS cells M_{nat} (=6%) is stochastically independent from the mortality induced by nano-injection $M_{inj}(P_{inj})$. Therefore, the probability that a cell dies because it was injected P_{inj} is given by

$$P_{inj} = \frac{M_{inj} - M_{nat}}{1 - M_{inj}} \quad (3.1)$$

Raw, uncorrected data of all survival experiments can be found in the appendix for reference.

The results (Figure 16) reveal a 92% chance of long-term survival for nano-injection (100 nm) into the cytoplasm (N=68). Injection directly into the nucleus amounts to a slightly smaller viability of 86% (N=71). Using the larger micropipette (500 nm) leads to significantly lower rates of 40% and 36% (both N=50) respectively.

Additionally, I compiled a statistic of only the surviving cells regarding their proliferation behaviour during the 24 hours. I found that 81% of the 116 surviving cells treated with the smaller 100 nm tip divided once or even twice during that period. In contrast, out of the 36 surviving microinjected cells, only 47% showed proliferation

3.4 Discussion & Conclusion

I demonstrated that the size of the injection probe has a considerable influence on the survival rate of treated cells. Not only does injection with a larger microinjection pipette lead to a more than doubled mortality, but it also has a measurable influence on the surviving cells as well. Surviving cells out of our control population all proliferated during the 24-hour experiment. Although not being an absolute indicator of the cells well-being, it certainly leads to the assumption, that with over 80% division rate, nanoinjection poses a smaller problem for the cell cycle than microinjection with about half that percentage.

This fact, and that I could determine the long-term viability of nanoinjection to 92% (cytoplasmic injection) for widely used U2OS cells yields good prospects for further experiments with more fragile cell lines or precious primary cells. As I determined that the electric field only influences viability for injection times longer than one minute and with a high voltage of 1 V, the increased mortality in my statistics can be attributed to the injection of dye molecules itself with reasonable certainty. This could be used generate studies regarding the toxicity of certain dyes or other molecules, when other factors like phototoxicity can be ruled out.

The slightly lower survival rates of nuclear injections are evident in both probe sizes. But the minimal, insignificant differences lead to the conclusion that overall, the target of injection isn't relevant. Maybe the main factor contributing to changes in survival rate is the amount of destruction done to the outer cell plasma membrane. It seems like a damaged nuclear membrane doesn't further decrease viability.

Further decrease of the nanopipette size could possibly lower the mortality even more. For example, carbon nanopipettes (Singhal et al. 2011; Schrlau et al. 2008): These are fabricated like normal glass pipettes but with a subsequently added robust carbon tip that can go down to some tens of nanometres in diameter. Even with the same fabrication method I used, it is theoretically possible to go as low as 10 nm (inner diameter). This requires quartz glass capillaries. But apart from a more costly

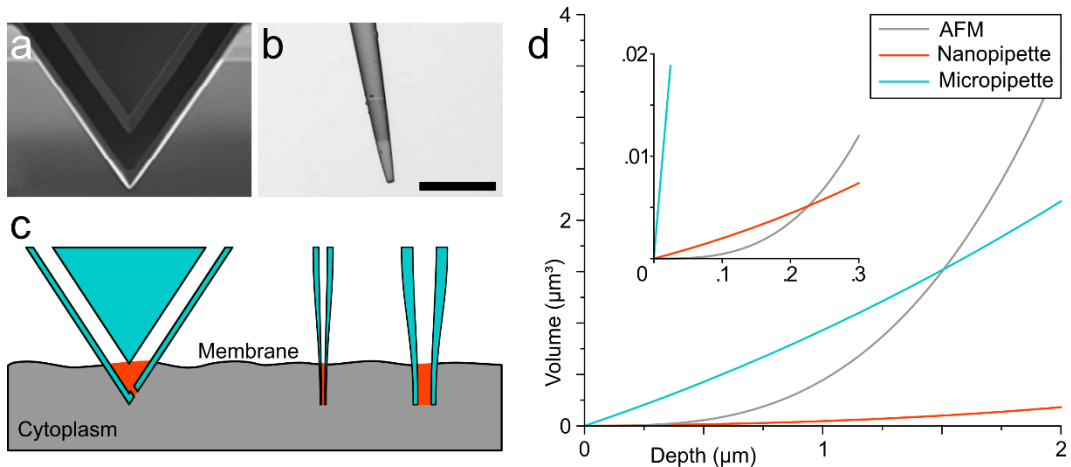


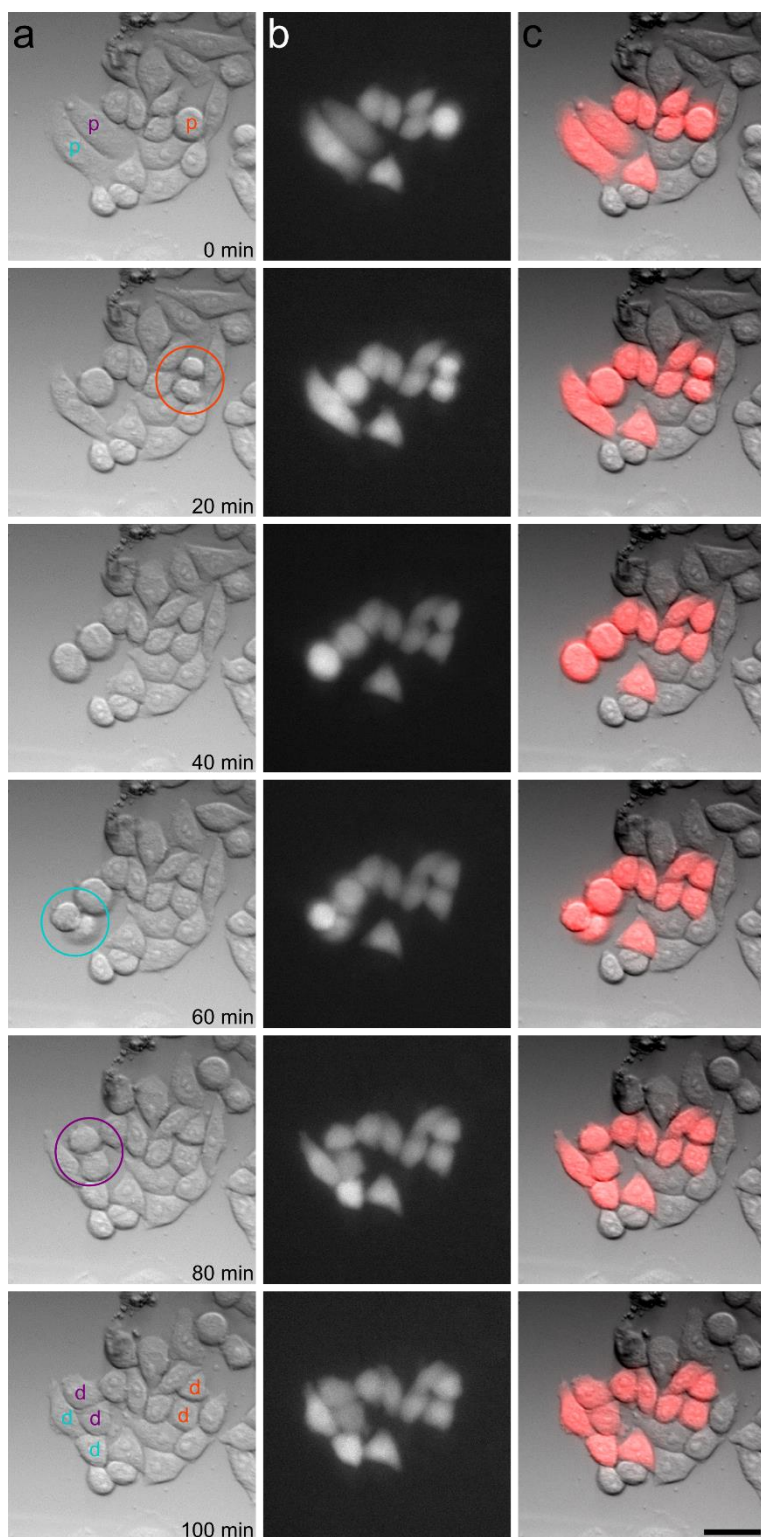
Figure 17: Size comparisons of different injection probes. (a-c) SEM and schematic images to scale. Scale bar, 3 μm. (a) FluidFM cantilever (Guillaume-Gentil et al. 2014) (b) Glass nanopipette (Ying et al. 2004) (c) FluidFM cantilever, 100 nm nanopipette and 500 nm micropipette ca. 1.5 μm deep inside the cytoplasm. (d) Mathematic model for visualizing the volume displacement dependent on penetration depth. For the AFM, we modeled a pyramid shape with an opening angle of 30°. A truncated cone with a 5° angle was used for the glass pipettes. For outer diameters, we took 150 nm and 1 μm which corresponds to the actual probes. The small opening angle leads to an almost linear behavior of the pipettes. AFM and micropipette have the same volume at a depth of 1.5 μm. The inset shows that nanopipette is only worse for the first 200 nm.

and difficult manufacturing process, going smaller comes with a set of new problems. The reproducibility certainly suffers from my experience (deviations of 20% for pipettes with an inner diameter of 20 nm), leading to varying results in application. And, after reaching a certain size, the scale of the injected molecules itself becomes an issue. Antibodies with sizes of around 10 nm would cluster and clog the pipette. I think, that pipette sizes around 100 nm are the sweet spot, where viability is sufficiently high and a wide range of molecules can be injected. If problems with clogging appear, one could increase the tip diameter and sacrifice a low mortality. Alternatively, if viability is extra-critical, using a smaller pipette could prove beneficial if the injected molecules allow it.

On the other side, there is the completely different probe architecture of AFM-based injection methods. Unfortunately, there aren't any survival statistics going further than N=23 with a mortality rate of 35%, which may be due to the inherent geometry of AFM cantilevers. Though the inner tip diameter of the FluidFM (Meister et al. 2009) probes is the same with around 100 nm, the cross-section of the pyramid-shaped form grows larger much quicker than a glass nanopipette (Figure 17). This

leads to a larger penetration area and an even larger volume displacement. I estimate the difference to be ten-fold when the probe has penetrated $1\ \mu\text{m}$ deep into the cell. Compared to the larger $500\ \text{nm}$ micropipette, the AFM cantilever displaces the same volume in a depth of around $1.5\ \mu\text{m}$. For nuclear injection, this is close the minimum distance to successfully target the nucleus. Thus, it seems reasonable to assume a survival rate of treated cells close to what I determined for micropipettes. Although the blunt tip of the pipette might contribute to the elevated mortality, the foreign volume inside the cell increases drastically for the AFM probe for deeper injections. These become especially relevant for injections into the nucleus.

Figure 18: 100 min. time-lapse of U2OS cells injected with DAF. Row (a) brightfield, (b) red fluorescence and (c) overlay. Parental cells are marked with a “p”. Circles indicate proliferation events and “d” shows the resulting daughter cells. Scale bar, $40\ \mu\text{m}$.



4 Development of a Mobile Nanoinjection (MoNa) System

As mentioned in a previous chapter, nanoinjection originated from scanning ion conductance microscopy (SICM) and therefore our injection setup - as most others - makes use of the SICM equipment already at-hand. However, this comes with a set of problems, because the gear is not very flexible and relatively expensive. On top of that, the benefits of having extremely low noise levels in the ion current measurements and sub-nanometre positioning accuracy are basically irrelevant for nanoinjection.

In this chapter, I show that it is possible to build an injection system that costs 87% less, is completely portable but still retains the same nanoinjection capabilities.

4.1 Motivation

The accuracy with which scanning ion conductance microscopes position the scanning pipette probe tip is only one order of magnitude lower than that of atomic force microscopes (AFM) (Rheinlaender und Schäffer 2009; Binnig et al. 1986). As a result, high lateral resolutions of smaller than 10 nm (axial: < 50 nm) can be achieved (Shevchuk et al. 2006). This precision demands a high-end (fast and accurate), piezo-driven xyz-stage and an additional axial piezo control for the pipette itself (this is necessary for different probing scenarios such as “hopping”-mode). An additional requirement is a microelectrode amplifier that yields a high signal-to-noise ratio (SNR). A combination of preamplifier, amplifier and lock-in amplifier is commonly

used to achieve this goal and gives an optimal feedback. On top of that, a high-frequency, high-resolution analog-to-digital and digital-to-analog converter (ADC/DAC) and software must be at hand to acquire measured data and to control the whole experiment. All this equipment is usually heavy, rack-mounted and therefore lacks flexibility to set up and connect to different workspaces.

But for microinjection and even nanoinjection, this level of precision and speed is not necessary. The size of adherent mammalian cells covers a wide range but is usually not much smaller than $10\ \mu\text{m}$. Even when targeting the nucleus for an injection, a lateral accuracy of around 0.5 to $1\ \mu\text{m}$ proved to be sufficient and can even be achieved by hand with a pair of micrometre screws. Further, an axial resolution of about $50\ \text{nm}$ seems adequate to penetrate a cell even as flat as one micrometre. As speed isn't a high priority, I estimate $100\ \text{ms}$ to be a reasonable for temporal resolution of the control and measurement devices.

Keeping these values in mind, my goal was to build a nanoinjection system, that is easy to carry to different workspaces and doesn't take long to set up, while at the same time not sacrificing stability or functionality. This way, injection experiments can potentially be carried out right where the cells are best observed – in live chambers with controlled atmospheres or on specialized high-resolution systems for example. Hereby, unnecessary sample movement can be avoided and more direct reactions can be monitored.

4.2 Setup

There are four main components to consider when building a nanoinjection system. First, an electrode amplifier that can measure the ion current and apply a set voltage to a reasonable accuracy, so that the unique shape of the approach curve is still distinguishable from noise. Second, a means of positioning the nanopipette with sufficient precision before and during approach. Thirdly, a robust, vibration-proof and flexible foundation to hold the pipette and connect it to the setup. Finally, there is the controller and software to monitor and synchronize the whole injection process.

4.2.1 Electrode Amplifier

For measuring the ion current I opted for a custom-build operational amplifier (op-amp) design (see Appendix A.4 for the detailed circuit diagram). It consists of two consecutive op-amps in a relatively small circuit (approx. 30 parts) that runs on a 15 V power supply or battery pack. Through a rotary switch, four different resistors can be brought in-line which results in different amplification gains. This corresponds to four different current ranges that can be measured: ± 10 nA, ± 100 nA, ± 1 μ A and ± 10 μ A. The amplifier converts the small ion current into a voltage output that is scaled from -10 V to +10 V to fill the entire input range of the ADC. For ease of use, two crocodile clamps coming out of the amplifier can be used to connect the two electrodes. They are mounted on short, flexible cables and allow the setup to adapt to small working areas. The scaled output is connectable via commonly used BNC connectors to the I/O device. To provide a voltage for the electrodes, again a BNC input is available.

4.2.2 Positioning

Positioning of the nanopipette consists of two parts (Figure 19 a,b). Coarse positioning in all three dimensions is done by hand with a set of three micrometre screws and the approach and injection movement itself is automatically driven by a piezo actuator.

I decided to do the manual alignment with a commercially available xyz-stage (ULTRAlign Precision XYZ Linear Stage, Newport Corporation, USA) with a theoretical precision of 100 nm. It was chosen due to its high rigidity and weight, which should dampen vibrations. Also, 13 mm travel range in all dimensions makes it a solid, flexible foundation for the pipette holder. This part is also used in our old SICM system and proved to be vital for this work.

For the injection itself, a second smaller linear stage, actuated by a piezo-driven micrometre screw (P-854.00, Physik Instrumente, Germany), is connected to the manual xyz-block. A piezo-controlled travel distance of 25 μ m is more than sufficient for nanoinjection, where I use 20 μ m at the most. Additionally, the micrometre screw can be used for further manual adjustment along the optical axis. The voltage for the piezo is provided by an appropriate driver (Piezo Driver P-863, Physik

Instrumente), that scales an input of 0 to 10 V up by a factor of ten (0 – 100 V), so that the whole 25 μm of travel range can be used.

4.2.3 Hardware

I designed the connection from the actuating stage system to the pipette holder to add some more flexibility concerning range while at the same time trying not to lose any stability. The final iteration consists of a solid crossbeam on which a second solid piece is able to slide out 2 cm (Figure 4.9 c,d). It is guided and fixed by a peg and a screw which gives it enough rigidity. For axial movement, a cylindrical piece is clamped down at the end. I mostly used a length of cylinder, that led to an adjustment range of about 2 cm as well. A serrated screw going through the cylinder allows for easy connection of the actual pipette holder. This makes it very easy and fast to change the pipettes without any tools. The actual connection with the pipette itself is an already existing design consisting of a two-piece polyoxymethylene (POM, an engineering thermoplastic) holder and a metal brace for connecting it with the rest of the apparatus.

On the other end of the xyz-stage, I designed a set of three massive, 2-cm thick aluminium plates with a typical, optical-table arrangements of M6 threads and some slide rails. In combination with some generic poles, I can position the setup almost anywhere around an inverted microscope with sufficient stability.

4.2.4 Controller & Software

For ease of use and flexibility, my ADC/DAC device (USB-6001, National Instruments, USA) is controllable via USB. The resolution is 14 bits with a sample rate of 20 kHz. Two analog output channels and eight analog input channels are available with a total range of $\pm 10\text{ V}$. It can only provide a maximum current of $\pm 5\text{ mA}$. But because I only expect values in the nA regime and only rarely go to μA , this is more than sufficient to supply the electrode voltage directly. This way I can avoid the need for an additional amplifier.

If we convert the bit-resolution into the actual voltage resolution and apply this to the z-piezo and the current measurement, we get the theoretical limits of the system. Smallest possible voltage change:

$$1 \text{ bit: } \frac{20 \text{ V}}{2^{14}-1} = 1.22 \text{ mV} \quad (4.1)$$

The resolution of the piezo movement is dependent on the input range of the piezo amplifier, which goes from 0 to 10 V, and the total travel range of 25 μm :

$$\frac{25 \mu\text{m}}{10 \text{ V}} \times 1.22 \text{ mV} = 3.05 \text{ nm} \quad (4.2)$$

The op-amp output covers the whole $\pm 10 \text{ V}$ range of the USB device. This leads to the following limitations of current measurements dependant on the selected range.

$\pm 10 \text{ nA}$ range:

$$\frac{20 \text{ nA}}{20 \text{ V}} \times 1.22 \text{ mV} = 1.22 \text{ pA} \quad (4.3)$$

$\pm 100 \text{ nA}$ range:

$$\frac{200 \text{ nA}}{20 \text{ V}} \times 1.22 \text{ mV} = 12.2 \text{ pA} \quad (4.4)$$

$\pm 1 \mu\text{A}$ range:

$$\frac{2 \mu\text{A}}{20 \text{ V}} \times 1.22 \text{ mV} = 122 \text{ pA} \quad (4.5)$$

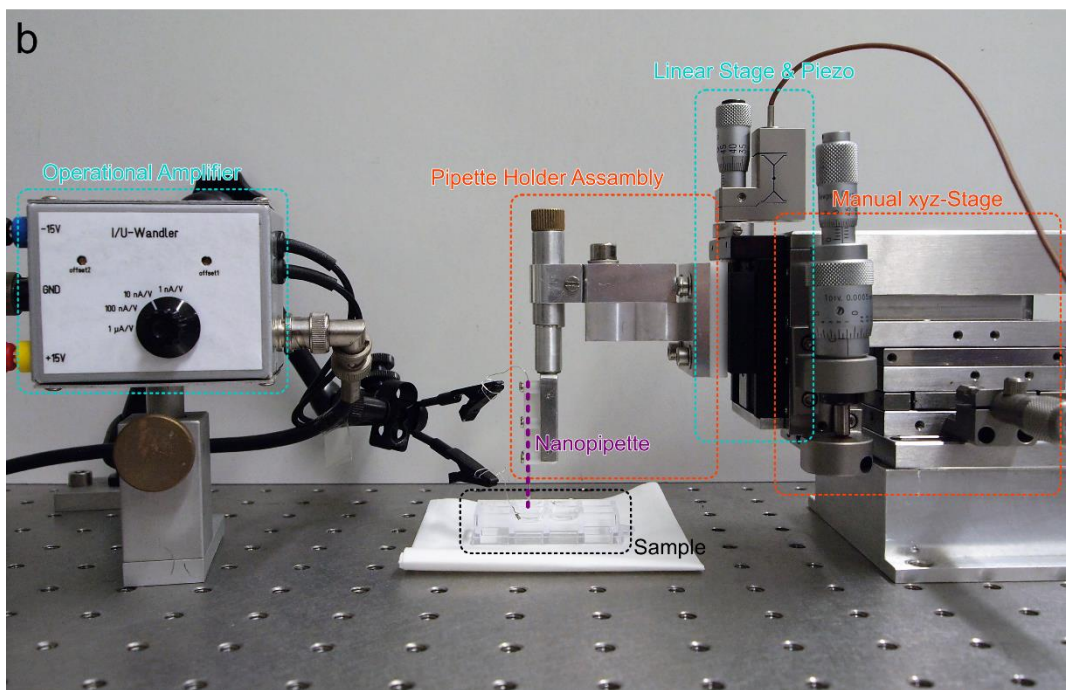
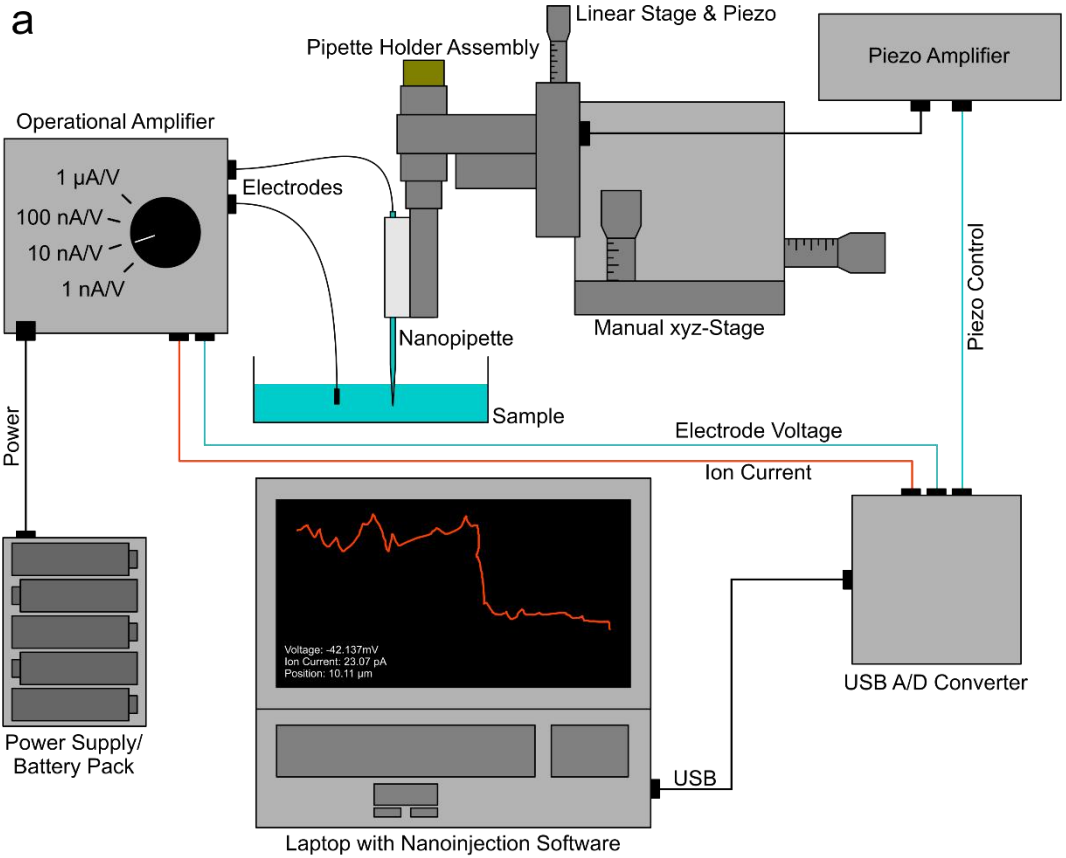
$\pm 10 \mu\text{A}$ range:

$$\frac{20 \mu\text{A}}{20 \text{ V}} \times 1.22 \text{ mV} = 1.22 \text{ nA} \quad (4.6)$$

As mentioned, these are only the theoretical limits of the system. Noise will prohibit this kind of accuracy. For example, the system noise of the USB device alone is 0.7 mV RMS. Each additional element like the op-amp, piezo driver, unshielded cables, etc. will contribute to additional deterioration of the signal. Hence, I measure the noise of the entire signal chain in the following chapter.

The two output channels (electrode voltage and piezo control) and one input channel (current measurement) are displayed and controlled by means of a custom-written software in a LabVIEW (National Instruments) programming environment. A Laptop (Intel i3 processor, 4 GB ram) ensures the portability I am trying to achieve (documentation of the software can be found in Appendix A.3).

The entire setup can be seen in Figure 19 e. Including miscellaneous bits and pieces like cables, screws, batteries, nanopipette boxes, etc. everything still fits inside a large suitcase.



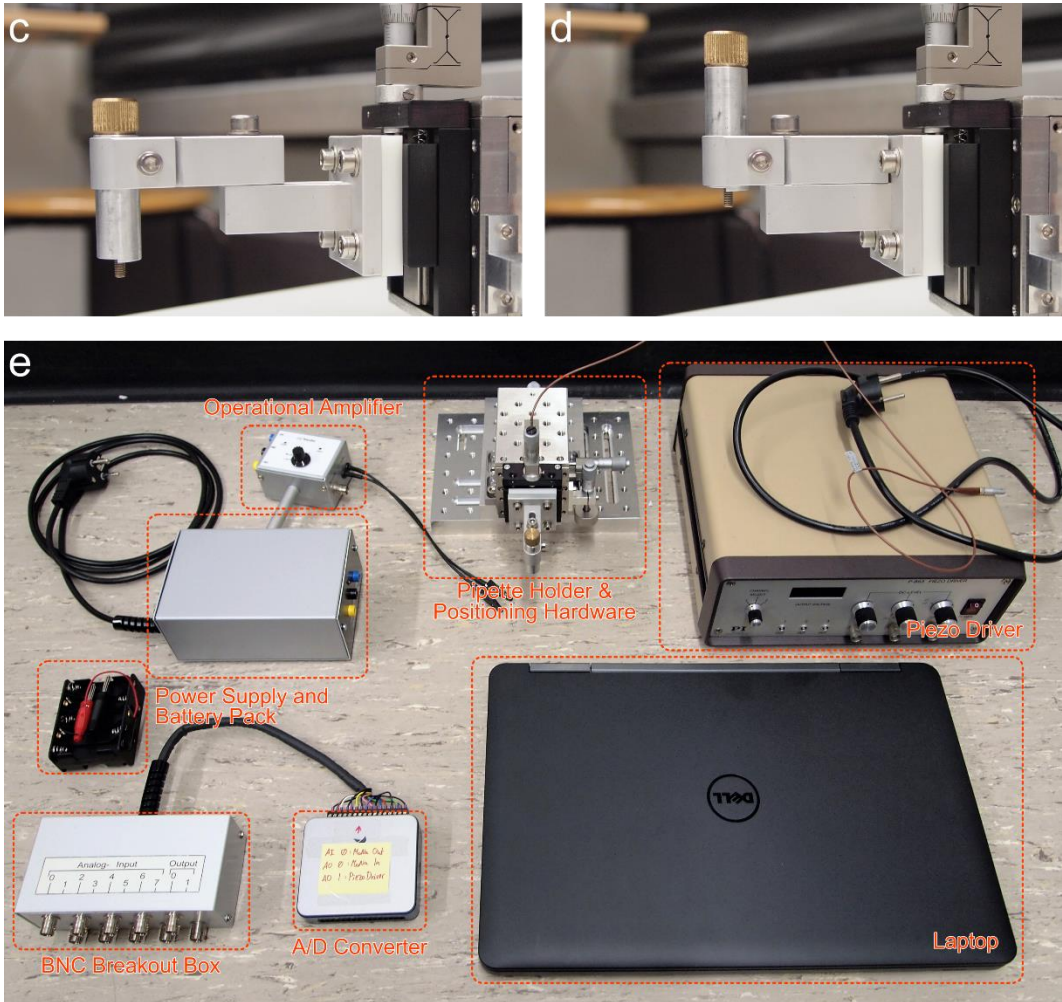


Figure 19: Mobile nanoinjection system parts. (a) Schematic image of the setup. Everything is controlled and monitored by a small data acquisition device connected via USB to a common laptop running a LabVIEW software. The two analog output channels (blue connections) are used to apply voltage to the electrodes and the piezo driver. The only analog input channel (red cable) we need, carries a signal proportional to the ion current from the amplifier back to the DAC device. A 15 V battery pack can be used to power the op-amp. Coarse pipette positioning can be done with the xyz-stage, while fine positioning along the optical axis and approach is handled by a piezo-driven linear stage. The pipette holder allows for 2 cm extra adjustment range. (b) Image of the core parts described in a. You can see the serrated brass screw on top of the holder assembly that is used for separating the lower part of the pipette holder to change out pipettes more easily. (c,d) Detailed close-up of the range achieved by the flexible pipette holder. The cylindrical part and brass screw can be replaced with longer ones for an even bigger reach along the z-axis. (e) Picture of all parts spread out (excluding miscellaneous items such as screws, cables, etc. and the two larger holding plates). With these considerably smaller and lighter parts, it is possible to fit them all in a large suitcase for easy travel.

4.3 Comparison to the Original SICM System

The first thing I did was to characterize the capabilities of my new MoNa system and compare it with what the old, commercial SICM setup could achieve. Reasonable noise levels are the key factor for a working nanoinjection system, because I rely on the ion current to give us accurate feedback of the pipette’s position. I performed five 10-second current measurements (10,000 samples at 1kHz sampling rate) while applying voltages in the range of ± 200 mV, as this is the typical range I use for the injection approach. Inclusion of the entire signal chain from PBS as electrolyte, to the electrodes, amplifier, DAC device and computer gives us a realistic idea of what to expect. The Results (Figure 20) show that compared to the old system (8.08 ± 0.24 pA), the root mean square (RMS) noise values of the MoNa system are only ten times higher with 83 ± 11 pA at the smallest measuring range (± 10 nA). These values are quite remarkable, when considering that the new amplifying and data acquisition equipment is more than 50 times lower in price (Table 1).

A further look at the table shows that roughly a third of the total was spent on the xyz-stage. In retrospect, this was a good decision, as the added weight and rigidity of the massive stage proves to inhibit vibrations very well. The second largest part of the costs ($1/6^{\text{th}}$) is for the LabVIEW development environment. All in all, the MoNa system amounts to about €6000 (including 19% German VAT), which is only 13% of the commercial setup which amounts to roughly €48000.

A key factor in nanoinjection is the ability to derive the position of the pipette from the course of the ion current. That is why I wanted to see how the injection

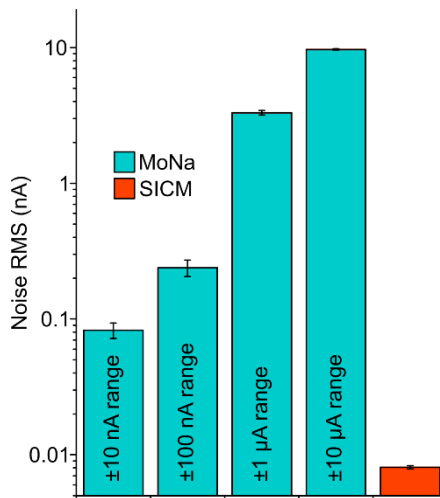


Figure 20: Mean noise levels. Shown are the four different settings of the MoNa amplifier and for comparison the SICM setup. The ion current noise levels were recorded five times each under typical injection conditions, i.e. PBS was used as electrolyte and we applied a voltage in the range of ± 200 mV. Each measurement took 10s and recorded 10,000 samples. Error-bars are the respective standard deviation of the five datasets. The lowest noise levels are achieved by the SICM setup at 8.08 ± 0.24 pA. Depending on the range setting, the mobile nanoinjection system yields 83 ± 11 pA, 239 ± 34 pA, 3.31 ± 0.17 nA and 9.68 ± 0.12 nA.

Table 1: Rough price comparison of our two different injection systems. The main components are compared separately. All prices are inclusive of German VAT (19%). Old prices are approximately corrected for inflation.

Component	Commercial SICM setup		Cost-efficient MoNa system	
	Part	Price (€)	Part	Price (€)
Ion current measurement, voltage control	Axopatch 200B Amplifier + CV 203BU Headstage (Molecular Devices)	11038.00 (2004)	Custom build operational amplifier	~ 40.00 (2016)
Pipette movement (manual)	ULTRAlign Precision XYZ Linear Stage (Newport)	2256.24 (2016)	ULTRAlign Precision XYZ Linear Stage (Newport)	2256.24 (2016)
Pipette movement (automated)	Nano-PDQ375HS + Nano-Drive 85 (Mad City Labs)	28842.00 (2007)	P-854.00 (Physik Inst.) Piezo Driver P-863 (Physik Instrumente)	675.00 (2000) ~ 819.00 (1996)
Analog I/O	NI PCIe-6251 + 2 x BNC-2090 + 2 x SHC68-68-EPM Shielded Cable (National Instruments)	3374.82 (2016)	USB-6001 (National Instruments)	219.29 (2016)
Software	LabVIEW Base Development System (National Instruments)	1013.29 (2016)	LabVIEW Base Development System (National Instruments)	1013.29 (2016)
Miscellaneous	PC, cables, screws, holders, clamps, electrodes, etc.	~ 1000.00	Laptop, cables, screws, holders, clamps, electrodes, etc.	~ 1000.00
Sum		47524.35		6022.82

approach curves of the two systems compared to each other next. For this, I approached a U2OS cell in a PBS environment while applying a typical +100 mV to the electrodes. To get the whole picture, I injected directly into the nucleus. This way, I can also evaluate, if the nuclear membrane is detectable with my new system. The approach speed was set to roughly 1 $\mu\text{m/s}$.

I can still observe the distinct features of the SICM approach curve in the MoNa data (Figure 21). The noise levels are elevated as I expected from looking at the previous experiment. This cloaks the shape of the curve to a certain degree compared to the SICM setup approach, but nevertheless, the different regions are still clearly visible. Overall, the current levels before and after penetration are consistent with each other, starting at around 2 nA and falling approx. 50% to about 1 nA. This leads to my first conclusion, that it is indeed possible to get a comparable, accurate positional feedback of the nanopipette during approach and penetration of living U2OS cells with a much simpler, basic setup.

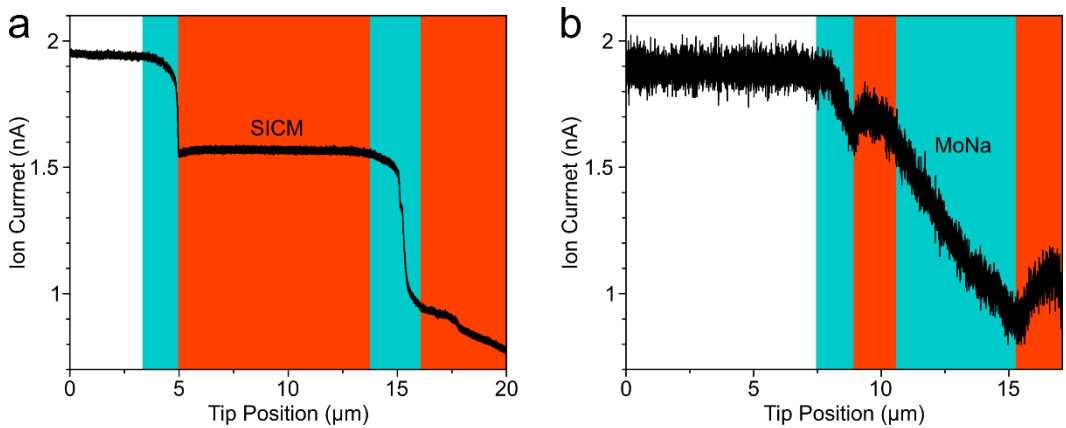


Figure 21: Ion current approach curves of the two different systems. We targeted a U2OS cell directly at the nucleus with a typical voltage of +100 mV and a speed of around 1 $\mu\text{m/s}$. (a) SICM approach. As expected, the current drops (blue) are easily visible and indicate the outer cell and nuclear membrane. These regions are clearly distinguishable from the red regions, where the current only experiences something between a minor de- or increase. (b) MoNa approach. Despite the apparent increase in signal noise, the distinctive features of membrane penetration are still noticeable, albeit not as prominent.

4.4 Injections of Fluorescent Dyes

For the next step, I tested the actual nanoinjection capabilities of my mobile setup. Once again, living U2OS cells were utilised as a typical target. I chose two different fluorescent dyes to show, that the MoNa system indeed works as well as a SICM-based system. I attached MoNa to our fluorescence microscopy setup – a standard inverse wide-field microscope (Olympus IX71, Olympus, Japan) with several possibilities for illumination and detection. The injection process itself wasn't any different from what I was used to.

For the first injection (Figure 22) with Mito Tracker Deep Red (Thermo Fisher Scientific, USA), I had to use an unusually high injection voltage of 2.5 V, as the dye is solved in DMSO, which has a significantly lower conductivity than PBS. But nevertheless, after approx. 10 min. of active staining, the mitochondrial structures were visible and I could track dynamics over a time of about 20 min. After that time, the structures began to break down indicating cell stress and maybe a subsequent cell death. Another thing to notice is that even though this dye is cell permeant, I

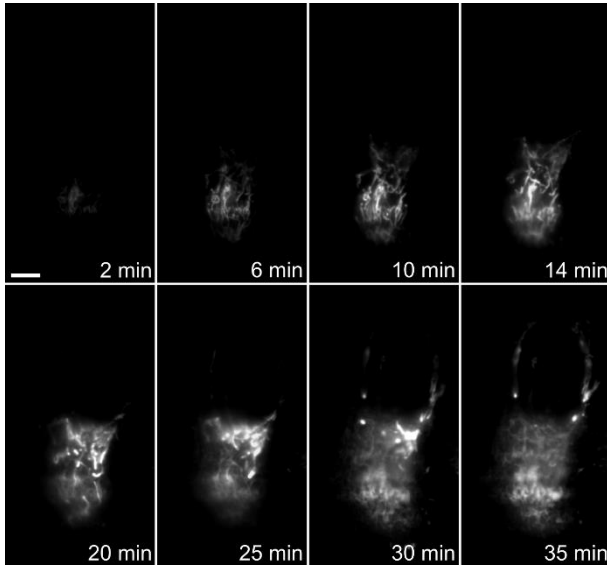


Figure 22: Nanoinjection of Mito Tracker Deep Red. We injected into the cytoplasm of a living U2OS cell. Because this dye is solved in DMSO, only a small ion current is present. This leads to a much longer staining process than normal. Only after ca. 2 min. a fluorescent signal emerges. After around 30 min., the cell is starting to die as can be seen by the mitchodrial structures breaking down. We used a concentration of 1 mM and an injection voltage of 2.5 V. Images were taken under normal wide-field conditions and an integration time of 120 ms. Scale bar, 5 μ m

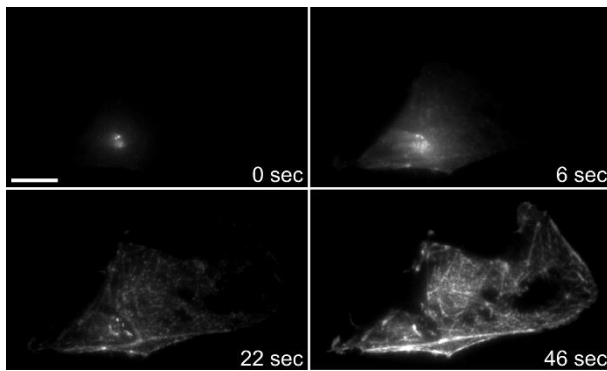


Figure 23: Nanoinjection of Atto 655 Phalloidin. Again, we injected into the cytoplasm. The images show the quick diffusion and subsequent binding of the dye molecules to the actin structure of the cell. After 45s, the staining is complete. Concentration of the dye, 10 μ M in PBS. Low wide-field conditions with 600 ms integration time. Scale bar, 5 μ m.

was able to only stain the mitochondria of one specific cell. This wouldn't be possible through a standard staining protocol.

The second staining (Figure 23) was much more straight forward, due to the highly nanoinjection-compatible dye ATTO655-Phalloidin (Atto-Tec Siegen, Germany). This fluorophore binds to the actin inside the cell, visualising the cytoskeleton. After only 45 s and applying 1.5 V, the entire actin-structure is visible.

These two injection processes show, that the MoNa system is in no regard inferior to a full-blown SICM system. On the contrary, it offers more flexibility in the choice of injected molecules. Electrode amplifiers used for scanning ion conductance microscopy are usually limited to a voltage range of ± 2 V (in my case even only ± 1 V). My op-amp and DAC on the other hand can deliver up to ± 10 V, which

means we can deliver molecules faster or can inject certain structures that aren't injectable at all at lower voltages via electrophoresis.

4.5 Conclusion

I successfully showed that it is possible to build a nanoinjection system at an 87% reduced cost with more than just the same injection capabilities and added portability. Compared to a commercial SICM system, it is flexible and can be adapted to almost any common inverted microscope (Figure 24). The only real drawback I found during my tests is the lack of an xyz piezo-driven stage. Lateral adjustments are exclusively done by hand now with the MoNa system. That means, that I am restricted to the precision of the micrometre screws, that is rarely better than 100 nm. This could pose a problem when targeting cell organelles smaller than the nucleus or when working with smaller cell types. Patience and a steady hand are the only solutions at the current state.

The setup is reduced to its essential components. Instead of an elaborate amplifier/pre-amplifier layout, I only use one small, custom-build op-amp. And instead of a rack-mounted, high-frequency and high-resolution data acquisition interface, I use a small USB device. The only thing I kept the same is the xyz-stage for pipette positioning. This concentration to the core components allows for a quick and easy setup and use of the nanoinjection setup. Now, I am able to quickly move from microscope to microscope to conduct injection experiments with relative ease due to its low weight and small form-factor.

MoNa is relatively flexible considering its components. Partially, I made use of old hardware that was already at hand. E.g. the piezo driver is more than 20 years old. A closer look at Figure 19 e shows that compared to the entire setup, this component takes up a lot of space. It could certainly be replaced by a newer, more compact piezo system. The only requirements are a minimum travel-range of 20 μm . You could go lower - but then the initial, manual positioning of the pipette tip over the sample becomes more difficult, which could result in a more frequent destruction of the sensible tip. Maybe even cheaper stepper motors could be used, as they can achieve sufficiently small step sizes below 100 nm. This only shows, that there is still potential to further minimize the system by using other components new or at hand.

I found, that with the old setup, I was sometimes restricted by the maximal electrode voltage of $\pm 1\text{ V}$. Especially larger molecules such as antibodies are harder

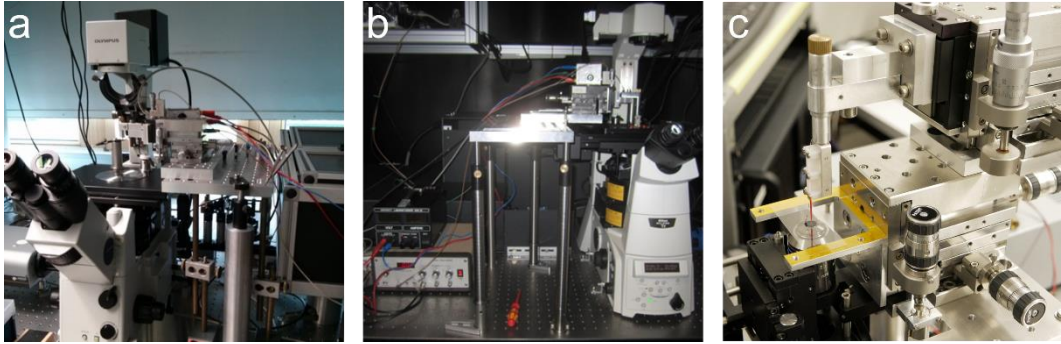


Figure 24: Examples of MoNa attached to different systems. (a) Olympus IX71 inverted microscope. (b) Nikon Eclipse TI inverted microscope. (c) Custom fast structured illumination setup running with fairSIM (Müller et al. 2016).

or impossible to inject in that range. Workarounds with external power supplies had to be used. But now, I am able to directly chose the appropriate voltage in a range of ± 10 V, which makes MoNa even more versatile.

Portability and ease of use comes with a host of new possibilities. We can now perform nanoinjection experiments on virtually any optical microscope setup using generic base-plates. For living cells this means, that they can be observed under ideal conditions i.e. appropriate temperature and atmosphere. In the last years, small and cost-efficient super-resolution systems have been reported (Holm et al. 2014). Especially for small laboratories with limited budgets, a combination of those systems could be very interesting and would open the door for new experiments.

5 Immersion Oils in Localization Microscopy

Objectives with a high numerical aperture (NA) are crucial for many advancements in microscopy. This is all the more applicable to recent super resolution techniques such as SIM, dSTORM or STED. You will find immersion objectives being used almost exclusively, due to their higher NA. However, high NA lenses are prone to optical aberrations of which spherical aberration is very prominent. This is due to the fact that it can occur even when all optical elements are strictly aligned on the optical axis.

At least three simple strategies can be used for correction: Changing the distance between the tube lens and the detector, using the objective lens' corrective collar or changing the refractive index of the immersion medium. While the first requires physical changes to the setup that are often not feasible with commercial setups, the second can effectively be applied in many situations. However, many objective lenses do not possess a correction collar or it might not be accessible for geometrical reasons. In this case, tuning the immersion medium is an easy applicable, effective and cost-efficient alternative. Apart from the optical pathway itself, changes in temperature or sample preparation lead to aberrations that can be compensated with the appropriate immersion medium.

We demonstrate how dramatic these effects can be by comparing a range of immersion oils in a variety of imaging situations. For instance, dSTORM measurements exhibit a 20% difference in terms of localization precision of the emitters when choosing an immersion oil with a refractive index only $\Delta n = 0.008$ different from the optimum. Another area greatly affected is the axial resolution both

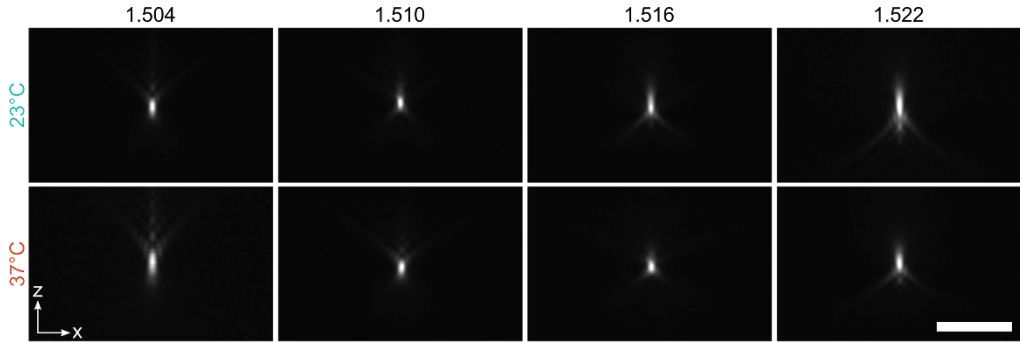


Figure 25: Axial cross-sections of PSFs acquired under different conditions. The data was generated by acquiring three-dimensional images of 100-nm fluorescent beads. Images were taken every 100 nm over a range of 10 μm . Forming of the airy ring pattern can best be seen at extremely detuned oil values like 1.504 and 1.522. As following experiments will show, the ideal oil for 37°C will be 1.516, while the ideal immersion refractive index for room temperature experiments will be 1.510. This corresponds nicely with these images as the PSFs are the most compact at these values. Scale bar, 5 μm

in conventional and super-resolution three-dimensional microscopy (Huang et al. 2008), which can be improved about 50 % as well. We also show that when working in an ideal live cell environment i.e. 37°C, again the situation changes and so should the immersion medium. This chapter shall illustrate how to easily calibrate and optimize a fluorescence microscope for conventional and three-dimensional super-resolution imaging and gives an idea of how much image quality can potentially be gained. The research was designed and conducted together with Robin Diekmann (Universität Bielefeld, 2017).

5.1 PSF Comparison

The first thing we did was to measure the system’s point spread function (PSF) in three dimensions under different experimental conditions. Because the PSF basically describes how information is transferred by the optical setup, this is an ideal starting point. To do this, we created a sparse slide of 100-nm fluorescent beads (TetraSpeck Microspheres, 0.1 μm fluorescent blue/green/orange/dark red, Molecular Probes, USA) that lie below the refraction limited resolution of our fluorescent microscope. We chose a red (647 nm) laser line as illumination as it is often used by us and is especially gentle to living cells concerning phototoxicity (Wäldchen et al. 2015). Furthermore, deep red dyes are often preferred for dSTORM. It is important to have a sparse distribution of beads on the cover glass because we are imaging an

axial range of 10 μm . The Airy patterns can get quite large when the focus is several micrometres away from the emitter, so it should be checked beforehand if these patterns overlap neighbouring microspheres.

Our fluorescence microscope setup is equipped with a piezo-driven objective ring (PI.WS P-721.10, Physik Instrumente, Germany) and corresponding custom control software. We took an image every 100 nm for a total range of 10 μm . This provides adequate information of the entire intensity distribution along the PSF. We repeated this process with a variety of different immersion oils with their respective refractive indices (1.500 to 1.526) under 23 °C room temperature and 37 °C common cell culture conditions. Temperature control was achieved with help of a custom heating stage. Additionally, we prepared one batch of bead slides with thinner #1 (150 μm) cover-slides (instead of the otherwise used #1.5, 170 μm) to see whether this makes a difference as well. It should be noted that our objective lens (APON 60XOTIRF, Olympus, Japan) has an adjustment ring to compensate for both of these circumstances. However, we wanted to emulate the possibility of not having this option. Looking at an excerpt of the measured PSFs (Figure 25), huge differences in PSF geometry become apparent at the two different temperature settings when using the same oils. Nevertheless, we couldn't find any significant difference concerning the differently sized cover glasses.

Before looking further into the details and continue evaluating our data, we wanted to know what to expect from our results first. Because a meticulously chosen oil is crucial for structured illumination microscopy (Demmerle et al. 2017) and much time is spend finding the right one, GE Healthcare Life Sciences (USA), as manufacturer of commercial SIM systems, provides a web tool (GE Healthcare 2017) for choosing the right oil. This tool takes the glass slide thickness, objective, temperature, sample refractive index and excitation wavelength into account. Unfortunately, the underlying algorithm is not disclosed. If we enter all our values (170 μm , 1.49 60x objective, 23 °C, 1.33, 650 nm), we are presented with an optimal oil of $n=1.518$. This is also the standard oil previously recommended for our objective by the manufacturer (Olympus). A temperature increased to 37 °C should in turn be compensated by an oil index of 1.524. Note that these values refer to commercially available setups.

Now we determine the FWHM both axially and laterally of the measured PSFs through Gaussian fits. A data set of simulated PSFs (using the Gibson and Lanni model (Gibson und Lanni 1992)) showed an approximately quadratic behaviour of the axial FWHM dependent on the refractive index. On the other hand, it should

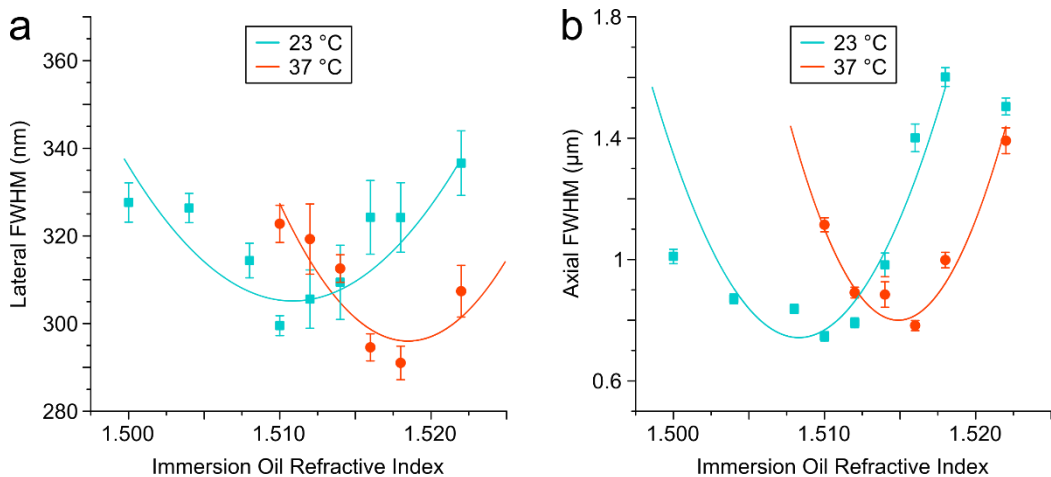


Figure 26: FWHM of the PSFs dependent on the immersion oil. The FWHM was determined by a gaussian fit through the focus of the beads. (a) For their lateral measurements, all values are only spread roughly 8% around 320 nm. The quadratic fits (solid lines) merely serve to indicate a possible trend. (b) The best resolutions for the axial data are determined by quadratic functions and give 1.5083 ± 0.0029 for 23 °C and 1.5146 ± 0.0025 for 37 °C.

have no influence on the lateral FWHM at all when measuring directly in focus. If we take a look at the axially measured results (Figure 26 b), the FWHMs show approximately the predicted behaviour. A quadratic fit, while not as good as in the simulated data, still seems reasonable and yields an optimal oil refractive index of 1.5083 ± 0.0029 and 1.5146 ± 0.0025 for 23 °C and 37 °C respectively for our setup. This is off by 0.01 of our expected manufacturer values (1.518 and 1.524). Although these slight changes do not seem that significant, if we take the determined 23 °C FWHM from the 1.510 oil (747 ± 15 nm) and compare it to the width achieved by the proposed 1.518 oil (1601 ± 31 nm), there is a more than 2-fold increase visible. Nevertheless, the relative difference between the two temperatures (~ 0.006) is consistent with the proposed values.

The lateral data (Figure 26 a) is made up of a much narrower distribution of different widths. Although our simulation predicted that there should be no difference at all, the same trend as in the axial data is recognisable. It becomes clear that our simulated PSFs are not suited for a meaningful comparison in this way. If we look again at the axial cross-sections (Figure 25), the issue becomes clear. For de-tuned oils, the focal region of the PSF becomes visibly elongated (by a factor of two and more as mentioned before). Though our simulations show that the lateral geometry in the focus point does not change at all, this does not take into account the overall

signal distribution. If we assume that the same number of photons are emitted regardless of the particular shape of the PSF, less photons will be available in each lateral focus position if the shape is broadened along the optical axis. Less signal in turn means a poorer signal-to-noise ratio and ultimately a wider FWHM even in the xy-plane. Another factor that has to be considered is the process of focusing itself. Spherical aberrations lead to defocus and the longer the central shape of the PSF becomes, the harder it is to find the exact focus point. Especially for single molecule localisation microscopy this is an issue, because here it is crucial for the maximum signal (and therefore resolution) to pinpoint the ideal focus.

5.2 2D dSTORM PSF Statistics

In order to get a meaningful statistic over as many emitters as possible, in a second step we prepared a standard dSTORM sample and imaged it with five oils ranging from $n=1.508$ to $n=1.524$. Each single emitter event results in a two-dimensional PSF that is localised and fitted by the STORM reconstruction algorithm (ThunderSTORM plugin (Ovesný et al. 2014) in ImageJ (Schindelin et al. 2015)). Afterwards, all determined localisations with their respective sigma values ($\sigma = \text{FWHM} / 2\sqrt{2\ln 2}$) are stored and statistically analysed. These measurements were performed on a slightly different optical setup. While the model of the objective and microscope body remained the same, slight differences in the illumination and detection pathways were present, leading to different optimal values regarding the immersion oil's refractive index.

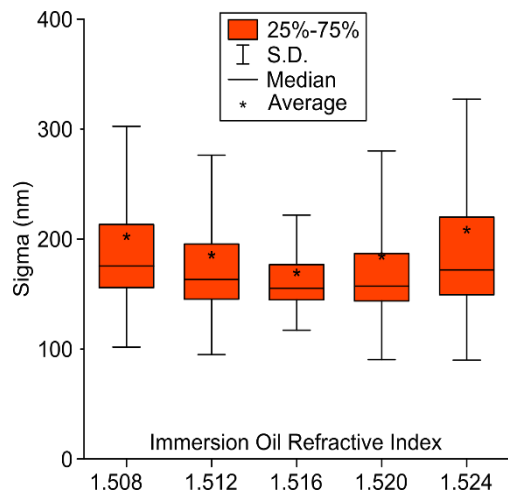


Figure 27: Statistics of localisations and their respective sigmas. We acquired 3 times 7,500 frames of immunolabelled microtubules under the same conditions for each oil. Mean values are, from left to right, 202 nm, 186 nm, 169 nm, 185 nm and 209 nm. ThunderSTORM was used for localization and emitter fitting. 647 nm laser power 4 kW/cm^2 , integration time, 14.9 ms.

U2OS cells were fixed and their microtubules immunolabelled with Alexa 647. For a complete sample preparation protocol, please see Appendix A.7. We adjusted and optimised the illumination power and TIRF/HILO angle for imaging with the 1.516 oil, as experience proved this to be the best one suited for this particular setup. For subsequent measurements, illumination conditions were kept the same. Intermittent, low-power UV radiation (378 nm) was sporadically used to provide an improved blinking density.

We see again a symmetrical distribution around a centred value (Figure 27). This confirms the impression we got from the previous experiment, this time with greater statistical relevance. Now, 1.516 is the optimal refractive index of the immersion oil. If we compare the corresponding lowest mean sigma to its neighbouring values (1.512 and 1.520 oils with 186 and 185 nm), we already have a difference of 10%. Going to the outside points with 202 and 209 nm, this difference becomes even larger (20% and 24%). The wider standard deviations caused by the unoptimized oils further implicate that the elongated focal shapes of the PSFs are leading to a more undefined signal, that is much harder to focus upon.

5.3 Correction for Refractive Index Mismatch

In following experiments, we want to use our now oil-wise optimised setup for the acquisition of three-dimensional images. One more thing that has to be taken into account is the apparent elongation along the optical axis, caused by the refractive index mismatch between the immersion oil ($n=1.5$) and the sample medium (assumed to be water, $n=1.33$). To compensate for this, we used a calibration sample consisting of three differently sized fluorescent microspheres. The smallest TetraSpeck beads (100 nm) have a diameter below the diffraction limit of the system. With them we registered the cover glass surface

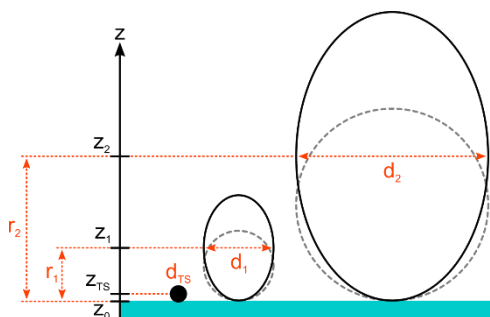


Figure 28: Schematic side-view image of the 3D calibration sample. The apparent form of the beads seems elongated (solid black ellipses) and differs from their actual form (dashed grey circles). TetraSpeck beads (black dot) are used to register the cover glass surface. Determining the beads' diameters and apparent height, one can calculate the refractive index mismatch.

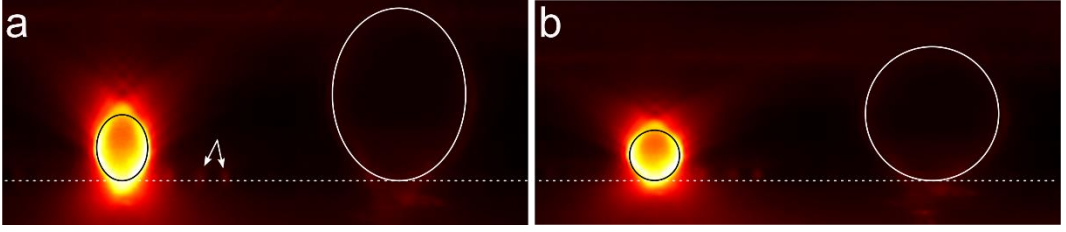


Figure 29: Side-view of three sizes of fluorescent beads. Arrows show two small TetraSpeck beads, black circles indicate the $2.8\ \mu\text{m}$ bead and the white circles the large $8\ \mu\text{m}$ beads. Note, that due to labelling differences, the large sphere is barely visible in this depiction. The $100\ \text{nm}$ beads are used to register the cover glass surface (dashed line). (a) The elongation of the supposed circles is clearly visible. We determined the average width/height ratio to be 0.77 . (b) With this factor, it is possible to correct the image which now shows the actual geometry much better.

to get a solid reference point for subsequent measurements. The other two types of spheres with diameters of approx. $2.8\ \mu\text{m}$ and $8\ \mu\text{m}$ were used to check the mismatch at two different depths inside the sample (see Appendix A.8 for preparation protocol).

For a calibration measurement, a region of interest containing all three kinds of beads is selected and a z -scan performed. Slices should be no further apart than approx. $50\ \text{nm}$ to ensure an adequate calibration. Figure 28 shows a schematic side-view. To get the coordinate of the cover glass surface z_0 , the small TetraSpeck beads are used:

$$z_0 = z_{TS} - \frac{d_{TS}}{2} \quad (5.1)$$

where z_{TS} is the z -position of the bead and d_{TS} its diameter. The diameters of the large beads d_1 and d_2 can be measured and with their apparent radii r_1 and r_2 . The mismatch ratio M can be calculated as follows:

$$M_i = \frac{r_i}{d_i} = \frac{z_i - z_0}{d_i} = \frac{z_i - z_{TS} - \frac{d_{TS}}{2}}{d_i} \quad (5.2)$$

To have enough leeway, we have imaged a large volume of our calibration sample with a thickness of $18\ \mu\text{m}$ and a step size of just below $48.9\ \text{nm}$ (Figure 28). The glass surface was calculated by axially fitting the TetraSpeck signal. Through a small custom written MATLAB program determining the radii of the larger beads each z -

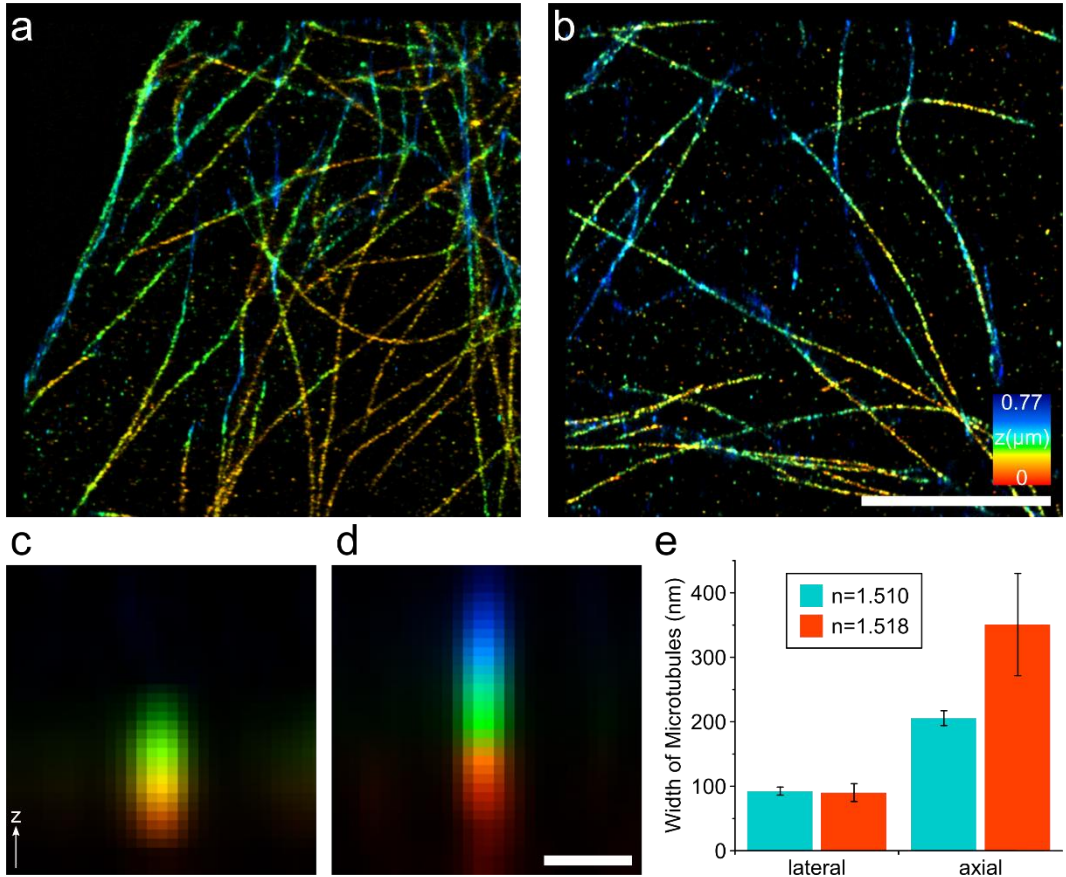


Figure 30: Comparison of 3D STORM images using different immersion oils. As sample, we used fixed U2OS cells with immunolabelled microtubules. Color-coded projections of the reconstructed images using (a) $n=1.510$ oil and (b) standard 1.518 oil. Scale bar, $5\ \mu\text{m}$. (c,d) Representative cross sections through a microtubule. While the data acquired using the un-optimized oil generates an axially distorted image, the proper oil leads to a more circular geometry. Scale bar, $1\ \mu\text{m}$. (e) Statistical analysis over the width and height (FWHM) of 10 microtubules each for the different oils. The lateral data gives $92.5 \pm 6.2\ \text{nm}$ and $90 \pm 14\ \text{nm}$. While the axial analysis shows more difference with $205 \pm 12\ \text{nm}$ and $351 \pm 79\ \text{nm}$.

slice, we were able to obtain the exact geometry. The diameter of the larger bead is in the range of what to expect ($8.195 \pm 0.022\ \mu\text{m}$), while the supposed $2.8\ \mu\text{m}$ sphere falls a bit short with only $2.115 \pm 0.013\ \mu\text{m}$. But that does not matter, since this approach only depends on the spherical shape of the beads and not their absolute dimensions. Finally, we calculated the mismatch to be 0.78 ± 0.01 for the smaller and 0.76 ± 0.03 for the larger bead. We will correct all following three-dimensional images with a factor of 0.77.

5.4 3D dSTORM imaging

As a final test for the relevance of choosing the appropriate oil for super-resolution fluorescence microscopy, we are imaging the same immunolabeled fixed U2OS cells as before. This time we are using an additional cylindrical lens ($f=1000$ mm) approx. 5 cm in front of the camera to introduce astigmatism into our detection pathway. This way 3D STORM images can be acquired. As oils, we are using the “standard” 1.518 oil and the 1.510 oil that yielded the best results in our first experiment.

Since the position of the localised emitters is encoded directly into the geometry of the PSF, it seems reasonable that the wrong oil should again have a bad influence on both lateral and axial resolution of the final image. What we see (Figure 30) are two, at the first glance similar images if we look at the lateral projection of the reconstructed data. Only if we examine the three-dimensional appearance of individual microtubules, can we see the difference. Using an unsuitable oil leads to a cross section that is drastically stretched along the optical axis. On the other hand, the optimal oil yields a much more natural looking tube while still not being perfectly round as expected. Looking at a small statistic of the width and height of 10 sections of microtubules for both conditions, the visual impression can be confirmed. The lateral dimensions are virtually the same, whereas the axial data shows a 70% increase in size from 205 nm to 351 nm. Additionally, the deviation of the axial 1.518 data is much larger with ± 79 nm compared to only ± 12 nm of the 1.510 oil. Both these values indicate that an unsuited oil leads to more unpredictable, worse results. – at least axially.

5.5 Conclusion

There are three conclusions to be drawn from the presented data. One, do not trust the manufactures suggestions or web tools to determine the right immersion oil for your setup. We found, that our two setups both needed a different oil to achieve their maximum potential (1.510 and 1.516 instead of 1.518). Two, temperature has the predicted effects on the imaging capabilities and needs to be compensated with

the appropriate oil. And three, otherwise, with unsuitable oil (off by $\Delta n = 0.008$), especially the axial resolution suffers greatly and is around two times worse. On the other hand, lateral precision seems to be less effected with PSFs 10% to 20% broader, while the reconstructed 3D STORM image showed no difference at all.

We showed two methods to determine the best oil. Either through three-dimensional images of the PSF or through a statistical analysis of common STORM data. While the first method is applicable for all microscope setups and can potentially even be done by hand without the help of a piezo-driven stage or objective, the second method surely is more stochastically sound and accurate. Both methods however, show that the optimal oil is strongly dependent on the individual optical pathway. Both setups used the same objective and microscope body and still yielded not only oil indices different from the standard, but from each other as well.

It should be noted though, that the mismatch calibration and the choice of oil is also strongly dependent on the used wavelength. We used probes fluorescing in the deep red spectral range throughout the experiments as an example but for different excitation wavelength, these measurements have to be repeated. This is also true for other temperatures or changes in the detection path. As mentioned, some objectives have adjustment rings to compensate different temperature ranges. Of course, these can also be used instead of changing oils. But as these objectives are not always available for everybody, adapting the oil is a cheap and flexible alternative.

6 Nanoinjection PAINT

With nanoinjection it is possible to inject dye molecules directly into living cells and at the same time imaging the process. This leads to a number of new possibilities when combining this with super-resolution methods such as dSTORM or PAINT. In this chapter, I show as a proof of concept that it is possible to acquire super-resolved images of living cells in two and three dimensions through simultaneous injection and imaging.

6.1 Real-time Control of Labelling Density

One of the many challenges of modern super-resolution techniques is the sample preparation. Especially the labelling density is a factor of utmost importance and many papers have been published concerning this issue (Sinkó et al. 2014; Kaplan und Ewers 2015; Chamma et al. 2016). While it is relevant for basically every fluorescence imaging process, I will concentrate in the following only on its implications to single molecule localisation methods such as dSTORM, PAINT or SOFI.

In SMLM methods if the density of fluorophores in the on-state is too high, the subsequent reconstruction algorithm oftentimes fails to distinguish between overlapping emitters and either discards the signal or gives a false localisation. Although multi-emitter fitting algorithms are able to compensate this to a certain extent, they are computationally more demanding and lack the resolution of a good single emitter fitting (Holden et al. 2011). Methods like SOFI can be used for a dense,

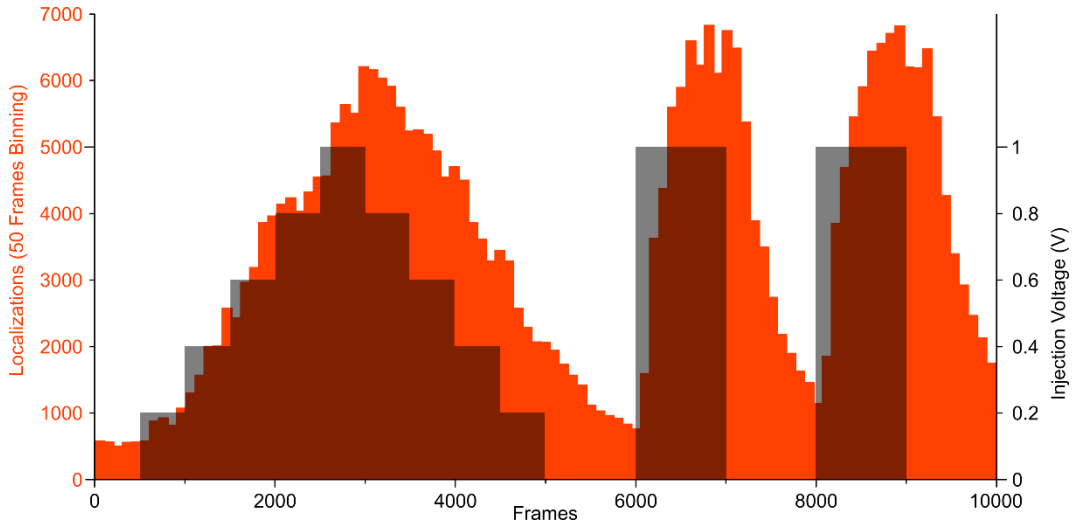


Figure 31: Single molecule localizations per 50 frames and corresponding injection voltages.

We injected Atto 655 Phalloidin into a living U2OS cell and recorded a total of 10,000 frames at 80 ms exposure time, while adjusting the voltage between 0 and 1 V. The corresponding reconstructed image can be seen in Figure 31. Although the localization frequency lags a few seconds behind, it is highly controllable by changing the voltage. It takes about 500 frames (40 s) for the localization count to plateau around 6000, after applying the full 1 V starting from zero. And after cutting the voltage, it goes back down again to its starting value of ca. 500 in about 1000 to 1500 frames (80 – 120 s).

fluctuating distribution of emitters, but it gives only a resolution enhancement of the factor of $\sqrt{2}$ (Dertinger et al. 2012).

On the other hand, a distribution of fluorophores that is too sparse, inevitably leads to longer imaging times as more frames have to be acquired in order to register enough localisations for a complete, super-resolved image. Or even worse, the density falls short of the Nyquist criterion and an accurate reconstruction is theoretically impossible.

Another problem, especially with the high illumination powers needed for dSTORM, is photobleaching. This means that the labelling density and thus the localizations per frame decrease with advancing imaging time as more and more fluorophores are irreversibly destroyed. Photoswitchable dyes can be used up to a certain point to adjust the behaviour of some fluorophores to compensate for this effect by switching more of them to the on-state. But at some point, there simply are not enough functioning molecules left for an efficient imaging process. Moreover, the irradiation used for photoswitching can introduce additional problems and cause increased mortality of cells through phototoxicity.

PAINT circumvents some of these issues. There is a virtually infinite supply of fresh fluorophores that can replace old, bleached ones from the surrounding solution constantly. But there are some restrictions to this method as well. The dye molecules must be highly cell permeant to yield a high enough concentration of fresh fluorophores inside of the cell. Of course, this doesn't apply for membrane stains, that only attach on the cell surface. Alternatively, fixed and permeabilized cells can be used to image structures within the cell.

The method I employ is a variation of PAINT combined with nanoinjection. I insert the nanopipette into the cell and ensure a continuous flow of fluorophores through the pipette into the cytosol. This way, bleached dye molecules can be replaced with fresh ones. And in contrast to PAINT, I am not limited to cell permeant dyes or membrane stains or fixed cells, as I inject directly into the cytoplasm or nucleus, circumventing the membrane. Another advantage is that through adjustment of the voltage, the density of fluorophores can be altered directly and in real-time. This way, the optimal dye distribution can be set for different imaging circumstances.

As a test of the possible flexibility concerning labelling density I injected a U2OS cell with ATTO655-phalloidin as described in previous chapters. During injection, I altered the injection voltage and recorded the corresponding number of localizations per time unit. The result can be seen in Figure 31.

I am able to adjust the density on the fly during a 10,000 frames image acquisition. Response time from 0 to 1 V and from 1 to 0 V are around 500 frames (40s) and 1500 (120s) frames respectively. After these times, the localization frequency plateaus at around 6000 per 50 frames and drops again to its starting value

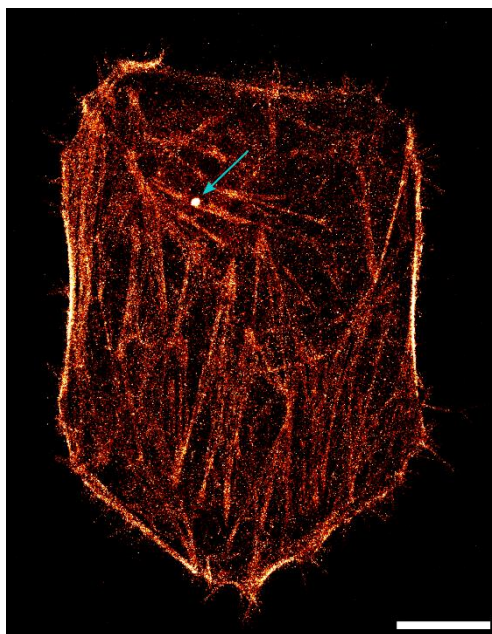


Figure 32: Reconstructed SMLM image of the actin structure of a U2OS cell. We injected a $3\mu\text{M}$ solution of Atto 655 Phalloidin in PBS into the cytoplasm using different voltages. (Figure 30). The blue arrow indicates where the pipette tip was located during image acquisition. Using a red laser intensity of 30 mW and an integration time of 80 ms, 10,000 frames were recorded for this reconstruction. Scale bar, 10 μm .

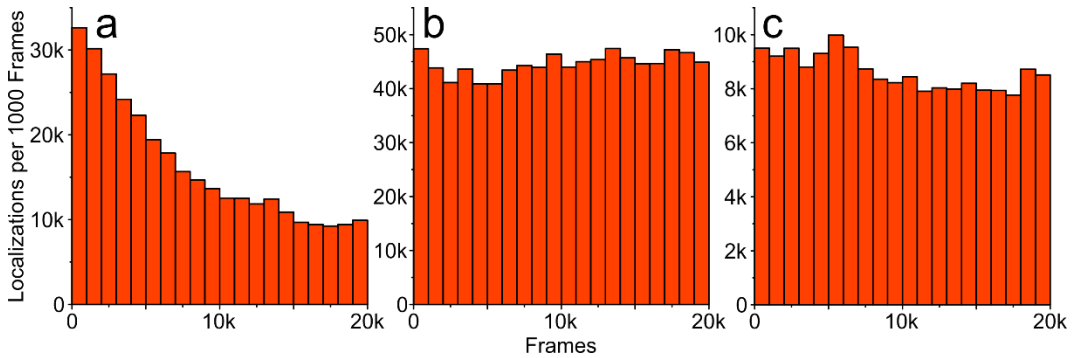


Figure 33: Time dependency of localization frequency. For each experiment, we recorded 20,000 frames. (a) Standard *d*STORM acquisition using anti- β -tubulin primary antibodies and Alexa 647 conjugated secondary antibodies (the complete staining protocol can be seen in Appendix A.7). The localization frequency declines approximately exponential due to photobleaching. Exposure time per frame, 25 ms. Illumination intensity 40 mW. (b) DNA PAINT data obtained with the commercial ultivue kit. The active emitter density remains the same throughout the whole imaging process. Exposure time 100 ms at an intensity of 30 mW. (c) Nanoinjection PAINT. The nanopipette was placed inside the cytoplasm while imaging. ATTO 655 Phalloidin was injected with a voltage of 30 mV. The data yields the same result as the classic PAINT approach – the localization frequency remains roughly on one level. Integration time was 80 ms with a laser power of 30 mW.

of around 500. This might seem rather slow, but considering that single molecule localization methods usually demand relatively long total acquisition times (tens of minutes), this isn't an issue. Additionally, I only need small voltage adjustments to fine tune the emitter density compared to the tested quick changes from 0 to 1 V and vice versa. To prove that I am not just measuring free fluorophores inside the cell but rather bound dyes contributing to a meaningful image, I performed a reconstruction of the 10,000 frames afterwards (Figure 32). There are indeed some emitters randomly distributed inside the cell, but the majority adds up to the image of the cell's actin structure. Because the density wasn't adjusted to give the best possible image but rather as a prove of adjustability, not enough localisations have been acquired and thus, the image looks spotty as expected.

To further prove that this method indeed works in the same manner as PAINT and is able to yield a constant localisation frequency, I compared it to data acquired with a commercial DNA-PAINT kit (Ultivue Training Kit, ultivue, UK) and a standard *d*STORM image (Figure 33). The *d*STORM sample was prepared in the same fashion as described in the previous chapter: A primary antibody/secondary antibody labelling method was used to stain the microtubules of fixed U2OS cells.

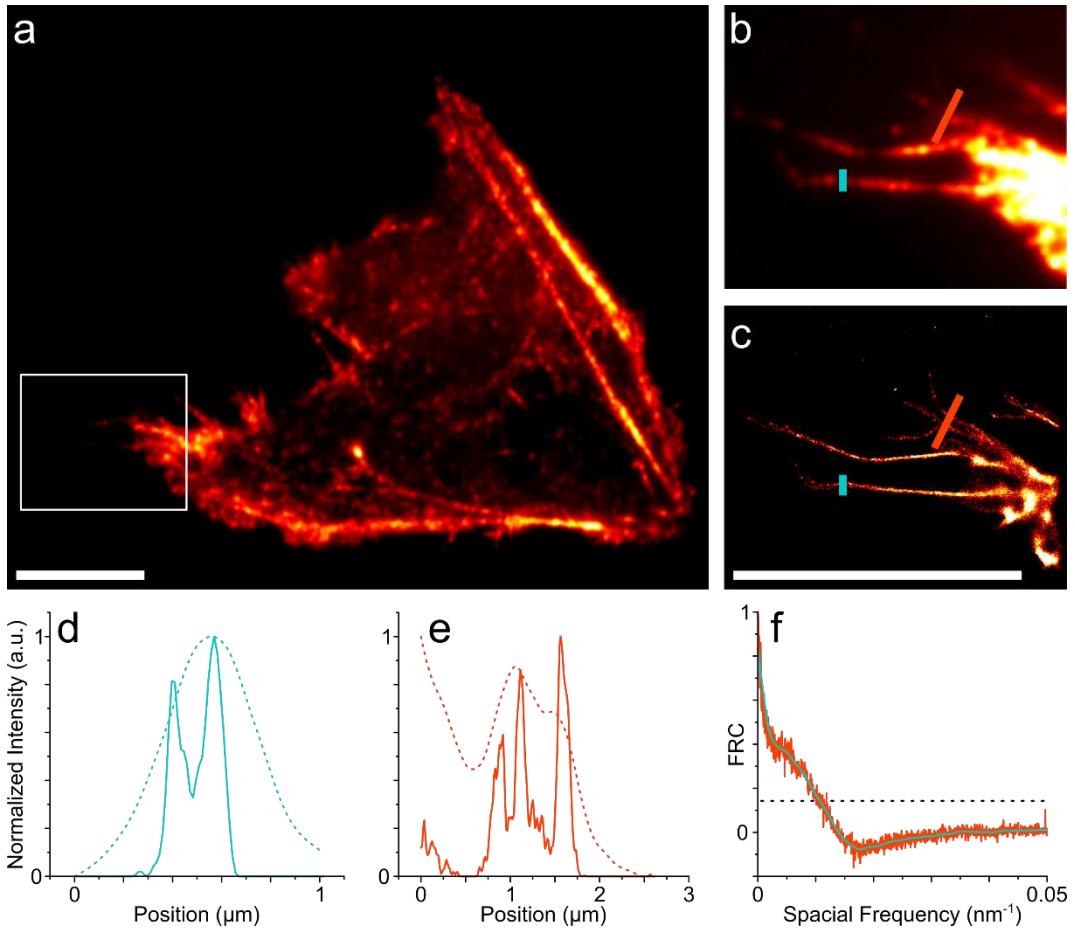


Figure 34: Widefield and super-resolved images of labelled actin. The U2OS cell was penetrated by a nanopipette filled with $3\mu\text{M}$ ATTO 655 Phalloidin in PBS. An injection voltage of 40 mV was sufficient for continuous acquisition. 20,000 frames were recorded with an exposure time of 80 ms and a laser intensity of ca. 40 mW. (a) Widefield image of the entire cell. (b) Detail of the widefield image. (c) Super-resolution reconstruction of the image detail. The actin filaments are displayed much sharper and additional details can be seen. Both scale bars, 10 μm . (d,e) Line plots of the areas indicated in b and c. Dashed lines correspond to widefield data, solid lines to the super-resolved image. There are multiple peaks clearly visible through the reconstruction that otherwise would have been undistinguishable. (f) Fourier ring correlation of the reconstructed image. The dashed line represents the 1/7 mark, below which any values are considered noise. The resolution is determined to be 93.3 ± 16.5 nm.

The basis of the PAINT kit is the same primary antibody. However, the provided secondary antibody is conjugated to a small DNA fragment. During image

acquisition, a complementary fluorophore-labelled DNA strand solution is added. Binding and unbinding of the two strands cause the typical PAINt signal to emerge.

As expected, we see that the dSTORM signal suffers a roughly exponential decay due to photobleaching. On the other hand, the classic DNA PAINt and my new nanoinjection PAINt method show little to no change in localisation frequency. Remaining fluctuations in signal strength are likely due to issues with shifting focus or stochastic variations rather than declining numbers of available fluorophores.

6.2 PAINt Imaging of the Cytoskeleton

Now that I have shown, that I can acquire images in a PAINt-like fashion using the nanopipette as a constant means of dye molecule delivery, I further test the capabilities of this method. Because we saw that the actin-stain was already working, I tried to acquire a super-resolved image of the cytoskeleton of a living cell. Again, I used ATTO 655 Phalloidin for this purpose.

Like in the previous example, I had to use a fairly high exposure time of 80 ms. Compared to STORM experiments this value is around ten-fold higher than what is usually worked with. But for PAINt circumstances, this is quite normal. Because the dyes diffuse through the cell, bind and unbind, bleach and get replaced, these long exposures are necessary. This way, the signal of moving molecules gets smeared along some distance and is easily discarded, while bound molecules concentrate their emission on the same spot. Once the pipette is positioned inside of the cell and the voltage is adjusted to yield a reasonable emitter density, image acquisition is started. I found, that a voltage of around 40 to 60 mV (and a corresponding current of approx. 0.5 nA) are sufficient for a continuous localization frequency when using a dye concentration of 0.6 mM.

As we can see in Figure 34, I am able to generate a super-resolved image that yields much details than the original widefield image. Small actin filaments are visible that previously weren't distinguishable from each other. To confirm the subjective gain in resolution, I performed Fourier ring correlation on the raw data set. A value of only 93.3 ± 16.5 nm falls a bit short of what I hoped for. STORM images usually achieve resolutions of 10 to 40 nm. One reason behind this could be the relatively long acquisition time of approx. 27 minutes (20,000 frames times 80 ms) and the fact, that at least in the beginning of the injection the cell was still alive. This additional movement and sample drift that couldn't be compensated completely may be

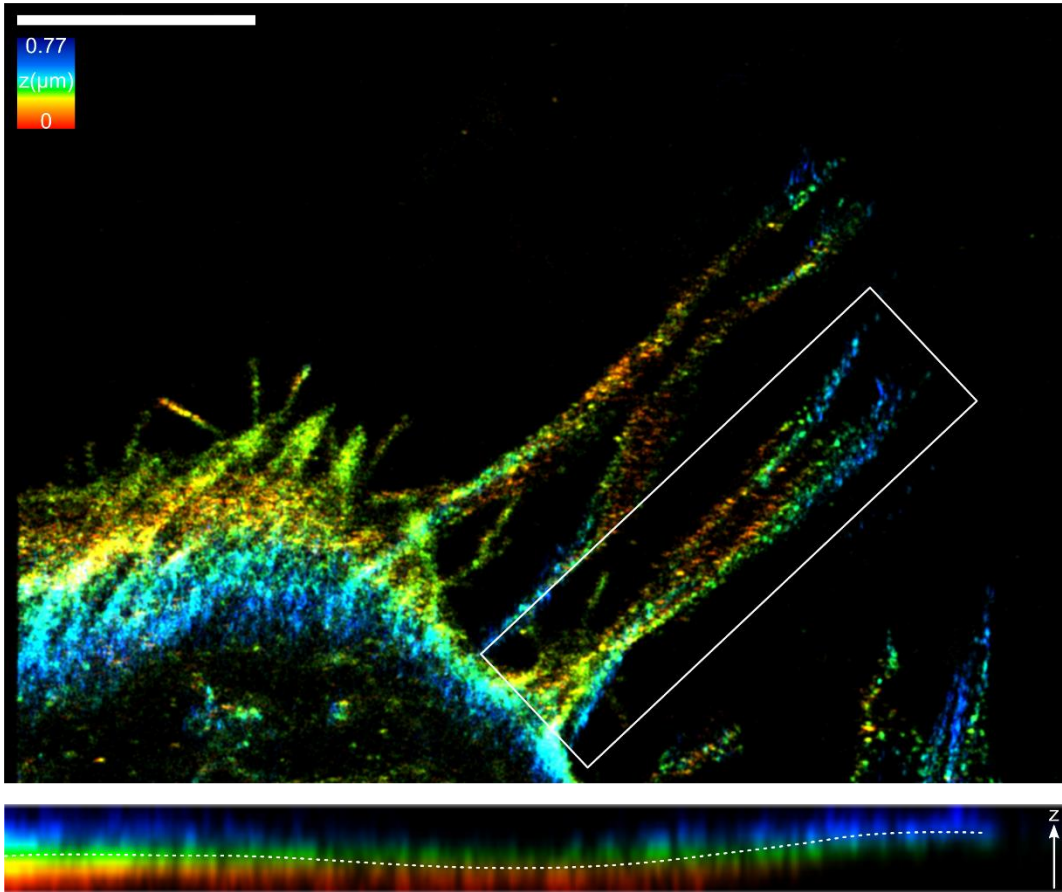


Figure 35: 3D reconstruction image of actin filaments of a living U2OS cell. Top: lateral projection of the 1 μm thick imaging sheet, color coded according to height above glass surface. Scale bar, 5 μm . Bottom: Side view of the indicated filaments. The dashed line indicates the average height of the filament.

responsible for the not optimal resolution. Nevertheless, a resolution enhancement by a factor of 3 compared to the theoretical Rayleigh limit of 278 nm for red light could be realized.

6.3 3D PAINT imaging

After the careful characterisation and calibration of our fluorescence microscope setup in respect to its 3D capabilities (see chapter 5), I now want to try out my nanoinjection PAINT approach to generate super-resolved, three-dimensional images

of live cells. The procedure is basically the same as with the already shown normal, two-dimensional image acquisition. You only have to consider that out-of-focus emitters are also contributing to the reconstructed image. Because their PSF is much broader than at their respective focal location, the density has to be lower to allow for precise detection of their dimensions. Also, the TIRF/HILO illumination has to be adjusted, so that roughly a $1\mu\text{m}$ thick slice of the sample is evenly illuminated. Keeping this in mind, I once again stained the actin structure of our U2OS cells.

The results are shown in Figures 35 & 36. I can resolve the three-dimensional morphology of outreaching actin filaments. They start at a height of around 500nm above the cover glass and over the course of several micrometres, they first bend down with the lower part attached to the glass surface. Finally, they seem to curve up again, sticking out freely into the medium.

6.4 Discussion & Conclusion

I demonstrated that it is possible to acquire data on par with that of a commercially available DNA PAINT kit. I was able to confirm the adjustability of labelling density and to obtain super-resolved images in two and three dimensions with a spatial resolution as low as 93nm .

Furthermore, I imaged live cells – compared to the PAINT kit and most STORM protocols that call for fixed, permeabilised cells. The first minutes of continued injection, the cell can be still assumed living. But at some time, the toxic phalloidin has immobilised the cells actin structure and we are no longer observing a fully

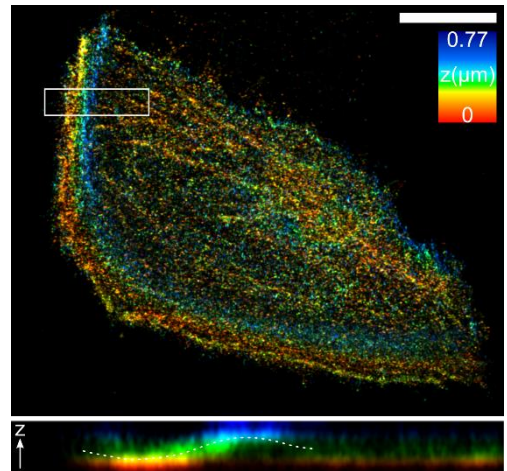


Figure 36: 3D reconstruction of an entire living U2OS cell. Top: lateral projection of the $1\mu\text{m}$ thick imaging sheet, color coded according to the distance from the cover glass. Scale bar, $10\mu\text{m}$. Bottom: Side view of the marked area above. The dashed line indicates the average height of the localized emitters.

functioning cell. However, there was still enough movement throughout the cell that the long imaging process leads to a lower resolution than what I hoped for.

With additional injections with YOYO-1 iodide, this problem was even more pronounced. YOYO binds to the double-stranded DNA of the cell's nucleus and does not have the fixation properties of phalloidin. Thus, the cell moves during the entire imaging process and the acquired data was virtually unusable for the reconstruction of a super-resolved image.

A proposed solution was to use a cooling stage to inhibit cell movement to a minimum by cooling them below room temperature. This proved to be feasible and was even shown to have negligibly effects on the cells health (Velve Casquillas et al. 2011). However, commercially available stages were either not compatible with nanoinjection because they prevented the necessary continuous access to the sample, or they introduced vibrations through moving parts which in return decreased localisation precision again. A custom build heating/cooling stage (see chapter 8) ultimately proved unsuitable too because of issues in combination with our piezo-driven microscope stage.

Another idea to circumvent sample movement issues is to reduce imaging time to a minimum. However, PAINT works only with long exposure times of around 100 ms. A step into the realm of STORM could be the answer (Hennig et al. 2015a). If a cell is labelled completely by nanoinjection subsequently imaged with a high frequency and intensity, the fluorophores would blink and bleach rapidly analogous to Figure 33 a. Illumination could then be shut off and with a high voltage, new fluorophores could be introduced fast through the still present nanopipette. Repeated cycles of this procedure would lead to a saw-tooth-like distribution of localisation frequency and could possibly yield an over-all speed-up. However higher voltages and illumination powers could lead to an even faster cell death.

Nevertheless, this technique could pose an interesting addition to the established PAINT method, as it is now possible to use different fluorophores previously not taken into consideration. Even for STORM measurements this could potentially lead to a better imaging result, as the labelling density can be precisely monitored during injection. After that, the pipette can be retracted and a common STORM image can be acquired.

7 Nanoinjection of the Alga

Chlamydomonas Reinhardtii

C. Reinhardtii is a unicellular green alga that is widely used in biology as a model organism. It is well studied and easy to culture. The possibility and necessity to genetically modify these organisms, e.g. as a means of biofuel production, has huge implications (Scranton et al. 2015). However, even with modern methods like CRISPR/Cas9, it has proven to be very difficult to achieve this goal (Shin et al. 2016).

In this chapter, I show that electrophoretic nanoinjection of the 10 μm small cells is possible and could potentially be used as an alternative to the standard delivery method of electroporation.

This research has been realized with the help of the “Algae Biotechnology & Bioenergy” research group (Universität Bielefeld, 2017).

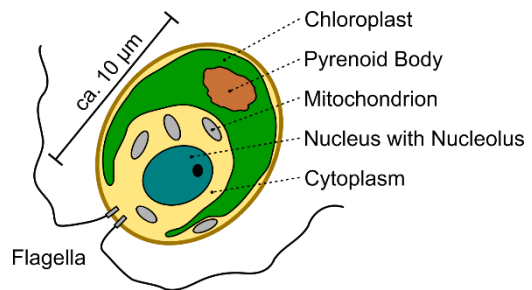


Figure 37: Schematic illustration of a single alga. The chloroplast is cup-shaped and surrounds almost the entire middle of the cell. Like plant cells, these algae have an outer cell wall.

7.1 History & Motivation

The clustered regularly interspaced short palindromic repeats (CRISPR) /CRISPR associated protein 9 (Cas9) system has generated a lot of attention and popularity due to its high specificity and versatility in gene knockout and editing (Doudna und Charpentier 2014; Kim und Kim 2014). This ribonucleoprotein complex (RNP) originated from a part of the bacterial immune system that destroys invading viral DNA and plasmids by specifically targeting and cleaving them with the help of a small piece of guide RNA (gRNA). While a first study reported the successful implementation of CRISPR/Cas9 on *C. Reinhardtii* via electroporation, it showed a low targeting efficiency hinting to the possible toxicity induced by the protein complex or the plasmid used for its expression (Jiang et al. 2014).

Schierenbeck et al. (2015) introduced a highly light tolerant phenotype of *C. Reinhardtii* by whole-gene-sequencing. These types are especially interesting for industry-scaled outdoor cultivation and commercial use. Nevertheless, additional studies must be conducted on these strains to gain further insights into their biology. A crucial tool for this purpose is the knockout of certain genes to observe its impact on the organism. CRISPR/Cas9 could present the appropriate means to achieve this goal, however the delivery method of electroporation proves to be a limiting factor. Because millions of algae are treated at the same time and the delivery happens in a stochastic manner, with so far only low efficiency, only genes expressing a unique phenotype can be targeted efficiently. Otherwise, targeted clones cannot be distinguished from non-targeted ones.

Our proposed solution is to directly nanoinject the RNPs into the algae to restrict false clones to a minimum so that further experiments can be done with higher certainty.

7.2 Injection Procedure and Cell Preparation

A recent publication (Zhou et al. 2017) already showed for the first time that it is possible, to electrophoretically inject fluorophores into the algae without killing them. The method they proposed is similar to the process of artificial insemination albeit on a smaller scale (Figure 38). They use an injection pipette with an inner diameter of approx. 200nm and an outer diameter of approx. 300nm, which is

roughly twice the size of our nanopipettes. A second pipette with a diameter marginally smaller than the algae itself is used to capture a single cell and hold it for the injection with a small amount of suction. Viability has proven to be in the order of 10 minutes while applying a constant voltage of 1 V. As my injections only need to last seconds, I presume that an increased mortality induced by the injection itself will only play a minor role.

In contrast to the reported method, our nanoinjection setup has the pipette positioned along the optical axis of the (in our case inverted) microscope and I do not have the option of an additional pipette holding the algae in place. But as the algae can be cultivated on agarose gel (see Appendix A.7 for full cell preparation protocols), I used this to immobilize the living cells for nanoinjection (Figure 39). A drop of agar (1% v/w with tris-acetate-phosphate (TAP) cell medium) is deposited onto a cover slide and left to dry for a moment. Then a second drop of medium containing the algae is placed on the fringe of the agar droplet making sure that there is a good contact area between them. As the medium dries out slowly, most of the cells accumulate at the edge of the drop. Because the medium contains a fraction of agar through the original cell preparation and it solving parts of the agar droplet, it leaves a very thin conductive layer behind that encloses and fixes the algae in place when it dries out completely.

The pellet of the counter electrode can be stuck into the agar drop. Now, the approach curve will look inverted compared to its usual form, because the surrounding medium is non-conductive air. This means that during the approach no current is detected up until the pipette tip contacts the fixated algae cells. After this, the injection works as usual. The voltage can be adjusted to yield the best results concerning the used injection medium.

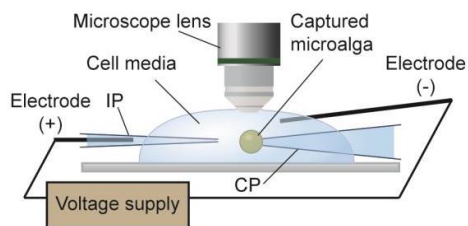


Figure 38: Schematic illustration of the injection setup previously taken from Zhou et al. The larger capture electrode (CP) holds the algae in place with a small vacuum, while the smaller injection pipette (IP) is used for the actual injection.

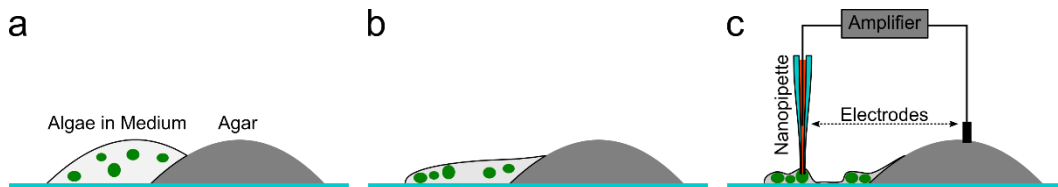


Figure 39: Schematic illustration of sample preparation and nanoinjection. (a) When the drop of medium containing the algae is initially deposited, the algae are dispersed evenly within the drop and are moving freely. (b) While the water slowly evaporates, the algae begin to concentrate at the edge of the drop. (c) The medium contains a fraction of agar as well, which in the end encloses and immobilizes the cells. Nanoinjection then functions “dryly”, with the ion current only emerging, when the pipette comes in contact with the algae. The previously placed agar droplet is used as a contact for the counter electrode.

7.3 Fluorophore Injection

As a proof-of-principle, I first tried to inject a fluorophore known to be compatible with nanoinjection. The auto-fluorescent properties of the algae have to be considered to yield an optimal signal that can clearly be associated with the injected dye. Usually, these cells show a stronger intrinsic fluorescence compared to mostly transparent mammalian cell lines. My choice fell upon Dextran Alexa 488. This dye is of the same making as the dextran used in my survival experiments, except for having a blue shifted spectrum that can be better distinguished from the fluorescent background of the algae.

Other than the already described fact that the approach curve has an inverted shape, injection works as expected with an injection voltage of -100 mV, although the pipette has to be positioned laterally with greater care. Not only are the algae quite small to begin with (approx. 10 μm diameter) but the cup-shaped chloroplast within the cell must be avoided (Figure 37). Injection into this large organelle would cause the target molecules to get stuck inside it with no chance of reaching the cytoplasm and nucleus. This basically leaves a target of half the diameter of the original cell. However, I am able to perform injections directly into the middle of the alga. This is a promising result for the next steps (Figure 40).

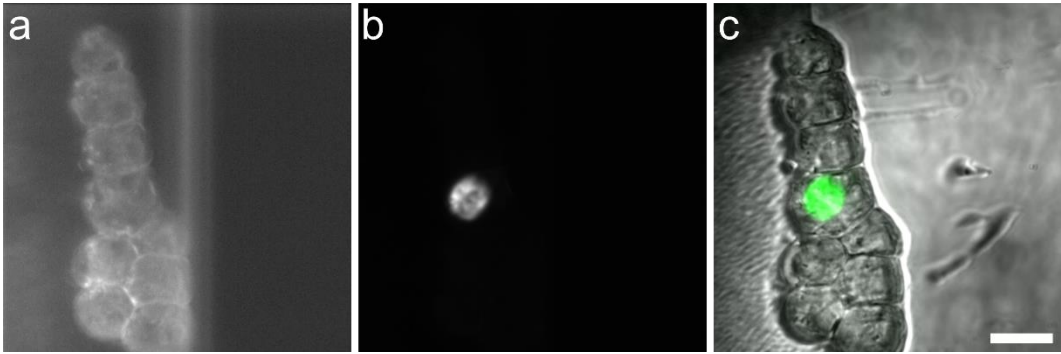


Figure 40: Injection of one alga with Dextran Alexa Fluor 488. Injection voltage was -100 mV and the time needed to stain the cell only 1-2s with a dye concentration of $666\text{ }\mu\text{M}$. (a) Green fluorescence channel before the injection. All that can be seen is auto-fluorescent signal. (b) After the injection, a bright and spatially distinct region can be seen. (c) An overlay with a whitelight image shows that the signal is contained within the cytoplasm of the cell indicating that the surrounding chloroplast has been avoided. Scale bar, $10\text{ }\mu\text{m}$.

7.4 Injection of RNPs

The fundamental working principle of nanoinjection is at the same time its biggest drawback. In contrast to pressure-driven microinjection, the molecules are only ejected out the pipette through electrophoretic forces. Parameters such as the orientation and intensity of the electric field, molecule concentration, weight and charge have to be considered. If the molecule of choice shows a fluorescent signal, injection can be easily verified optically. But if it is not fluorescent and there are no further details of the molecule available, trial and error is the only option.

For the first test, I used a CRISPR/Cas9 protein complex that knocks out the phytoene synthase gene of the algae. This prevents the cell from producing carotenoids that are essential for photosynthesis and photoprotection. The effected algae will become pale (called “white mutants”) and are not able to survive in the light (McCarthy et al. 2004). Using this highly visible phenotype I can assess if and to what extend the delivery of RNPs by nanoinjection is successful.

I injected approx. 20 cells out of a population of approximately 100 cells per culture dish. For a first experiment, this should be sufficient to find the white mutant clones even after several generations. Injection was performed with three different relatively low concentrations of the protein complex (4 nM , 20 pM and 0.2 pM) as one

molecule is theoretically all it needs to modify the genome. The protein is positively charged and thus, a positive voltage applied to the pipette will supposedly inject this molecule into the cell.

After injections took place, the culture dishes are filled with TAP medium to resuspend the algae. It is important to keep them in a dark environment from here on as the white mutants will only survive without light. Two days thereafter, the suspended algae are transferred to TAP/agar (1.5% w/v) petri dishes for two to three weeks and checked for white algae colonies.

7.5 Conclusion

Unfortunately, the end results could not be determined prior to finishing the writing process of the work at hand. Nevertheless, nanoinjection of fluorescent molecules into *C. Reinhardtii* itself represents an (almost) novel approach of working with these algae and a promising first result.

Next steps would be to further refine the process. For example, a 100% injection rate of algae within the culture dish has to be achieved in order to make confident assumptions of the efficiency. This could either be realised by further diluting the algae or by speeding up the injection. I also have to be certain (at least to a reasonable extent) that all performed injections are successful at injecting the RNPs. Ideally, I could confirm this through phytoene synthase knockout. But since the efficiency of the knockout itself is not yet entirely clear, further experiments are obviously needed.

To further establish the method of nanoinjecting *C. Reinhardtii* in general, a survival statistic in the same fashion as described earlier in this work would be necessary. The mentioned 2017 paper only investigated the momentary viability of single cells. While this surely gives an indication of the initial reaction of the algae, a longer study would yield a certain result.

8 Heating & Cooling Microscope Stage

For working with living cells on a microscope, it is important to keep cell stress to a minimum if one wants to observe them behaving mostly undisturbed. This can be done by using low illumination powers and suitable mediums. But one key factor is temperature. By keeping cells in their natural temperature range (37 °C for U2OS and most mammalian cell lines) at least this issue is resolved.

As mentioned before in Chapter 6, it can be beneficial for certain imaging methods that demand longer acquisition times to inhibit cell movement to a certain degree (Velve Casquillas et al. 2011). This could be achieved by a microscope stage capable of cooling the cells below room temperature. Processes inside the cell will slow down and for a certain amount of time, the disadvantages of the induced cold shock will outweigh the improved imaging conditions.

In this chapter I summarize the problems concerning temperature controlling stages used in single molecule localisation microscopy and show a possible solution by building an automated, Peltier-controlled heating and cooling stage.

Previous Temperature Controlled Stages

The equipment previously used in our lab to keep living cell samples at a suitable 37 °C consists of a hollow copper ring that could be fitted to the objective. This ring is connected via two tubes to a temperature controlled water reservoir, continuously pumping the water through the ring. It is even possible to cool the water and thus the objective and overlying sample. The precision is also more than adequate with 0.1 °C. But there are two problems. Only the objective is connected with the temperature control, so there is a considerable thermal gradient between it, the sample and the microscope stage. This leads to unwanted convections inside the

sample and temperature stress within the setup which causes sample drift. The second problem is more an issue with single molecule localisation microscopy. Vibrations introduced by the flowing water cause a worse localisation precision. Disabling the water circulation during imaging prevents vibrations but the change in temperature again induces sample drift, ruining long time acquisitions.

Another heating stage I used was of a much simpler design. A couple of resistors attached to the metal sample stage and powered by an adjustable power supply. The heat is closer to the sample and therefore the temperature equilibrium is more stable. Nevertheless, the temperature has to be calibrated over a long time and is only indirectly controllable via the power supply. It lacks flexibility as a change in room temperature can only be compensated manually and vaguely. Also, this concept does not provide any cooling functionality.

8.1 Peltier Controlled Microscope Stage

The new approach utilizes Peltier-elements to solve those problems. There are no moving parts like circulating water and in contrast to a resistor-based design both heating and cooling can be achieved by reversing the voltage. Additionally, I implement a PID-control via temperature sensors on the stage and in the sample controlled by an Arduino microcontroller (Arduino UNO, Arduino, Italy).

Hardware

I chose copper as the main building material of the stage plate since it has the second highest thermal conductivity of all metals. Hereby the heat can spread efficiently throughout the entire system and thermal gradients will be smaller. Furthermore, we wanted to combine the designs of the previous devices by connecting the stage with the objective via two heavy copper cables (Figure 41 a,b). Now, temperature gradients through the sample itself, which lies between these parts, ought to be much smaller, too.

To balance the heat capacity of the copper stage and connected objective ring, a solid piece of copper roughly the same weight is connected to the other side of the two Peltier-elements. Finally, aluminium heat sinks are attached to the copper block to dissipate the heat quick and effectively. An additional small fan can be used to further increase heat transfer. In that case however, the fan has to be mounted in

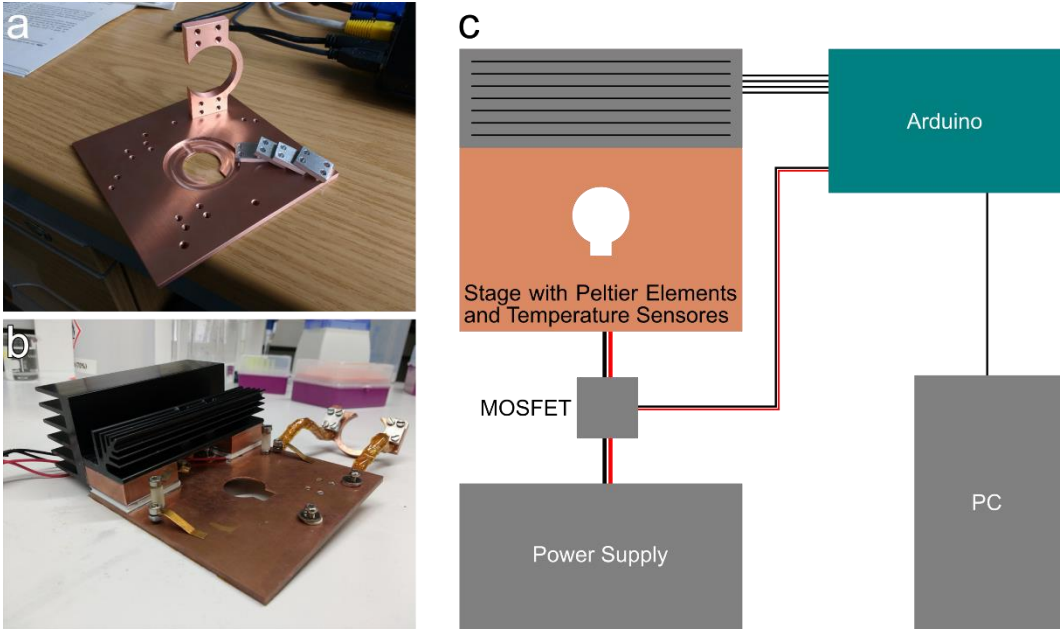


Figure 41: Images and illustration of the heating & cooling stage. (a) shows the main copper stage with a recessed hole for the objective, the objective ring and four aluminum plates used to create a tight connection between the solid parts and the cables connecting the ring and plate. (b) The Peltier elements (white, between the copper layers) are securely fixed between the stage and copper core of the heatsink with special heat-conducting glue (resin-based with aluminum particles). The cables are now seen connecting the underside of the plate with the objective ring. (c) shows the system integrated in our fluorescence microscope. Note the additional fan on the right of the heatsink providing extra heat dissipation. (c) Schematic image of the entire system. The Arduino microcontroller is controlled and communicates via USB with a PC running a MATLAB program. It collects data from the four temperature sensors and sends a PWM signal to relay the power from a supply to the Peltier-elements.

such a way that neither vibrations are directly transferred into the system nor the airflow is directed over the sample itself.

Electronics and Control

I am using two Peltier elements (TES1-127030-30X30, P&N Technology, China) with a sustainable temperature difference of 75 °C at 16.4V and 3A. A standard laboratory power supply is used as source. It is set to a maximum of 20V and 3A suitable for the serially connected elements. To control the amount of power reaching the Peltier elements, the output is pulse-width modulated (PWM) through a MOSFET (IRF 520N). The amount of PWM can be set from 0-255 by an Arduino microcontroller board. To get sufficient temperature feedback from the system, a

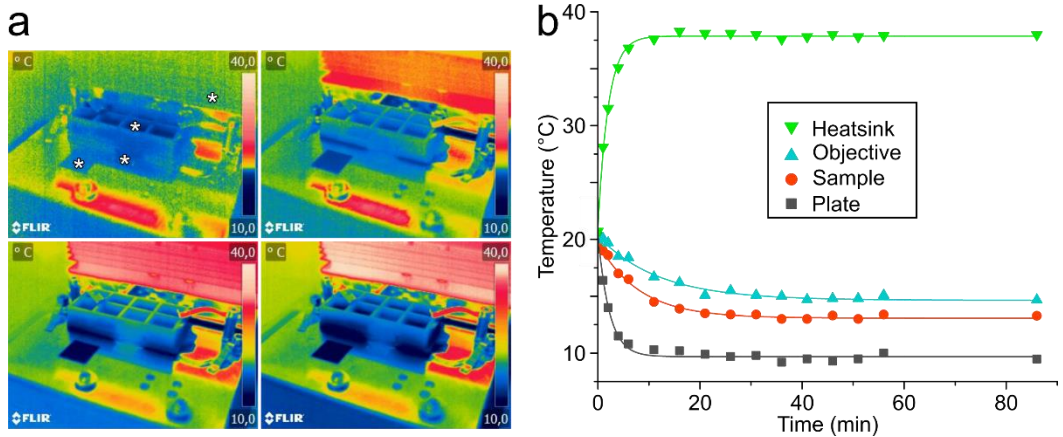


Figure 42: IR temperature measurements. The system runs without any PID control with 2 A, 6 V supplied to the Peltier elements. (a) Thermographs show the temperature distribution over the course of about 1.5 hours. The white stars indicate the points of measurements. To get an accurate reading of the reflective copper and objective body, a piece of matt black tape was added. The inside of the LabTek container is filled with water. (b) Temperature points over the course of time and an exponential decay fitted to the data. The end temperatures reached are $37.865 \pm 0.091^\circ\text{C}$ for the heatsink, $14.65 \pm 0.15^\circ\text{C}$ for the objective, $13.077 \pm 0.090^\circ\text{C}$ for the sample and $9.69 \pm 0.14^\circ\text{C}$ for the stage plate itself.

total of four digital temperature sensors (DS18S20, Maxim Integrated, USA) are used. They deliver with an accuracy of 0.1°C the readings from the heatsink, stage and ambient room. An additional, water-proof sensor can be placed directly in the sample. They too are controlled through the Arduino (Figure 41 c).

While PID-control and temperature settings could be done directly on the microcontroller, I decided to use the serial interface to connect it to a small MATLAB program. In the software, all relevant preferences like the desired temperature, maximum heatsink temperature and PID-parameters can be set. Simultaneously, all temperatures are displayed over the course of one minute as well as the current PWM percentage.

8.2 Cooling Experiments

To verify the cooling capabilities of my stage, I did a series of measurements with a thermographic camera (Figure 42). These first experiments are yet done without the PID-control. I just applied a power of 12 W (2 A, 6 V) to the Peltier elements and waited for the system to reach its thermal equilibrium. In doing so, I

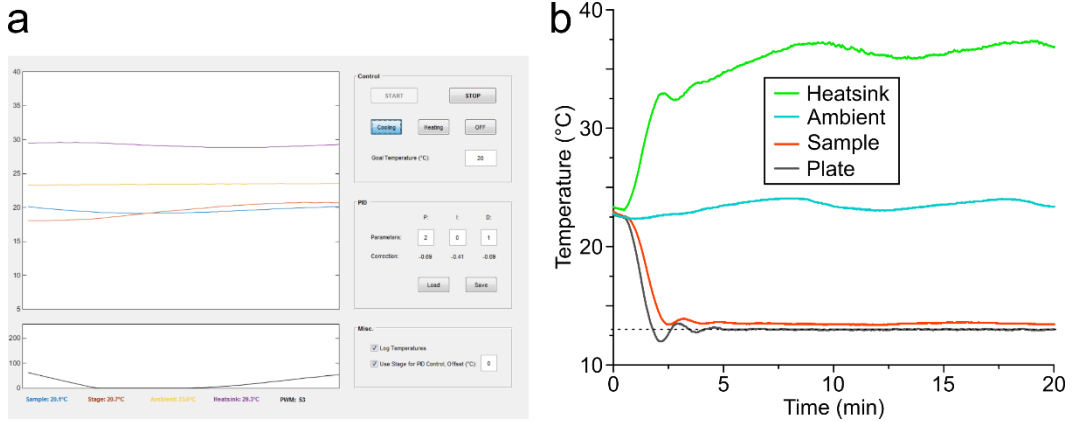


Figure 43: Cooling with the temperature stage. (a) shows the GUI of the MATLAB program. The temperature is displayed over the course of one minute on the top left. Right below that, the PWM can be seen. The right side is used for general control like goal temperature, PID parameter adjustment and switching between heating and cooling. (b) Temperature data of the cooling process. A goal temperature of 13°C for the stage was set ($\sim 10^\circ\text{C}$ below room temperature, dashed line). While the room (and therefore heatsink) temperature fluctuate, the stage remains stable within a 0.4-degree range after only 5 minutes. The sample itself was only 0.5°C warmer.

know for future experiments when it is save to start measurements with minimal sample drift caused by changing temperature gradients. I found that after 40 minutes the temperature does not change significantly anymore. As expected, heatsink and base plate are the quickest to reach their end temperatures (38°C and 10°C), since they are directly in contact with the thermo-elements. The sample temperature stayed 3° above the stage temperature. This is caused by the geometry of the chamber-slide used here. The measured chamber was positioned right over the objective hole. It was isolated by the plastic walls from the surrounding, colder wells. A larger sample dish used in following measurements yielded better contact and heat transfer with the stage plate.

Now I tested the capabilities of the entire system with active temperature control enabled. For this, I set a temperature goal of 13°C which was 10 degrees below room temperature at the starting time (Figure 43). After only 5 min, the sample temperature is stable within $13 \pm 0.2^\circ\text{C}$. The sample itself has a 0.5 degrees higher end temperature which is reached after another minute. Even though the ambient room temperature fluctuates between 22 and 24°C during the 20-min measuring interval (possibly caused by the air condition), this has no influence on the stage and sample temperature. Compared to the uncontrolled resistor-based temperature stage that is a huge advantage as it provides stable imaging conditions throughout the

experiments. The PWM of the power supply levelled off at around just under 63%. A further test with the PWM set to an average maximum of 95% yielded a temperature difference of 15 °C between the stage and room. The 5% headroom for the power proved to be sufficient for the active PID-control to work as expected.

8.3 Conclusion

I showed that it is possible to build a simple temperature controlled microscope stage out of only a few parts. A temperature gradient of 10 degree can be reached in only 5 minutes. Although for the heatsink and the surrounding setup to be in an adequate thermal equilibrium, 40 minutes should lie between setting the temperature and imaging. The maximum gradient of my setup below room temperature was determined to 15 °C. After that, the heatsink is not able anymore to sufficiently cool the hot side of the Peltier-elements anymore and the temperature will increase with a growing rate.

Due to the Peltier-element's poor efficiency of only around 10%, cooling is much harder than heating the stage. The limiting factor here proved to be the ability to dissipate the generated heat efficiently. Heating works much easier with much less power consumed. Temperatures of 50 °C only demanded 15% of the total available power.

Although the capabilities of my stage were satisfactory in respect to the temperature control, it proved to have compatibility issues with the piezo-stage of our fluorescence microscopy setup. The combined weight of the solid copper and relatively big aluminium heatsinks introduced huge irregular drift issues. Unfortunately, this issue could not be resolved in time.

9 Conclusions and Outlook

92% Survival Rate in Nanoinjected Cells

It was important for future experiments to reliably determine the survival rates of nanoinjected cells. Otherwise, the big advantage compared to ensemble methods such as electroporation becomes meaningless. A high viability of treated cells is crucial for single cell methods. I was pleased to have found an exceptionally high 92% long-term survival rate. The comparison with a microinjection probe with a five-fold increased inner diameter of 500 nm yielded further insight to what extent volume displacement correlates with cell viability. In addition to that, I took the influence of the electric field and duration of injection into account, further enhancing this comprehensive statistical analysis. While I refrained from using stress markers to distinguish living but stressed cells from completely healthy cells, I could observe a normal proliferation behaviour in the majority of nanoinjected cells indicating a relatively undisturbed cell cycle.

Cost-Efficient Mobile Nanoinjection

I was able to show that it is possible even with limited resources to build a fully functional nanoinjection setup. 87% of the costs were saved by reducing the system to its core components. However, I proved that the injection capabilities are still on a par with previously used equipment that originated from scanning ion conductance microscopy. In addition to that, we can now adapt MoNa to a variety of experimental conditions since the new system is flexible and lightweight.

Excursus: Choosing the Wrong Immersion Oil Impairs Image Resolution

On my way to combine nanoinjection with super-resolved SMLM, we exposed an oftentimes overlooked way to improve the imaging qualities of a fluorescence microscope. The choice of immersion oil had an immense impact on the resolution of a reconstructed super-resolution image. We could show that the lateral effect is not as severe ranging from 20% worse image resolution in standard dSTORM to no detectable difference in 3D STORM. The axial resolution however was proven to be 150% to over 200% worse.

Super-Resolved PAINT Imaging via Nanoinjection

In contrast to all other SMLM methods, I demonstrated that via nanoinjection, it is not only possible to maintain a constant level of labelling density but that it is also highly adjustable through the applied voltage. This can be used to provide optimal imaging circumstances over long periods of time, as a virtually unlimited supply of fresh fluorophores can be delivered.

I showed, that through a combination of PAINT and nanoinjection, I am able to acquire three-dimensional super-resolved images of living U2OS cells with an actin label that is not inherently suitable for standard PAINT.

Nanoinjection of Non-Adherent Algae

So far only as a proof-of-concept, I could show the nanoinjection of fluorescent molecules into living algae cells. For this I developed a protocol that allows reproducible injection into the non-adherent *C. Reinhardtii* and is easier to accomplish than the previous reported method using two pipettes at the same time. Further experiments with the introduction of RNPs into the algae have been conducted but remain inconclusive until now.

Comprehensive Outlook

The field of single cell specific research has been growing rapidly over the last decades (Figure 44). Many new methods have been developed due to the increasing demand for new ways to manipulate and study biological processes on a (sub-)cellular level (Yuan et al. 2017). Up until recent developments, the vast majority of publications concerning cellular processes or the behaviour of cells under specific

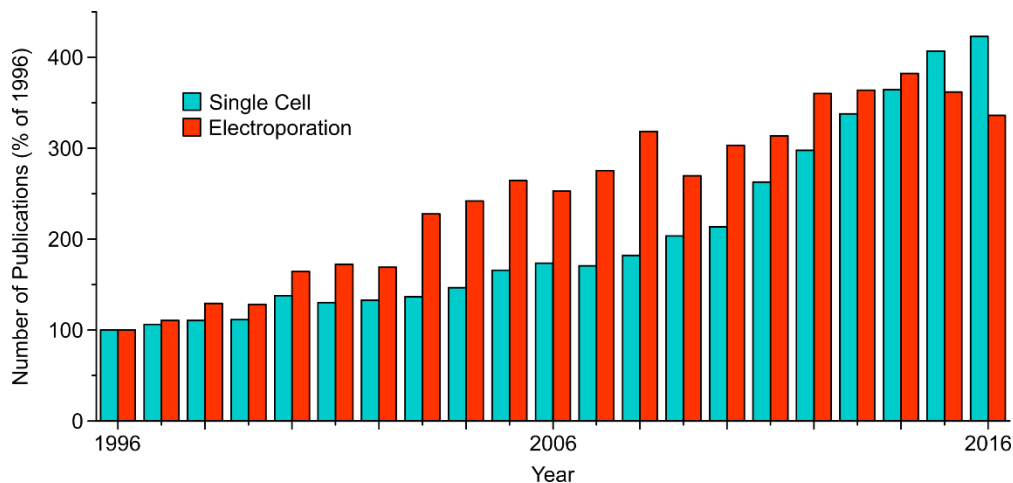


Figure 44: Number of publications during the last two decades. The data is taken from the PubMed database (National Center for Biotechnology Information (NCBI) 2017). The search term “single cell” yielded an almost exponential growth starting from 594 in 1996 to an over 400% increased 2512 in 2016. For comparison, the second search term “electroporation” represents a standard cell ensemble method. It started with 191 publications in 1996. No strong trend is observable and as of 2014, the relative growth of this method falls behind. End point here is 642 or roughly 340%.

experimental conditions relied on cell culture. That is, the generated results illustrate the average reaction of the average cell out of millions without the chance of making definitive statements concerning the reaction of specific single cells. But small variations within the cell population may lead to completely different outcomes. Hence the need for new single cell methods (Perkel 2017).

This fact is also supported (or even made possible in the first place) by the current developments in fluorescent imaging. Super-resolution techniques make it possible to image processes within single cell with increasing quality, speed and versatility. Further development and combination of single cell imaging and manipulation methods will without a doubt create new tools and possibilities to gain an ever-increasing insight in the fundamental mechanics of cell biology.

One of these new tools is presented with electrophoretic nanoinjection. It was first reported a decade ago but it has only been in the last few years that its advantages are understood and used for specific tasks. These advantages become clear by taking a look at the work at hand. This method hits a sweet spot concerning complexity, cost, versatility and cell viability (Figure 45). Compared to microinjection it yields an improved viability and the possibility to inject into smaller targets. In contrast to AFM based methods once again the survival rate is superior. Additionally, the injection process is much more straight forward and with MoNa, a

cheaper and more flexible approach exists. Carbon nanotube-based injection techniques are especially gentle to the cells due to their extreme small size. Nevertheless, probe preparation and the choice of injection target are quite restricted.

Of course, nanoinjection has its drawbacks as well and further work has to be done in order to advance and established this approach. Maybe the biggest disadvantage in comparison to microinjection and other pressure-driven methods are the so far insufficiently explained particle kinetics inside the nanopipette. While predictions based on electrophoresis alone hold in roughly 80% to 90% of all cases, there are simply too many variables or even unknowns in this sensitive system. Sometimes injection of certain molecules seems to be impossible - maybe due to the earlier described equilibrium of electro-osmotic and electrophoretic forces. A solution to this would be to use larger nanopipettes instead, as electro-osmosis contributes more to the molecule movement as the diameter of the capillary gets smaller. Although this would in turn lower the viability of treated cells. But as more applications emerge and more experiments are going to be done, nanoinjection will be further refined and more useful for the increasingly important single cell specific research field.

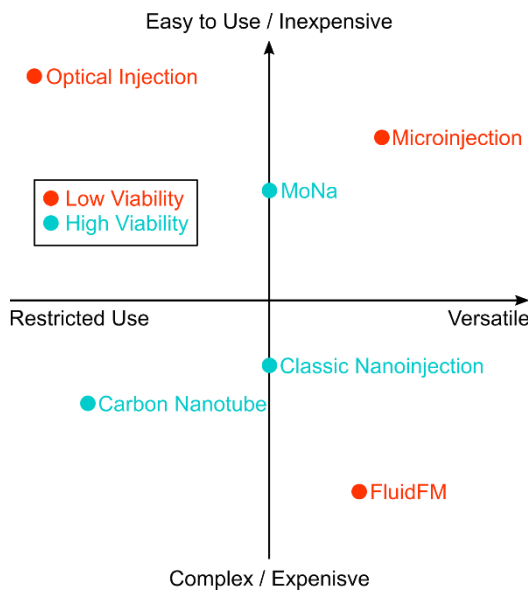


Figure 45: Illustration of single cell delivery method attributes. The costs are merely estimated values. But it seems reasonable that with increased complexity, they also will be higher. Versatility refers to the ability to inject a certain variety of different molecules into different target cells.

A Appendix

A.1 Raw Data of the Survival Statistics

Table 2: Summary of the viability experiments. Experiment Parameters from left to right: Used pipette inner tip diameter, duration of injection, applied voltage, target of injection, injected fluorophore. N, number of total injected cells per experiment. Dead/Alive status is checked 24 hours after injection.

Experiment Parameters	N	Dead	Alive
100 nm, 1 minute, 0.5 V, nucleus, no fluorophore	18	0	18
	14	1	13
100 nm, 5 minutes, 0.5V, nucleus, no fluorophore	8	1	7
	9	2	7
100 nm, 1 minute, 1 V, nucleus, no fluorophore	11	0	11
	12	2	10
	12	0	12
100 nm, 5 minutes, 0.5 V, nucleus, no fluorophore	5	2	3
	9	6	3
	6	3	3
	6	3	3
100 nm, 1 - 10 seconds, 1 V, cytoplasm, DAF	14	1	13
	15	3	12
	18	2	16
	21	3	18
100 nm, 1 - 10 seconds, 1 V, nucleus, DAF	10	2	8
	24	5	19
	17	2	15
	20	5	15
500 nm, 1 - 10 seconds, 1 V, cytoplasm, DAF	11	7	4
	14	7	7
	11	9	2
	14	8	6
500 nm, 1 - 10 seconds, 1 V, nucleus, DAF	18	11	7
	18	14	4
	14	8	6

A.2 Nanoinjection Materials & Methods

Setup

The setup is based around the fluorescence microscope described in Appendix A.5. For manual positioning of the nanopipette, a xyz-stage (M-562 XYZ ULTRAlign, Newport Corporate, USA) is connected to the custom-made pipette holder. Further fine adjustment and approach to the cell surface is done by a xyz piezo-driven microscope stage (MCL Nano-PDQ375HS, Mad City Labs, USA). The ion current is measured by a patch-clamp amplifier (Axopatch200B, Axon Instruments, Molecular Devices, USA) and compatible pre-amplifier (CV203BU, Axon Instruments). Data (voltage) I/O is regulated by the PCIe-card of the fluorescence microscope setup and an additional USB device (USB6001, National Instruments). A custom-written software (LabView, NI) is used to control all important parameters (e.g. electrode voltage, approach speed, etc.) and displays and regulates the approach of the nanopipette to the cells.

Electrodes

For the electrodes that were placed inside the pipette, a 5-cm piece of teflon-coated silver wire was cut from a coil (Science Products, Germany, AG-8T) and the tip chlorinated inside of sodium hypochlorite (NaClO) for approx. 30 min. The not chlorinated end then is stripped bare for a few mm to make contact with the electrode amplifier. Pelleted counter-electrodes for the electrolyte bath are also purchased from Science Products (Ag/AgCl Pellets, E-205).

Micropipettes

I used Femtotips (Eppendorf, Germany, E5242952008) with an inner diameter of 0.5 μm and outer diameter of 1 μm for comparison with our nanopipettes.

Nanopipettes

Borosilicate glass capillaries (GB100F-8P, Science Products GmbH) with a length of 7 cm, an outer diameter of 1 mm and an inner diameter of 0.58 mm are pulled into two nanopipettes using the following program of the P2000 puller (Sutter Instruments, CA, USA):

Line1: HEAT:350, FIL:3, VEL:30, DEL:220, PULL:0

Line2: HEAT:330, FIL:2, VEL:27, DEL:180, PULL:250

This gives us a within reasonable (approx. 5%) deviations, an inner diameter of 100 nm and an outer diameter of 150 nm.

Filling of the Nano- and Micropipettes

To ensure a predictable, reproducible injection behaviour, it is important to fill the pipettes without introducing any air bubbles, as this can potentially disturb the ion current or even fully clog the pipette. I use Microloader (Eppendorf, Germany) for this purpose. These are specialised tips for common pipettes that have a thin, few cm long nozzle that can be inserted into the end of micro- and nanopipettes.

I fill the Microloader with 10 to 20 μl of solution and place it inside the nanopipette. It is important to start the filling process from the bottom up as otherwise air bubbles will form. If small air bubbles are present, careful flicking and rolling between the fingers can in some cases help. Otherwise the pipette has to be discarded.

A.3 MoNa Software Documentation

The Software is written in LabVIEW (version 14.0.1, National Instruments). Originally adapted for nanoinjection by Simon Hennig (Universität Bielefeld, 2012), it was further refined and developed by Alice Wilking (Universität Bielefeld, 2015).

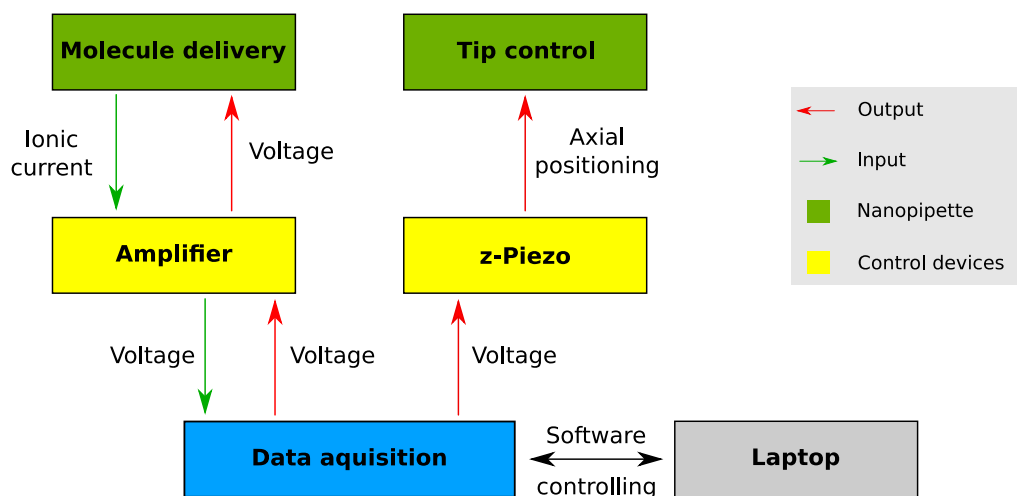


Figure 46: Schematic illustration of the communication channels between all MoNa devices. Courtesy of Alice Wilking.

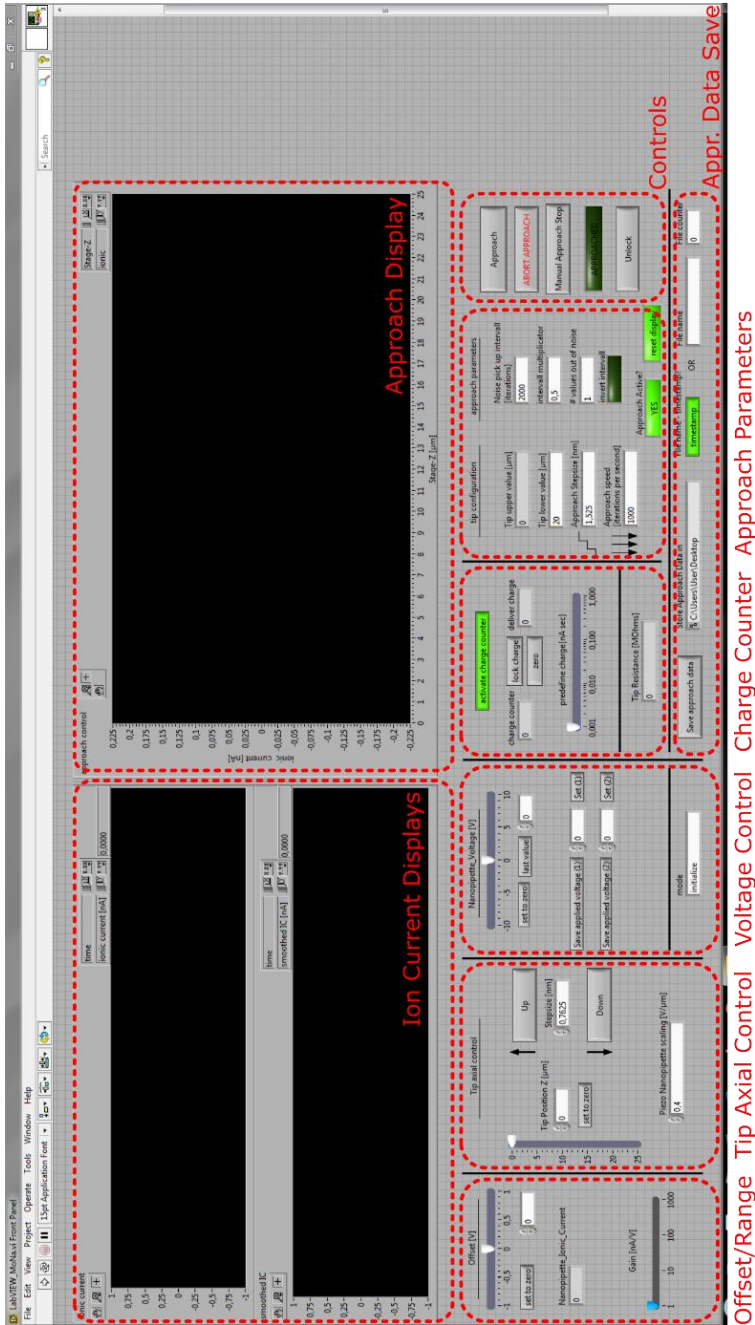


Figure 47: Screenshot of the MoNa software GUI. The ion current is displayed in real-time as raw data and smoothed data in the top left. During approach, the large display on the right is used to show the ion current over the nanopipette z-position. The offset and measuring range can be set according to the settings of the op-amp. Approach parameters such as the speed and maximal depth can be set prior to injection. Manual control of the voltage and pipette position is always possible. Additionally, the approach curve can be saved to a specific file.

A.4 MoNa Operational Amplifier Circuit

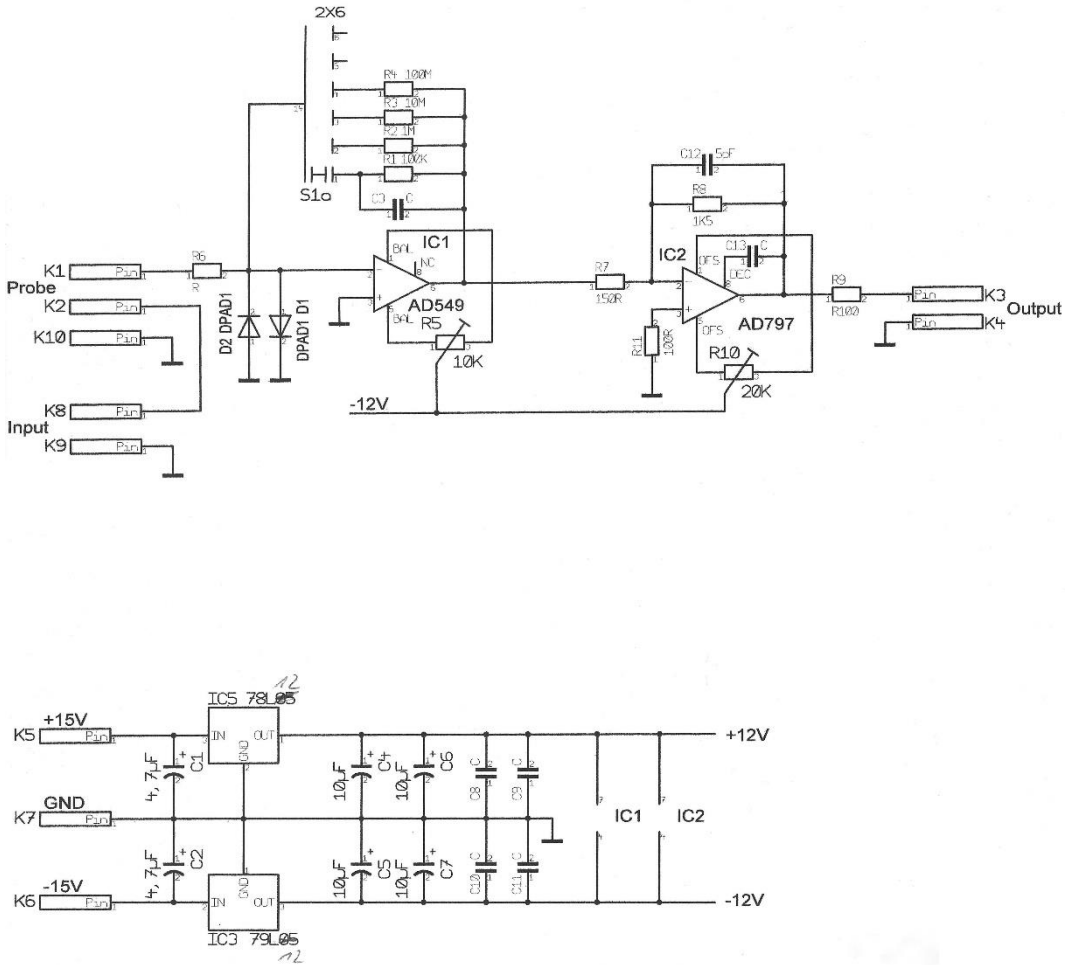


Figure 48: Circuit diagram of the op-amp. Original design and build by Herbert Bergmeier (Universität Bielefeld, Physik Elektronikwerkstatt, 2015). K1 and K2 are connected to the electrodes via alligator clips. K8 and K9 are used to supply voltage to the electrodes. They are connected via BNC (labeled “INPUT”) to the USB A/D converter (Analog-Out 0). K3 and K4 connect to the input of the USB device (Analog-In 0). This output is used to monitor the ion current. The power supply is connected through K5, K6 and K7.

A.5 Fluorescence Microscope Setup

The basis of our fluorescence microscope is the inverted IX71 (Olympus, Japan) equipped with an oil-immersion objective (APO N 1,49NA/60x, Olympus). Through a piezo-driven objective ring (PI.WS P-721.10, Physik Instrumente, Germany) and a custom-written software (MATLAB, The MathWorks, USA), three-dimensional images can be acquired. Minimal slice thickness is approx. 3 nm over a range of 100 μ m. Data (Voltage) I/O is regulated by a PCIe-card (NI PCIe-6251, National Instruments, USA) connected to two BNC breakout boxes (BNC-2090, NI).

Excitation is provided by an Argon Krypton ion laser (70C-Spectrum, Coherent, USA) with a total output power of 2.5 W. The suitable laser line can be selected by an acousto-optical tuneable filter (AOTF_nC-VIS-CN, A-A Opto Elecctronics, France). For this work only the 647 nm and 488 nm lines are used.

For detection, a cooled emCCD (iXon+ DU-888E-C00-BV, Andro, Ireland) camera is used.

A.6 Fluorophores & Filter Sets

Table 3: List of Fluorophores used in this work. All dyes are available from Thermo Fisher Scientific, except (*) from Sigma-Aldrich. The excitation and emission maxima are given in nm.

Fluorophore	Item	Exc./Emi.
Dextran Alexa 647, 10.000MW	D22914	650/668
Mito Tracker Deep Red	M22426	644/665
Phalloidin-Atto 655(*)	18846	663/684
Goat anti-Mouse Second. AB, Alexa 647 conjugate	A-21237	650/668
SYTOX Green Dead Cell Stain	S7020	504/523
Dextran Alexa 488, 3.000MW	D34682	495/519
YOYO-1 Iodine	Y3601	491/509

Table 4: Filters used for red fluorescence.

Filter	Wavelength (Bandwidth)	Item, Manufacturer
Beamsplitter	560 nm/659 nm	FF560/659-Di01, Semrock, USA
Bandpass	700 nm (75 nm)	FF01-700/75-25, Semrock, USA
Longpass (*)	665 nm	HQ665lp, Chroma, USA

Table 5: Filters used for green fluorescence.

Filter	Wavelength (Bandwidth)	Item, Manufacturer
Beamsplitter	500 nm	500DRLP, Omega Optical, USA
Bandpass	525 nm (45 nm)	XF1074/25, Omega Opt., USA
Longpass	500 nm	HQ500lp, Chroma, USA

A.7 Cell Preparation & Staining

U2OS preparation

Human bone osteosarcoma cells (U2OS) were grown in Dulbecco's Modified Eagle Medium (DMEM) with 5% fetal bovine serum (FBS) and 1% pen strep (Penicillin-Streptomycin, Thermo Fisher Scientific) added and cultivated at 37 °C in a humidified 5% CO₂ atmosphere. For all survival rate experiments, cells were transferred to 35 mm gridded culture dishes (μ -Dish, Ibidi, Germany) at the desired density and given at least 24 hours to settle down. Additional cells for STORM and PAINT experiments were transferred onto chambered glass slides (Nunc Lab-Tek II Chamber Slide, 8-well, Thermo Fisher Scientific).

C. *Reinhardtii* preparation

Chlamydomonas Reinhardtii cc124 are from the Chlamydomonas Resource Center (University of Minnesota, USA). Permanent cultures are kept on TAP (Tris-Acetate-Phosphate) agar plates (1.5% w/v) at 20 °C and 15 $\mu\text{mol m}^{-2} \text{s}^{-1}$ whitelight. They are transferred to a new plate every 8 weeks. Prior to experiments, the cells are cultivated mixotrophically in TAP medium. Some cell material from the permanent culture is inoculated with 20 ml medium inside a 50 ml Erlenmeyer flask and cultivated at 40 $\mu\text{mol m}^{-2} \text{s}^{-1}$ on an orbital shaker (120 rpm).

For nanoinjection experiments, first TAP-agar (1% w/v) is boiled up and after a short time to cool down, a single drop (approx. 20 μl) is placed in a LabTek chamber or microscope dish. The TAP-cultivated algae are taken in their mid-log growth phase (approx. 6×10^6 cells per ml) and are further diluted 1:20 with more TAP medium. 10 μl are then placed on the prepared agar-droplet.

Tubulin immunolabelling for dSTORM measurements

This protocol mainly follows Endesfelder et al. (2014) and was further adjusted and refined by Robin Diekmann (Universität Bielefeld, 2017).

Preparations:

Cytoskeleton buffer (CB):

- 80 mM Pipes (302.37 g/mol)
- 1 mM MgCl₂ (203.31 g/mol)
- 5 mM EDTA (291 g/mol)
- Adjust pH to 6.9 using aqueous KOH

Preextraction buffer (PB):

- 0.5% (v/v) Triton X-100 in CB and warm to 37 °C

Fixation buffer (FB):

- 0.5% glutaraldehyde in CB and warm to 37 °C

Freshly prepare 0.1% NaBH₄ in PBS

Prepare 100 mM Tris-HCl pH 7.3 in PBS

Prepare 5% BSA

Prepare 0.1% Triton X-100 in PBS

Fixation and labelling protocol:

- Place the sample on a planar bottle filled with 37 °C warm water or use a prewarmed copper block
- Aspirate the medium and fill the chamber with prewarmed preextraction buffer (PE), incubate for 1 min
- Aspirate the PE and fill the chamber with prewarmed fixation buffer (FB), incubate for 15 min
- Aspirate and wash 3x with PBS
- Incubate 7 min with 0.1% NaBH₄ (quenching glutaraldehyde-induced autofluorescence)
- Aspirate and wash 3x with PBS
- Incubate 7 min with 100 mM Tris-HCl pH 7.3 (quenching reactive cross-linkers)
- Aspirate and wash 3x with PBS
- Incubate 45 min with 5% BSA (blocking)
- Incubate 90 min with primary antibody 1:150 in 1.33% BSA, 0.033% Triton X-100 in PBS
- Aspirate and wash 3x with PBS

- Incubate 90 min with secondary antibody 1:200 in 1% BSA, 0.025% Triton X-100
- Aspirate and wash 5x with PBS

Imaging:

- dSTORM standard GODCAT buffer with 100 mM MEA, 2 mM COT

Ultivue DNA PAINT kit

The fixation and antibody process follows the same protocol as described above. Instead of the fluorescently labelled secondary antibody, an antibody with an attached DNA strand provided by the kit is used. Imaging buffer and fluorophores are provided with the kit.

A.8 Additional Materials & Methods

PBS

Phosphate buffered solution was produced by solving one tablet (P4417, Sigma-Aldrich, USA) in 200ml double distilled water. Before use, it is important that the tablet is fully dissolved to avoid clogging of the nanopipette

For cell culture use, an already prepared, sterile and filtered PBS solution (Dulbecco's Phosphate Buffered Saline, Sigma-Aldrich, USA) is utilized.

Calibration Samples (Fluorescent Bead Slides)

There are two different bead slides used in this work. The first one is a simple bead slide, that displays a low-density surface of small, fluorescent 100-nm beads stuck to the cover glass for measuring the PSF of the optical system. A small drop of TetraSpeck (0.1 μm , Molecular Probes, USA) stock solution diluted 1:40,000 in ddH₂O is placed on a cover glass and let to dry. Afterwards, an additional drop of water is placed in the same spot. For longer durability, a second cover glass can be placed on the drop and then sealed with lacquer.

The second slide is more elaborate and consists of three different sizes of beads. The first step is the same. A small drop (approx. 10 μl) of the TetraSpeck solution is deposited onto a cover glass and let to dry. The larger beads (Dynabeads M-280 Streptavidin, Thermo Fisher Scientific, USA and COMPEL Magnetic Streptavidin modified 8 μm , Bangs Laboratories, USA) are coated in streptavidin, so we choose a

biotin conjugated fluorophore (Alexa Fluor 647 biotin conjugate, Thermo Fisher Scientific, USA) to coat the surface of them. For this process, 5 μl of each microsphere dispersion are incubated for 30 minutes at room temperature with 100 μl 10^{-7}M dye solution in ddH₂O while slowly shaking on a vortexer (approx. 100 rpm). After incubation, a quickspin up to 15 krpm in a centrifuge and washing with 100 μl ddH₂O is repeated three times to get rid of any free fluorophores. The last time, phosphate buffered saline (PBS) is used to redissolve the pallet and one drop is placed on the dried out TetraSpeck dispersion. For durability, once again, a second cover glass can be used to seal the slide with lacquer.

SMLM image reconstruction

For all reconstructions of raw single molecule data, I used the ThunderSTORM (Ovesný et al. 2014) plugin for the public domain, Java-based image processing program ImageJ (Schindelin et al. 2015). This free software package also allows the calibration and reconstruction of 3D datasets.

For 2D reconstructions, settings were kept on the default settings. For 3D reconstructions, the B-spline scale was increased from 2 to 3, because the broader PSF would otherwise lead to multiple localisations.

List of Figures

Figure	Page
Schematic illustration of cell delivery methods	2
Fluorescence images	8
Fluorescence and phosphorescence principles	9
Transition probabilities and spectra	9
Airy pattern shape	10
Illustration of the Rayleigh criterion	11
Fluorescence microscope setup and illumination modes	13
Illustration of the SMLM principle	17
Original PAINT principle	19
The principle of 3D STORM	22
Nanoinjection principle	24
Nanopipette simulations	28
Time-lapse of U2OS cells injected with DAF	32
Statistics of cell survival after injection with different timings and voltages	33
Overlay of whitelight and red fluorescence images of U2OS cells	34
Cell state 24 hours after injection with 100 nm and 500 nm pipettes	35
Size comparisons of different injection probes	37
100 min. time-lapse of U2OS cells injected with DAF	39
Mobile nanoinjection system parts	46
Mean noise levels	48
Ion current approach curves of the two different systems	50
Nanoinjection of Mito Tracker Deep Red	51
Nanoinjection of Atto 655 Phalloidin	51
Examples of MoNa attached to different systems	53
Axial cross-sections of PSFs acquired under different conditions	56
FWHM of the PSFs dependent on the immersion oil	58
Statistics of localisations and their respective sigmas	59
Schematic side-view image of the 3D calibration sample	60
Side-view of three sizes of fluorescent beads	61
Comparison of 3D STORM images using different immersion oils	62

Figure	Page
Single molecule localisations per 50 frames and injection voltages	66
Reconstructed SMLM image of the actin structure of a U2OS cell	67
Time dependency of localization frequency	68
Widefield and super-resolved images of labelled actin	69
3D reconstruction image of actin filaments of a living U2OS cell	71
3D reconstruction of an entire living U2OS cell	72
Schematic illustration of a single alga	75
Schematic illustration of the injection setup previously reported	77
Schematic illustration of sample preparation and nanoinjection	78
Injection of one alga with Dextran Alexa Fluor 488	79
Images and illustration of the heating & cooling stage	83
IR temperature measurements	84
Cooling with the temperature stage	85
Number of publications during the last two decades	89
Illustration of single cell delivery method attributes	90
Schematic illustration of the channels between all MoNa devices	93
Screenshot of the MoNa software GUI	94
Circuit diagram of the op-amp	95

List of Tables

Table	Page
Rough price comparison of our two different injection systems	49
Summary of the viability experiments	91
List of Fluorophores used in this work	96
Filters used for red fluorescence	96
Filters used for green fluorescence	97

List of Abbreviations

ADC	Analog-to-Digital Converter
AFM	Atomic Force Microscopy
BNC	Bayonet Neill Concelman
Cas9	CRISPR associated protein 9
CCD	Charge-Coupled Device
CMOS	Complementary Metal-Oxide-Semiconductor
CRISPR	Clustered Regularly Interspaced Short Palindromic Repeats
DAC	Digital-to-Analog Converter
DAF	Dextran Alexa Fluor 647
ddH ₂ O	Double-Distilled Water
DMEM	Dulbecco's Modified Eagle's Medium
DMSO	Dimethyl Sulfoxide
DNA	Deoxyribonucleic Acid
dSTORM	direct Stochastic Optical Reconstruction Microscopy
emCCD	electron multiplying Charge-Coupled Device
EPI	Epifluorescence
FWHM	Full Width at Half Maximum
gRNA	guide Ribonucleic Acid
HILO	Highly Inclined and Laminated Optical (illumination)
id	inner diameter
LED	Light Emitting Diode
MoNa	Mobile Nanoinjection
MOSFET	Metal-Oxide-Semiconductor Field-Effect Transistor
NA	Numerical Aperture
od	outer diameter
op-amp	Operational Amplifier
PAINT	Point Accumulation for Imaging in Nanoscale Topography
PALM	Photo-Activated Localization Microscopy
PBS	Phosphate Buffered Saline
PFA	Paraformaldehyde
PID	Proportional-Integral-Derivative

PSF	Point Spread Function
PWM	Pulse-Width Modulation
RNA	Ribonucleic Acid
RNP	Ribonucleoprotein Complex
sCMOS	scientific Complementary Metal-Oxide-Semiconductor
SEM	Scanning Electron Microscopy
SICM	Scanning Ion Conductance Microscopy
SIM	Structured Illumination Microscopy
SMLM	Single Molecule Localization Microscopy
SNR	Signal-to-Noise Ratio
SOFI	Super-resolution Optical Fluctuation Imaging
STED	Stimulated Emission Depletion Microscopy
STORM	Stochastic Optical Reconstruction Microscopy
SXG	SYTOX Green nucleic acid stain
TIR(F)	Total Internal Reflection (Fluorescence)
TAP	Tris-Acetate-Phosphate
U2OS	Human Bone Osteosarcoma Epithelial Cells

References

- Abbe, E. (1873): Beiträge zur Theorie des Mikroskops und der mikroskopischen Wahrnehmung. In: *Archiv f. mikrosk. Anatomie* 9 (1), S. 413–418. DOI: 10.1007/BF02956173.
- Actis, Paolo; Maalouf, Michelle M.; Kim, Hyunsung John; Lohith, Akshar; Vilozy, Boaz; Seger, R. Adam; Pourmand, Nader (2014a): Compartmental genomics in living cells revealed by single-cell nanobiopsy. In: *ACS nano* 8 (1), S. 546–553. DOI: 10.1021/nm405097u.
- Actis, Paolo; Tokar, Sergiy; Clausmeyer, Jan; Babakinejad, Babak; Mikhaleva, Sofya; Cornut, Renaud et al. (2014b): Electrochemical nanoprobe for single-cell analysis. In: *ACS nano* 8 (1), S. 875–884. DOI: 10.1021/nm405612q.
- Adam Seger, R.; Actis, Paolo; Penfold, Catherine; Maalouf, Michelle; Vilozy, Boaz; Pourmand, Nader (2012): Voltage controlled nano-injection system for single-cell surgery. In: *Nanoscale* 4 (19), S. 5843–5846. DOI: 10.1039/c2nr31700a.
- Ambrose, E. J. (1956): A Surface Contact Microscope for the study of Cell Movements. In: *Nature* 178 (4543), S. 1194. DOI: 10.1038/1781194a0.
- Anderson, Sean E.; Bau, Haim H. (2014): Electrical detection of cellular penetration during microinjection with carbon nanopipettes. In: *Nanotechnology* 25 (24), S. 245102. DOI: 10.1088/0957-4484/25/24/245102.
- Axelrod, D. (1981): Cell-substrate contacts illuminated by total internal reflection fluorescence. In: *The Journal of cell biology* 89 (1), S. 141–145. DOI: 10.1083/jcb.89.1.141.
- Besseling, T. H.; Jose, J.; van Blaaderen, A. (2015): Methods to calibrate and scale axial distances in confocal microscopy as a function of refractive index. In: *Journal of microscopy* 257 (2), S. 142–150. DOI: 10.1111/jmi.12194.
- Betzig, Eric; Patterson, George H.; Sougrat, Rachid; Lindwasser, O. Wolf; Olenych, Scott; Bonifacino, Juan S. et al. (2006): Imaging intracellular fluorescent proteins at nanometer resolution. In: *Science (New York, N.Y.)* 313 (5793), S. 1642–1645. DOI: 10.1126/science.1127344.

- Binnig; Quate; Gerber (1986): Atomic force microscope. In: *Physical review letters* 56 (9), S. 930–933. DOI: 10.1103/PhysRevLett.56.930.
- Bruckbauer, Andreas; Ying, Liming; Rothery, Alison M.; Zhou, Dejian; Shevchuk, Andrew I.; Abell, Chris et al. (2002): Writing with DNA and Protein Using a Nanopipet for Controlled Delivery. In: *J. Am. Chem. Soc.* 124 (30), S. 8810–8811. DOI: 10.1021/ja026816c.
- Calander, Nils (2009): Analyte concentration at the tip of a nanopipette. In: *Analytical chemistry* 81 (20), S. 8347–8353. DOI: 10.1021/ac901142z.
- Canatella, Paul J.; Karr, Joan F.; Petros, John A.; Prausnitz, Mark R. (2001): Quantitative Study of Electroporation-Mediated Molecular Uptake and Cell Viability. In: *Biophysical journal* 80 (2), S. 755–764. DOI: 10.1016/S0006-3495(01)76055-9.
- Chamma, Ingrid; Letellier, Mathieu; Butler, Corey; Tessier, Béatrice; Lim, Kok-Hong; Gauthereau, Isabel et al. (2016): Mapping the dynamics and nanoscale organization of synaptic adhesion proteins using monomeric streptavidin. In: *Nature communications* 7, S. 10773. DOI: 10.1038/ncomms10773.
- Davis, B. R.; Yannariello-Brown, J.; Prokopishyn, N. L.; Luo, Z.; Smith, M. R.; Wang, J. et al. (2000): Glass needle-mediated microinjection of macromolecules and transgenes into primary human blood stem/progenitor cells. In: *Blood* 95 (2), S. 437–444.
- Demmerle, Justin; Innocent, Cassandravictoria; North, Alison J.; Ball, Graeme; Müller, Marcel; Miron, Ezequiel et al. (2017): Strategic and practical guidelines for successful structured illumination microscopy. In: *Nature protocols* 12 (5), S. 988–1010. DOI: 10.1038/nprot.2017.019.
- DePamphilis, M. L.; Herman, S. A.; Martínez-Salas, E.; Chalifour, L. E.; Wirak, D. O.; Cupo, D. Y.; Miranda, M. (1988): Microinjecting DNA into mouse ova to study DNA replication and gene expression and to produce transgenic animals. In: *BioTechniques* 6 (7), S. 662–680.
- Dertinger, Thomas; Colyer, Ryan; Vogel, Robert; Heilemann, Mike; Sauer, Markus; Enderlein, Jörg; Weiss, Shimon (2012): Superresolution optical fluctuation imaging (SOFI). In: *Advances in experimental medicine and biology* 733, S. 17–21. DOI: 10.1007/978-94-007-2555-3_2.

- Diaspro, Alberto; Federici, Federico; Robello, Mauro (2002): Influence of refractive-index mismatch in high-resolution three-dimensional confocal microscopy. In: *Applied optics* 41 (4), S. 685–690.
- Doudna, Jennifer A.; Charpentier, Emmanuelle (2014): Genome editing. The new frontier of genome engineering with CRISPR-Cas9. In: *Science (New York, N.Y.)* 346 (6213), S. 1258096. DOI: 10.1126/science.1258096.
- Endesfelder, Ulrike; Malkusch, Sebastian; Fricke, Franziska; Heilemann, Mike (2014): A simple method to estimate the average localization precision of a single-molecule localization microscopy experiment. In: *Histochemistry and cell biology* 141 (6), S. 629–638. DOI: 10.1007/s00418-014-1192-3.
- Felgner, P. L.; Gadek, T. R.; Holm, M.; Roman, R.; Chan, H. W.; Wenz, M. et al. (1987): Lipofection: a highly efficient, lipid-mediated DNA-transfection procedure. In: *Proceedings of the National Academy of Sciences of the United States of America* 84 (21), S. 7413–7417.
- Fitzgerald, James E.; Lu, Ju; Schnitzer, Mark J. (2012): Estimation theoretic measure of resolution for stochastic localization microscopy. In: *Physical review letters* 109 (4), S. 48102. DOI: 10.1103/PhysRevLett.109.048102.
- GE Healthcare (2017): Immersion Oil Calculator Web App. Online verfügbar unter <http://www.gelifesciences.com/webapp/wcs/stores/servlet/catalog/en/GELifeSciences-de/service-and-support/immersion-oil-calculator-web-app>.
- Gerlach, Dieter (2009): Geschichte der Mikroskopie. 1. Auflage. Frankfurt am Main: Verlag Harri Deutsch.
- Giannone, Gregory; Hosy, Eric; Levet, Florian; Constals, Audrey; Schulze, Katrin; Sobolevsky, Alexander I. et al. (2010): Dynamic superresolution imaging of endogenous proteins on living cells at ultra-high density. In: *Biophysical journal* 99 (4), S. 1303–1310. DOI: 10.1016/j.bpj.2010.06.005.
- Gibson, S. F.; Lanni, F. (1992): Experimental test of an analytical model of aberration in an oil-immersion objective lens used in three-dimensional light microscopy. In: *Journal of the Optical Society of America. A, Optics and image science* 9 (1), S. 154–166.
- Graessmann, M.; Graessmann, A. (1983): Microinjection of tissue culture cells. In: *Methods in enzymology* 101, S. 482–492.

- Greenbaum, L.; Rothmann, C.; Lavie, R.; Malik, Z. (2000): Green fluorescent protein photobleaching: a model for protein damage by endogenous and exogenous singlet oxygen. In: *Biological chemistry* 381 (12), S. 1251–1258. DOI: 10.1515/BC.2000.153.
- Guillaume-Gentil, Orane; Potthoff, Eva; Ossola, Dario; Franz, Clemens M.; Zambelli, Tomaso; Vorholt, Julia A. (2014): Force-controlled manipulation of single cells: from AFM to FluidFM. In: *Trends in biotechnology* 32 (7), S. 381–388. DOI: 10.1016/j.tibtech.2014.04.008.
- Gustafsson, M. G. (2000): Surpassing the lateral resolution limit by a factor of two using structured illumination microscopy. In: *Journal of microscopy* 198 (Pt 2), S. 82–87.
- Haitinger, Max (1938): Fluoreszenzmikroskopie. Ihre Anwendung in der Histologie und Chemie. Leipzig: Akademische Verlagsgesellschaft.
- Hansma, P.; Drake, B.; Marti, O.; Gould, S.; Prater, C. (1989): The scanning ion-conductance microscope. In: *Science* 243 (4891), S. 641–643. DOI: 10.1126/science.2464851.
- Hapala, I. (1997): Breaking the barrier: methods for reversible permeabilization of cellular membranes. In: *Critical reviews in biotechnology* 17 (2), S. 105–122. DOI: 10.3109/07388559709146609.
- Heilemann, Mike; van de Linde, Sebastian; Schüttpelz, Mark; Kasper, Robert; Seefeldt, Britta; Mukherjee, Anindita et al. (2008): Subdiffraction-resolution fluorescence imaging with conventional fluorescent probes. In: *Angewandte Chemie (International ed. in English)* 47 (33), S. 6172–6176. DOI: 10.1002/anie.200802376.
- Heimstädt, Oskar (1911): Das Fluoreszenzmikroskop. In: *Zeitschrift für wissenschaftliche Mikroskopie* (28), S. 330–337.
- Hell, S. W.; Wichmann, J. (1994): Breaking the diffraction resolution limit by stimulated emission: stimulated-emission-depletion fluorescence microscopy. In: *Optics letters* 19 (11), S. 780–782.
- Hennig, Simon; van de Linde, Sebastian; Bergmann, Stephan; Huser, Thomas; Sauer, Markus (2015a): Quantitative Super-Resolution Microscopy of Nanopipette-Deposited Fluorescent Patterns. In: *ACS nano* 9 (8), S. 8122–8130. DOI: 10.1021/acsnano.5b02220.

- Hennig, Simon; van de Linde, Sebastian; Lummer, Martina; Simonis, Matthias; Huser, Thomas; Sauer, Markus (2015b): Instant live-cell super-resolution imaging of cellular structures by nanoinjection of fluorescent probes. In: *Nano letters* 15 (2), S. 1374–1381. DOI: 10.1021/nl504660t.
- Hess, Samuel T.; Girirajan, Thanu P. K.; Mason, Michael D. (2006): Ultra-high resolution imaging by fluorescence photoactivation localization microscopy. In: *Biophysical journal* 91 (11), S. 4258–4272. DOI: 10.1529/biophysj.106.091116.
- Holden, Seamus J.; Uphoff, Stephan; Kapanidis, Achillefs N. (2011): DAOSTORM: an algorithm for high- density super-resolution microscopy. In: *Nature methods* 8 (4), S. 279–280. DOI: 10.1038/nmeth0411-279.
- Holm, Thorge; Klein, Teresa; Löschberger, Anna; Klamp, Tobias; Wiebusch, Gerd; van de Linde, Sebastian; Sauer, Markus (2014): A blueprint for cost-efficient localization microscopy. In: *Chemphyschem : a European journal of chemical physics and physical chemistry* 15 (4), S. 651–654. DOI: 10.1002/cphc.201300739.
- Huang, Bo; Wang, Wenqin; Bates, Mark; Zhuang, Xiaowei (2008): Three-dimensional super-resolution imaging by stochastic optical reconstruction microscopy. In: *Science (New York, N.Y.)* 319 (5864), S. 810–813. DOI: 10.1126/science.1153529.
- Jiang, Wenzhi; Bruggeman, Andrew J.; Horken, Kempton M.; Plucinak, Thomas M.; Weeks, Donald P. (2014): Successful transient expression of Cas9 and single guide RNA genes in *Chlamydomonas reinhardtii*. In: *Eukaryotic cell* 13 (11), S. 1465–1469. DOI: 10.1128/EC.00213-14.
- Jungmann, Ralf; Avendaño, Maier S.; Woehrstein, Johannes B.; Dai, Mingjie; Shih, William M.; Yin, Peng (2014): Multiplexed 3D cellular super-resolution imaging with DNA-PAINT and Exchange-PAINT. In: *Nature methods* 11 (3), S. 313–318. DOI: 10.1038/nmeth.2835.
- Kaplan, Charlotte; Ewers, Helge (2015): Optimized sample preparation for single-molecule localization-based superresolution microscopy in yeast. In: *Nature protocols* 10 (7), S. 1007–1021. DOI: 10.1038/nprot.2015.060.
- Kim, Hyongbum; Kim, Jin-Soo (2014): A guide to genome engineering with programmable nucleases. In: *Nature reviews. Genetics* 15 (5), S. 321–334. DOI: 10.1038/nrg3686.

- Kubitscheck, Ulrich (2013): Fluorescence microscopy. From principles to biological applications. Weinheim: Wiley-Blackwell.
- Laforge, François O.; Carpino, James; Rotenberg, Susan A.; Mirkin, Michael V. (2007): Electrochemical attosyringe. In: *Proceedings of the National Academy of Sciences of the United States of America* 104 (29), S. 11895–11900. DOI: 10.1073/pnas.0705102104.
- Lakowicz, Joseph R. (2006): Principles of fluorescence spectroscopy. 3. ed. New York, NY: Springer.
- Landers, James P. (2007): Handbook of Capillary and Microchip Electrophoresis and Associated Microtechniques, Third Edition. Hoboken: Taylor & Francis. Online verfügbar unter <http://gbv.ebib.com/patron/FullRecord.aspx?p=321564>.
- Legant, Wesley R.; Shao, Lin; Grimm, Jonathan B.; Brown, Timothy A.; Milkie, Daniel E.; Avants, Brian B. et al. (2016): High-density three-dimensional localization microscopy across large volumes. In: *Nature methods* 13 (4), S. 359–365. DOI: 10.1038/nmeth.3797.
- Li, Dongqing (2004): Electrokinetics in microfluidics. 1. ed. Amsterdam [u.a.]: Elsevier (Interface science and technology, 2).
- Li, Miao; Lohmuller, Theobald; Feldmann, Jochen (2015): Optical injection of gold nanoparticles into living cells. In: *Nano letters* 15 (1), S. 770–775. DOI: 10.1021/nl504497m.
- Luo, Qingming; Deng, Yong; Huang, Zhenli; Li, Yu; Xing, Da; Zhang, Zhihong (Hg.) (2017): Advances in molecular biophotonics. Berlin, Shanghai: De Gruyter (Advances in optical physics, 5).
- Mauro, Alexander (1980): Dielectrophoresis. The Behavior of Neutral Matter in Nonuniform Electric Fields. Herbert A. Pohl. In: *The Quarterly Review of Biology* 55 (1), S. 68–69. DOI: 10.1086/411635.
- McCarthy, Sarah S.; Kobayashi, Marilyn C.; Niyogi, Krishna K. (2004): White mutants of *Chlamydomonas reinhardtii* are defective in phytoene synthase. In: *Genetics* 168 (3), S. 1249–1257. DOI: 10.1534/genetics.104.030635.
- McNeil, P. L.; Warder, E. (1987): Glass beads load macromolecules into living cells. In: *Journal of cell science* 88 (Pt 5), S. 669–678.

- Meister, André; Gabi, Michael; Behr, Pascal; Studer, Philipp; Vörös, János; Niedermann, Philippe et al. (2009): FluidFM: combining atomic force microscopy and nanofluidics in a universal liquid delivery system for single cell applications and beyond. In: *Nano letters* 9 (6), S. 2501–2507. DOI: 10.1021/nl901384x.
- Monkemoller, Viola; Oie, Cristina; Hubner, Wolfgang; Huser, Thomas; McCourt, Peter (2015): Multimodal super-resolution optical microscopy visualizes the close connection between membrane and the cytoskeleton in liver sinusoidal endothelial cell fenestrations. In: *Scientific reports* 5, S. 16279. DOI: 10.1038/srep16279.
- Neumann, E.; Schaefer-Ridder, M.; Wang, Y.; Hofschneider, P. H. (1982): Gene transfer into mouse lyoma cells by electroporation in high electric fields. In: *The EMBO journal* 1 (7), S. 841–845.
- Ovesný, Martin; Křížek, Pavel; Borkovec, Josef; Svindrych, Zdeněk; Hagen, Guy M. (2014): ThunderSTORM: a comprehensive ImageJ plug-in for PALM and STORM data analysis and super-resolution imaging. In: *Bioinformatics (Oxford, England)* 30 (16), S. 2389–2390. DOI: 10.1093/bioinformatics/btu202.
- Pepperkok, R.; Schneider, C.; Philipson, L.; Ansorge, W. (1988): Single cell assay with an automated capillary microinjection system. In: *Experimental cell research* 178 (2), S. 369–376.
- Perkel, Jeffrey M. (2017): Single-cell biology. The power of one. In: *Science*. DOI: 10.1126/science.opms.p1500099.
- Rayleigh (1879): XXXI. Investigations in optics, with special reference to the spectroscope. In: *Philosophical Magazine Series 5* 8 (49), S. 261–274. DOI: 10.1080/14786447908639684.
- Reuss, F. F. (1809): Sur un nouvel effet de l'électricité galvanique. In: *Mémoires de la Société Impériale des Naturalistes de Moscou* (2), S. 327–337.
- Rheinlaender, Johannes; Schäffer, Tilman E. (2009): Image formation, resolution, and height measurement in scanning ion conductance microscopy. In: *Journal of Applied Physics* 105 (9), S. 94905. DOI: 10.1063/1.3122007.
- Rust, Michael J.; Bates, Mark; Zhuang, Xiaowei (2006): Sub-diffraction-limit imaging by stochastic optical reconstruction microscopy (STORM). In: *Nature methods* 3 (10), S. 793–795. DOI: 10.1038/nmeth929.

- Sage, Daniel; Kirshner, Hagai; Pengo, Thomas; Stuurman, Nico; Min, Junhong; Manley, Suliana; Unser, Michael (2015): Quantitative evaluation of software packages for single-molecule localization microscopy. In: *Nature methods* 12 (8), S. 717–724. DOI: 10.1038/nmeth.3442.
- Schierenbeck, Lisa; Ries, David; Rogge, Kristin; Grewe, Sabrina; Weisshaar, Bernd; Kruse, Olaf (2015): Fast forward genetics to identify mutations causing a high light tolerant phenotype in *Chlamydomonas reinhardtii* by whole-genome-sequencing. In: *BMC genomics* 16, S. 57. DOI: 10.1186/s12864-015-1232-y.
- Schindelin, Johannes; Rueden, Curtis T.; Hiner, Mark C.; Eliceiri, Kevin W. (2015): The ImageJ ecosystem: An open platform for biomedical image analysis. In: *Molecular reproduction and development* 82 (7-8), S. 518–529. DOI: 10.1002/mrd.22489.
- Schrlau, Michael G.; Falls, Erica M.; Ziober, Barry L.; Bau, Haim H. (2008): Carbon nanopipettes for cell probes and intracellular injection. In: *Nanotechnology* 19 (1), S. 15101. DOI: 10.1088/0957-4484/19/01/015101.
- Scranton, Melissa A.; Ostrand, Joseph T.; Fields, Francis J.; Mayfield, Stephen P. (2015): *Chlamydomonas* as a model for biofuels and bio-products production. In: *The Plant journal : for cell and molecular biology* 82 (3), S. 523–531. DOI: 10.1111/tpj.12780.
- Sharonov, Alexey; Hochstrasser, Robin M. (2006): Wide-field subdiffraction imaging by accumulated binding of diffusing probes. In: *Proceedings of the National Academy of Sciences of the United States of America* 103 (50), S. 18911–18916. DOI: 10.1073/pnas.0609643104.
- Shevchuk, Andrew I.; Frolenkov, Gregory I.; Sánchez, Daniel; James, Peter S.; Freedman, Noah; Lab, Max J. et al. (2006): Imaging proteins in membranes of living cells by high-resolution scanning ion conductance microscopy. In: *Angewandte Chemie (International ed. in English)* 45 (14), S. 2212–2216. DOI: 10.1002/anie.200503915.
- Shin, Sung-Eun; Lim, Jong-Min; Koh, Hyun Gi; Kim, Eun Kyung; Kang, Nam Kyu; Jeon, Seungjib et al. (2016): CRISPR/Cas9-induced knockout and knock-in mutations in *Chlamydomonas reinhardtii*. In: *Scientific reports* 6, S. 27810. DOI: 10.1038/srep27810.

- Simonis, Matthias; Hubner, Wolfgang; Wilking, Alice; Huser, Thomas; Hennig, Simon (2017): Survival rate of eukaryotic cells following electrophoretic nanoinjection. In: *Scientific reports* 7, S. 41277. DOI: 10.1038/srep41277.
- Singhal, Riju; Orynbayeva, Zulfiya; Kalyana Sundaram, Ramalingam Venkat; Niu, Jun Jie; Bhattacharyya, Sayan; Vitol, Elina A. et al. (2011): Multifunctional carbon-nanotube cellular endoscopes. In: *Nature nanotechnology* 6 (1), S. 57–64. DOI: 10.1038/nnano.2010.241.
- Sinkó, József; Kákonyi, Róbert; Rees, Eric; Metcalf, Daniel; Knight, Alex E.; Kaminski, Clemens F. et al. (2014): TestSTORM: Simulator for optimizing sample labeling and image acquisition in localization based super-resolution microscopy. In: *Biomedical optics express* 5 (3), S. 778–787. DOI: 10.1364/BOE.5.000778.
- Strehlow, David; Gilbert, Walter (1993): A fate map for the first cleavages of the zebrafish. In: *Nature* 361 (6411), S. 451–453. DOI: 10.1038/361451a0.
- Thompson, N. L.; Burghardt, T. P.; Axelrod, D. (1981): Measuring surface dynamics of biomolecules by total internal reflection fluorescence with photobleaching recovery or correlation spectroscopy. In: *Biophysical journal* 33 (3), S. 435–454. DOI: 10.1016/S0006-3495(81)84905-3.
- Thompson, Russell E.; Larson, Daniel R.; Webb, Watt W. (2002): Precise Nanometer Localization Analysis for Individual Fluorescent Probes. In: *Biophysical journal* 82 (5), S. 2775–2783. DOI: 10.1016/S0006-3495(02)75618-X.
- Thorne, H. V. (1966): Electrophoretic separation of polyoma virus DNA from host cell DNA. In: *Virology* 29 (2), S. 234–239.
- Tokunaga, Makio; Imamoto, Naoko; Sakata-Sogawa, Kumiko (2008): Highly inclined thin illumination enables clear single-molecule imaging in cells. In: *Nature methods* 5 (2), S. 159–161. DOI: 10.1038/nmeth1171.
- Velve Casquillas, Guilhem; Fu, Chuanhai; Le Berre, Mael; Cramer, Jeremy; Meance, Sebastien; Plecis, Adrien et al. (2011): Fast microfluidic temperature control for high resolution live cell imaging. In: *Lab on a chip* 11 (3), S. 484–489. DOI: 10.1039/C0LC00222D.
- Viigipuu, Katrin; Kallio, Pasi (2004): Microinjection of living adherent cells by using a semi-automatic microinjection system. In: *Alternatives to laboratory animals : ATLA* 32 (4), S. 417–423.

- Visser, T. D.; Oud, J. L. (1994): Volume measurements in three-dimensional microscopy. In: *Scanning* 16 (4), S. 198–200. DOI: 10.1002/sca.4950160403.
- Wäldchen, Sina; Lehmann, Julian; Klein, Teresa; van de Linde, Sebastian; Sauer, Markus (2015): Light-induced cell damage in live-cell super-resolution microscopy. In: *Scientific reports* 5, S. 15348. DOI: 10.1038/srep15348.
- Wang, Wenhui; Sun, Yu; Zhang, Ming; Anderson, Robin; Langille, Lowell; Chan, Warren (2008): A system for high-speed microinjection of adherent cells. In: *The Review of scientific instruments* 79 (10), S. 104302. DOI: 10.1063/1.3006000.
- Wilson, Aubrey M.; Aten, Quentin T.; Toone, Nathan C.; Black, Justin L.; Jensen, Brian D.; Tamowski, Susan et al. (2013): Transgene delivery via intracellular electroporetic nanoinjection. In: *Transgenic research* 22 (5), S. 993–1002. DOI: 10.1007/s11248-013-9706-7.
- Xing, Yan-Fei; Yang, Chuan-Lu; Mo, Yong-Fang; Wang, Mei-Shan; Ma, Xiao-Guang (2014): Spontaneous nanoinjection with carbon nanotubes. A molecular dynamics simulation study. In: *J. Mater. Chem. B* 2 (7), S. 859–867. DOI: 10.1039/C3TB21468K.
- Ying, Liming; White, Samuel S.; Bruckbauer, Andreas; Meadows, Lisa; Korchev, Yuri E.; Klenerman, David (2004): Frequency and voltage dependence of the dielectrophoretic trapping of short lengths of DNA and dCTP in a nanopipette. In: *Biophysical journal* 86 (2), S. 1018–1027. DOI: 10.1016/S0006-3495(04)74177-6.
- Yuan, Guo-Cheng; Cai, Long; Elowitz, Michael; Enver, Tariq; Fan, Guoping; Guo, Guoji et al. (2017): Challenges and emerging directions in single-cell analysis. In: *Genome biology* 18 (1), S. 84. DOI: 10.1186/s13059-017-1218-y.
- Yum, Kyungsuk; Wang, Ning; Yu, Min-Feng (2010): Nanoneedle: a multifunctional tool for biological studies in living cells. In: *Nanoscale* 2 (3), S. 363–372. DOI: 10.1039/b9nr00231f.
- Zhou, Xuewen; Zhang, Xixi; Boualavong, Jonathan; Durney, Andrew R.; Wang, Tonghui; Kirschner, Scott et al. (2017): Electrokinetically controlled fluid injection into unicellular microalgae. In: *Electrophoresis*. DOI: 10.1002/elps.201600548.

Publications & Conferences

Simonis, M., Diekmann, R., Schüttpelz, M., Hennig, S., and Huser, T. (2017):
Choosing the Right Immersion Oil for optical Microscopy.
Manuscript in preparation.

Simonis, M., Wilking, A., Huser, T., and Hennig, S. (2017):
MoNa – A Cost-Efficient, Portable Nanoinjection System.
Submitted.

Simonis, M., Hübner, W., Wilking, A., Huser, T., and Hennig, S. (2017):
Survival rate of eukaryotic cells following electrophoretic nanoinjection.
Scientific Reports 7, 41277

Hennig, S., van de Linde, S., Lummer, M., Simonis, M., Huser, T., Sauer, M. (2015):
Instant Live-Cell Super-Resolution Imaging of Cellular Structures by Nanoinjection
of Fluorescent Probes.
ACSNano Letters 15, 1374—1381

Simonis, M., Wilking, A., Huser, T., and Hennig, S. (2016):
MoNa – A Cost-Efficient, Portable Nanoinjection System
7th NRW Nano-Conference (Münster, 12/2016), 2. Place Poster-Award

Simonis, M., Hennig, S., and Huser, T. (2014):
Survival Rate of Eukaryotic Cells after Nanoinjection
20th Workshop on Single Molecule Spectroscopy (Berlin-Adlershof, 09/2014), Poster

Simonis, M., Hennig, S., and Huser, T. (2013):
3D Deconvolution Microscopy and Nanoinjection
Science Fair, Perspektive (Bielefeld, 11/2013), Poster

Acknowledgements

Mein erster Dank gilt meinem Doktorvater Prof. Dr. Thomas Huser, der diese Arbeit ermöglicht hat und für meine Fragen und Probleme immer eine offene Tür hatte.

Danke an meinen Zweitkorrektor Prof. Dr. Andreas Hütten und an Prof. Dr. Dario Anselmetti und Prof. Dr. Edwin Laermann für die schnelle und unkomplizierte Planung meiner Verteidigung.

Dr. Simon Hennig danke ich für die tatkräftige Unterstützung und tolle Betreuung seit meiner Masterzeit. Ohne ihn gäbe es Nanoinjection in ihrer jetzigen Form nicht.

Für das kritische Hinterfragen von meinen Ergebnissen und die Hilfe bei biologischen Fragestellungen danke ich Dr. Wolfgang Hübner.

Natürlich muss ich auch Dr. Gerd Wiebusch für die Zeit bei technischen Fragen und Reinhild Pätzmann für organisatorisches Talent danken.

Ich danke Nina Lämmermann, Dr. Jan H. Mussnug und Dr. Kyle J. Lauersen aus der Arbeitsgruppe „Algae Biotechnology & Bioenergy Research“ von Prof. Dr. Olaf Kruse für die Zusammenarbeit an *Chlamydomonas reinhardtii* und die Präparation der Algen.

Einen ganz großen Dank an mein tolles Büro: Robin Diekmann für die Idee und Mitarbeit beim „rumgeöle“. Stephan Bergmann für das gemeinsame Auf- und Abreißen unseres Setups. Alice Wilking für das konstruktive Mitwirken an MoNa. Zusätzlicher Dank an alle drei für eine tolle Organisation (Bestellungen, Getränke, Grillabende, Seminar, etc. etc.) und natürlich die unglaublich schöne Atmosphäre in unserem Büro. Möge die Obstschüssel weiterhin gut gefüllt bleiben.

Generell ein Dankeschön an die gesamte Arbeitsgruppe „Biomolecular Photonics“. Neben der Hilfsbereitschaft und Anpack-Mentalität werden mir vor allem die bunt gemischten Charaktere und Events in Erinnerung bleiben.

Danke an die Physiker von D2: M.Sc. Oliver Reimer, M.Sc. Robin P. Klett und B.Sc. Jan P. Haskenhoff für die Freundschaft und Ablenkung vom Uni-Alltag. Ganz besonders an Torsten Hübner, mit dem ich eine geile Zeit in London hatte. Natürlich darf ich auch nicht die vergessen, die uns irgendwann verlassen haben: Hanno Meyer zu Theenhausen, Thomas Lilienkamp, Michael Stührenberg und Carolin Böger. Dankeschön.

Größten Dank an meine Familie. An meinen Bruder Stephan, der nie müde wird mich zu coolen Aktionen zu motivieren. Und natürlich an meine Eltern Annegret und Günther, die mich ausnahmslos auf meinem Weg durchs Leben unterstützen und immer für mich da sind.

Mein letzter Dank gilt Mandy Kleinsorge. Für das Aushalten und Unterstützen in der stressigen Endphase der Doktorzeit. Dafür, dass Du mein Leben so unfassbar toll machst. Danke.

In Erinnerung an

Annegret Simonis

Erklärung

Hiermit erkläre ich,

- dass ich die vorgelegte Dissertation selbständig und ohne unzulässige fremde Hilfe angefertigt und verfasst habe, dass alle Hilfsmittel und sonstigen Hilfen angegeben und dass alle Stellen, die ich wörtlich oder dem Sinne nach aus anderen Veröffentlichungen entnommen habe, kenntlich gemacht worden sind;

- dass die Dissertation in der vorgelegten oder einer ähnlichen Fassung noch nicht zu einem früheren Zeitpunkt an der Universität Bielefeld oder einer anderen in- oder ausländischen Hochschule als Dissertation eingereicht worden ist.

Matthias Simonis

Diese Arbeit wurde auf säurefreiem, alterungsbeständigem Papier gedruckt.
(gemäß DIN EN ISO 9706)